Drag of Spanwise Heterogeneous Surface Topographies

Zur Erlangung des akademischen Grades eines

Doktors der Ingenieurwissenschaften (Dr.-Ing.)

von der KIT-Fakultät für Maschinenbau des
Karlsruher Instituts für Technologie (KIT)
angenommene

Dissertation

von

M. Sc. Lars Hendrik von Deyn

Tag der mündlichen Prüfung:	29. November 2022
Hauptreferentin:	Prof. Dr.-Ing. Bettina Frohnapfel
Korreferent:	Prof. Dr. Nicholas Hutchins

Abstract

Accurately predicting the drag of turbulent wall-bounded flows above a given surface topography is subject of ongoing research. Especially spanwise heterogeneous surfaces pose a significant challenge in the prediction of drag. It is currently uncertain how to adequately embed heterogeneity effects in the existing framework to predict the roughness function ΔU^+ by means of the equivalent sand grain roughness k_s.

In this work, Nikuradse-type diagrams of spanwise heterogeneous topographies in channel flow are experimentally assessed via pressure-drop measurements in order to provide reliable friction measurements and to uncover occurring drag regimes of spanwise heterogeneous topographies. Two categories of spanwise heterogeneous topographies are investigated: first, 2D surface structures referred to as riblets and ridges are investigated spanning from the homogeneous regime (where $s \ll \delta$) to the onset of heterogeneous behaviour where $s \to \delta$. Second, surfaces comprised of spanwise alternating strips of smooth and sandpaper are investigated. Complementary hot-wire and sPIV measurements are carried out to enable local flow analysis and to better link with literature studies.

While analyzing the drag behaviour of trapezoidal grooved surfaces of different sizes, it is observed that an appropriate definition of the effective channel height δ is crucial for interpreting the drag behaviour. For 2D surface structures, this work shows that defining δ with the streamwise protrusion height $h_{\|}$ of the structured surface is favourable as this definition allows to discern the modification of C_f induced by turbulence. For spanwise heterogeneous roughness consisting of spanwise alternating smooth and sandpaper roughness strips this approach cannot directly be applied. An attempt to define a laminar reference height h_{lam} is made based on laminar flow solution obtained via DNS that assumes a different physical interpretation than $h_{\|}$.

This work shows that the roughness function ΔU^+ of 2D surface structures, commonly termed riblets or ridges depending on their physical size, increases logarithmically with l_g^+ for $l_g^+ > 17$. Thus, an apparent fully-rough behaviour up to $l_g^+ \approx 40$ is found.

Interestingly, the investigated 2D surface structures do not behave as "regular" homogeneous roughness, which stays within the fully-rough regime once the transitionally rough regime is surpassed. Instead, further increase of the Reynolds number, i.e. l_g^+ leads to a clear departure from the fully-rough regime and an unexpected non-monotonic behaviour of the roughness function ΔU^+ for $50 < l_g^+ < 200$ is found. As a quantity to match the newly observed drag behaviour at high Reynolds numbers, a hydraulic height, similar to the classical hydraulic diameter, is introduced and shown to provide a framework for the drag prediction of ridges in the respective drag regime.

Increasing the complexity of the investigated spanwise heterogeneous topographies, drag measurements of spanwise alternating smooth and sandpaper strips reveal a comparable "transitionally" fully-rough behaviour. When employing the concept of k_s to the presently investigated surfaces, fully-rough behaviour is found for $15 \lessapprox k_s^+ \lessapprox 40$. Comparable to the 2D surface structures, increasing k_s^+ leads to a clear departure from the fully-rough regime.

As expected, secondary motions are present for the investigated heterogeneous surfaces observed in the numerous hot-wire and sPIV measurements, which are known to alter the resulting global friction. However, so far no satisfactory explanation of the unexpectedly rich drag behaviour has been found and should therefore be addressed in future work.

Kurzfassung

Die genaue Vorhersage des Reibungswiderstandes von turbulenten wandgebundenen Strömungen über einer gegebenen Oberflächentopographie ist Gegenstand aktueller Forschung. Insbesondere spannweitig heterogene Oberflächen stellen eine große Herausforderung bei der Vorhersage des Reibungswiderstandes dar, und es ist derzeit ungewiss, wie man Heterogenitätseffekte angemessen in den bestehenden Rahmen zur Vorhersage der Rauhigkeitsfunktion ΔU^+ mit Hilfe der äquivalenten Sandkornrauigkeit k_s einbinden kann.
In der vorliegenden Arbeit werden Nikuradse-Diagramme von spannweitig heterogenen Topographien in einer Kanalströmung experimentell durch Druckmessungen untersucht, um zuverlässige Reibungsmessungen zu erhalten und die auftretenden Reibungs Regime von spannweitig heterogenen Topographien zu untersuchen. Ergänzend werden Hitzdraht- und sPIV-Messungen durchgeführt, um eine lokale Strömungsanalyse zu ermöglichen und eine bessere Verbindung zu Literaturstudien herzustellen.
Bei der Analyse des Widerstandsverhaltens von trapezförmig gerillten Oberflächen unterschiedlicher Größe zeigt sich, dass eine geeignete Definition der effektiven Kanalhöhe δ für die Interpretation des Widerstandsverhaltens entscheidend ist. Für 2D-Oberflächenstrukturen hat sich herausgestellt, dass die Definition von δ mit der longitudinalen Protrusion Höhe $h_{\parallel}$ der strukturierten Oberfläche vorteilhaft ist, da diese Definition es erlaubt, die durch Turbulenz induzierte änderung von C_f zu erkennen. In ähnlicher Vorgehensweise wird eine mittels DNS erhaltene laminare Strömungslösung verwendet, um eine laminare Bezugshöhe h_{lam} für eine über die Spannweite verteilte heterogene Rauheit zu definieren, die aus über die spannweite alternierenden abwechselnd glatten und Sandpapierstreifen besteht.
Unter Verwendung dieses laminaren Bezugssystems werden zum ersten Mal verschiedene Widerstandsregime beobachtet. Es wird gezeigt, dass die Rauheitsfunktion ΔU^+ von 2D-Oberflächenstrukturen, die je nach ihrer physikalischen Größe als Riblets oder Ridges bezeichnet werden, für $l_g^+ > 17$ logarithmisch mit l_g^+ zunimmt. So wird ein scheinbar vollständig raues Verhalten bis zu $l_g^+ \approx 40$ beobachtet. Riblets werden terminologisch von Ridges anhand ihrer relativen Größe der Quadratwurzel der Rillenfläche l_g in Bezug auf δ unterschieden, d.h. 2D-Strukturen mit $l_g/\delta < 0,17$ werden als Riblets bezeichnet.
Interessanterweise verhalten sich die untersuchten 2D-Oberflächenstrukturen nicht wie "reguläre" homogene Rauhigkeiten, die im vollständig rauen Bereich verbleiben, sobald der übergangsweise raue Bereich überschritten ist. Stattdessen führt eine weitere Erhöhung der Reynoldszahl, d.h. l_g^+, zu einem deutlichen Verlassen des vollrauen Regimes und es wird ein unerwartetes nicht-monotones Verhalten der Rauheitsfunktion ΔU^+ für $50 < l_g^+ < 200$ beobachtet. Als eine Größe, die dem neu beobachteten Widerstandsverhalten bei hohen Reynoldszahlen entspricht, wird eine hydraulische Höhe, ähnlich dem klassischen hydraulischen Durchmesser, eingeführt und gezeigt, dass sie einen Rahmen für die Widerstandsvorhersage von Ridges im entsprechenden Widerstandsregime bietet.
Um die Komplexität der untersuchten heterogenen Topographien in spannweiten Richtung zu erhöhen, zeigen Widerstandsmessungen von abwechselnd glatten und Sandpapierstreifen in Spannweitenrichtung ein vergleichbares "vorübergehendes" voll-raues Verhalten. Wendet man das Konzept von k_s auf die hier untersuchten Oberflächen an, so findet man vollrauhes Verhalten für $15 \lessapprox k_s^+ \lessapprox 40$. Wie bei den 2D-Oberflächenstrukturen führt eine Erhöhung von k_s^+ zu einer deutlichen Abweichung vom vollständig rauen Regime.

Wie erwartet sind bei den untersuchten heterogenen Oberflächen Sekundärströmungen vorhanden, die in den zahlreichen Hitzdraht- und sPIV-Messungen beobachtet wurden und bekanntlich die resultierende globale Reibung beinflussen. Bisher wurde jedoch noch keine zufriedenstellende Erklärung für das unerwartet reichhaltige Widerstandsverhalten gefunden und sollte daher in zukünftigen Arbeiten näher untersucht werden.

Contents

1 Introduction

The prediction of the global friction drag of a wall-bounded flow in the vicinity of arbitrary surface topography is an ongoing endeavour in current research [25]. Generally speaking, the friction drag of a given surface structure is only accurately known after testing it numerically or experimentally [16].

1.1 Motivation

The knowledge of the drag associated with a given surface topography is crucial in a variety of applications ranging, e.g. from turbulent boundary layers on aircraft and ship hulls to atmospheric boundary layers. A surface cannot be considered smooth if its topographical features are large enough to alter the transfer of momentum (drag), heat, and mass. In practice, because each roughness topography affects flow differently, the uncertainty of predictions is at least 10% [16]. This has enormous ramifications with uncertainties costing billions of euros per year, as illustrated by the following examples: In shipping, bio-fouling significantly increases the skin-friction drag of ship hulls with associated costs in the hundred millions of dollars [107]. Economically informed maintenance decisions depend on accurate drag estimates and can reduce the drag-penalty cost. In aviation, roughness effects can be performance critical, as measurements of surface roughness on turbine blades showed [10]. Also, in the context of renewable energy during the design process of wind farms, environmental and surface roughness play a role in determining turbine selection and economic viability [121]. Therefore, the predictability and the understanding of related physical mechanisms offers opportunity for long-term performance optimisation and potential mechanisms for reducing skin-friction drag.

Currently, a significant shortcoming of available predictive correlations is their focus on homogeneous roughness due to its easier predictability. However, most realistic occurring roughness topographies are patchy or heterogeneous. In order to dissect heterogeneity effects in subgroups, researchers commonly distinguish between streamwise and spanwise variations in roughness topographies and analyse respective configurations separately [16]. Streamwise alternating smooth and rough elements or patches were e.g. studied by [94, 57, 62]. These studies mention the emergence of an internal boundary layer when a sudden change in streamwise direction between a smooth wall and roughness or vice versa occurs and the need for a substantial development length to return to equilibrium conditions. Considering spanwise heterogeneous surfaces, such configurations occur in a variety of applications, e.g. natural flows such as river bed flows [20] and the atmospheric boundary layer [8], but also in engineering flows over ablated turbine blades [4]. Therefore, designated studies are much needed to better understand the resulting skin-friction drag.

It is known that the lateral surface inhomogeneities induce spanwise gradients in turbulent stresses that lead to the formation of Prandtl's secondary flows of the second kind [3, 48]. Secondary motions significantly alter momentum and heat transfer properties [104] and are therefore essential to be considered in predictive frameworks. One objective of the present study is to provide reliable drag measurements of surface topographies that induce said secondary flows and to study possible Reynolds number effects of the global skin-friction drag. Linking with reported flow phenomena described in the literature, this procedure is intended to contribute a further step towards the predictability of heterogeneous topographies.

1.2 Background

Established engineering predictions of roughness effects such as the Moody diagram reprinted in figure 1.1 [78] enable an approximation of the skin-friction coefficient C_f as a function of the bulk Reynolds number Re_b. Once a fully-rough flow state is reached, C_f (which is proportional to the friction factor $\lambda = 4C_f$ plotted in figure 1.1) becomes independent of Re_b. This was first demonstrated in the famous experiments by Nikuradse [80], who measured the friction factor of sand grain roughened pipe flow.

In the fully-rough regime, a hydraulic roughness length scale can be defined, linking the roughness topography to the friction factor. Commonly, this length scale is termed the *equivalent sand grain roughness* k_s referring to Nikuradse's experiments [80]. The table inserted in figure 1.1 states the equivalent sand grain roughness k_s for exemplary surface topographies. The respective friction factor is plotted as a function of the relative pipe roughness k_s/D defined with the pipe diameter D. This makes the Moody diagram an easily accessible tool for back-of-the-envelope estimations of roughness effects on the global drag.

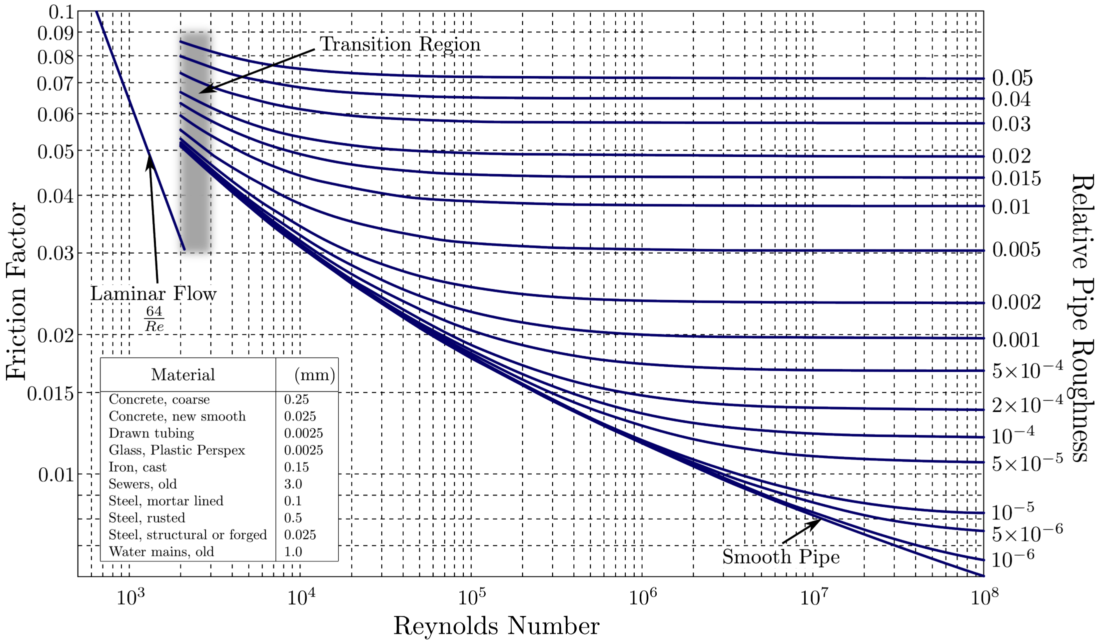

Material	(mm)
Concrete, coarse	0.25
Concrete, new smooth	0.025
Drawn tubing	0.0025
Glass, Plastic Perspex	0.0025
Iron, cast	0.15
Sewers, old	3.0
Steel, mortar lined	0.1
Steel, rusted	0.5
Steel, structural or forged	0.025
Water mains, old	1.0

Figure 1.1: Friction factors for pipe flow, reprinted from Moody [78].

However, the definition of k_s is not straightforward. Generally speaking, k_s is an unknown function of relevant surface parameters and additionally depends on the individual flow conditions. Thus, an a priori definition of k_s is challenging and the key obstacle for a reliable friction prediction of rough surfaces in the fully-rough regime. Consequently, obtaining well-defined correlations to predict k_s is subject of ongoing research. In fact, a rough topology features a multitude of statistical properties, which are all relevant in terms of the resulting drag penalty [16]. As a starting point, researchers often choose simplified topographies, gradually increasing complexity.

Many studies, e.g. [14, 61, 67, 88] feature ordered distinct elements of various shapes that have the clear advantage of a well-defined shape enabling comprehensive parametric studies. As an additional degree of freedom, Forooghi et al. [32] studied randomly distributed distinct elements arguing that the random character is an important aspect of "real" roughness topography that needs to be accounted for. Experimentally, easy-to-manufacture surfaces such as grid blasted [29] or sandpaper configurations [103] are frequently studied. Also, a large number of application-based roughness studies exist. Here, studies featuring roughness configurations extracted from bio-fouling [77], turbine blades [119] and river beds [95] are noteworthy examples.

Overall, a multitude of roughness studies is available in the literature (see e.g. [16, 58, 59] for an overview) but with limited generalizability due to the nearly unlimited different roughness topographies. Consequently, current empirical correlations of k_s as a function of statistical properties, e.g. proposed by [13, 27, 32] are only applicable in a narrow parameter range within the scope where they were designed. Current endeavours of creating an extensive roughness database [109] and using data-driven methods as applied by [60] are promising approaches to enable a more accurate prediction of k_s in the fully-rough regime in the near future.

However, the equivalent sand grain roughness k_s is only well-established in the fully-rough regime of homogeneous rough surfaces. Especially for inhomogeneous roughness, the question arises if a fully-rough regime is present despite the spatial inhomogeneity. If not, other scales than k_s may be needed to better characterise the onset and quantification of roughness effects. For instance, Medjnoun et al. [69] studied streamwise aligned bars as a model for ridge-type roughness. Such surface structures can serve as a model geometry for inhomogeneous roughness in the sense that exceedingly rough patches compared to the remaining surface distribution are condensed into smooth protruding ridges aligned in streamwise direction on a smooth wall. In this configuration, they report a decreasing C_f with increasing Re_b, indicating the absence of a fully-rough regime for this type of surface structure. Hence, accurate skin-friction measurements of heterogeneous topographies over a wide range of Reynolds numbers are needed to unveil the underlying drag regimes of lateral heterogeneous topographies.

1.3 Objectives and Procedure

The present work aims at contributing to the drag predictability of lateral inhomogenous topographies. The study is conceptualised to link with literature studies and gradually increase the complexity of the investigated surface topographies. Considering the studies available in the literature, many studies feature a detailed analysis of velocity statistics, but relatively little is known regarding the implications for the overall skin-friction drag and the associated Reynolds number dependence. Most likely, the rationale is the high cost to obtain $C_f(Re_b)$ curves as shown in figure 1.1 in numerical studies and the need for designated friction measurement facilities for experimental studies.

In order to bridge this knowledge gap, the global skin-friction of various lateral heterogeneous surface configurations is assessed via high-precision pressure-drop measurements in channel flow. Additional hot-wire anemometry (HWA) and stereoscopic particle image velocimetry (sPIV) measurements allow the quantification of local flow effects and link with literature studies. The experimental facility is comparable to the facility used by Flack et al. (e.g. [27, 29, 31]) for homogeneous roughness research. The utilised high-precision facility built by Güttler [43] was used for drag-reduction research [38] in the past, where its suitability and accuracy have been proven.

For the present study, the Reynolds number range is extended up to $Re_b = 8.5 \times 10^4$ in order to investigate a broader range in drag regimes. First, reference measurements in the smooth channel in the extended Reynolds number range $4.5 \times 10^4 < Re_b < 8.5 \times 10^4$ are carried out, characterising the flow quality. The results are presented in chapter 4.

As the first of two groups of surface structuring, purely two-dimensional (2D) trapezoidal groove surface structures invariant with the mean flow direction are investigated (see chapter 5). This simplified configuration has the clear advantage of a well-defined geometry, where height h and spacing s can be systematically varied. Thus, a large range in viscous scaled wavelengths can be reached (see chapter 2 for definitions). Physically small 2D surface structures termed riblets are known even to reduce skin-friction drag. The underlying drag-reducing mechanism is reasonably well understood [35] or can at least be matched with a theoretical framework [66]. Moreover, precise drag measurements of riblets obtained with an oil tunnel are available in literature [7] upon which the present study can build as reference data.

Increasing the complexity, spanwise alternating strips of smooth and sandpaper roughness are investigated as the second group of surface structures (see chapter 6). As opposed to the purely 2D surface structures, the sandpaper roughness includes more features of realistic roughness, i.e. it experiences form drag in addition to the viscous drag. In order to link with the literature, protruding and submerged (see chapter 6 for detailed description) configurations are investigated, which correspond to so-called ridge-type and strip-type roughness, respectively.

Overall, the present study is intended to provide novel, unprecedented data over a wide range of Reynolds numbers and enable a discussion of the drag regimes of lateral inhomogeneous topographies. More specifically, it is intended to clarify to what extent established concepts in roughness research, such as the equivalent sand grain roughness k_s, are applicable.

2 Drag in Internal Channel Flows

This chapter introduces the governing equations and discusses fundamental definitions that are important when analysing the drag of internal flows. Starting from smooth laminar flow (§2.1.1) the complexity is gradually increased towards the discussion of spanwise heterogeneous surface topographies subject to turbulent flow (§2.2.3). Important aspects for drag assessment, such as the concept of a roughness function and outer-layer similarity, are also discussed. The chapter concludes with a refined definition of the objectives of the present work compared to §1.3.

For the presently investigated incompressible flow of a Newtonian fluid, the governing equations are the continuity and Navier-Stokes equations

$$\frac{\partial u_i}{\partial x_i} = 0, \tag{2.1}$$

$$\frac{\partial u_i}{\partial t} + u_j \frac{\partial u_i}{\partial x_j} = -\frac{1}{\rho}\frac{\partial p}{\partial x_i} + \nu \frac{\partial^2 u_i}{\partial x_j \partial x_j}, \tag{2.2}$$

with the three velocity components $(u_1, u_2, u_3) = (u, v, w)$ along the streamwise, wall-normal and spanwise $(x_1, x_2, x_3) = (x, y, z)$-axes, respectively. t, p, ρ and ν denote time, pressure, fluid density and the kinematic viscosity, respectively.

2.1 Smooth Wall Channel Flow

For a fully developed plane laminar channel flow, the definition of skin-friction, Reynolds number and their relationship with the streamwise pressure gradient is straightforward. In this context, channel flow denotes a flow between two plates which are infinite in length and width. However, note that strictly speaking, the experimental studies presented in this thesis are carried out in a duct flow facility of aspect ratio $\mathrm{AR} = W_{\mathrm{duct}}/(2\delta) \approx 12$ for practical reasons discussed in §3.1. W_{duct} denotes the width of the duct, while δ is the half channel height as shown in figure 2.1. Due to the high aspect ratio, the flow in the duct is approximated as two-dimensional plane channel flow neglecting side wall effects in the following. The validity of this approximation is assessed experimentally and verified in the spanwise core region of the duct as discussed in §4.2 and §4.3. Consequently, in chapters 5 and 6 the term *channel flow* is used when local flow measurements are discussed as no side-wall effects influence the measurement results. Thus, a comparison to channel flow of infinite width (commonly approximated with periodic boundary conditions in numerical studies) is valid.

2.1.1 Laminar Flow

For fully developed smooth laminar channel flow, the Navier-Stokes equations (2.2) simplify to

$$0 = -\frac{1}{\rho}\frac{\partial p}{\partial x} + \nu \frac{\partial^2 u}{\partial y \partial y} \tag{2.3}$$

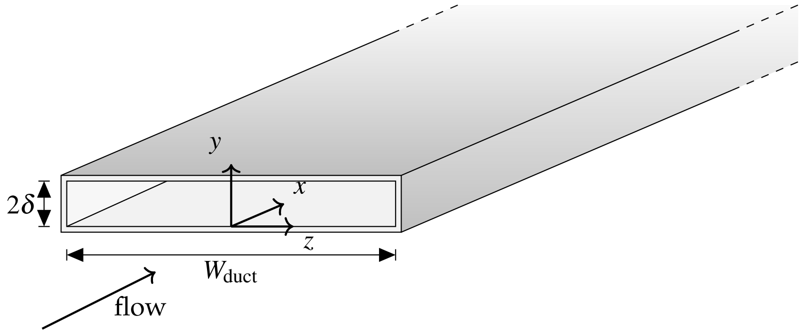

Figure 2.1: Sketch of the high aspect ratio duct used in the current experimental study including dimensions and the chosen Cartesian coordinate system.

and

$$0 = -\frac{1}{\rho}\frac{\partial p}{\partial y} \tag{2.4}$$

in streamwise and wall-normal directions, respectively. Thus, an analytical solution for the velocity profile U with the no-slip boundary conditions $U(0) = 0$ and $U(2\delta) = 0$

$$U = \frac{1}{\rho\nu}\frac{\partial p}{\partial x}\left(\frac{y^2}{2} - \delta y\right) \tag{2.5}$$

can be formulated (see figure 2.1 for the definition of the Cartesian coordinate system). Capital U indicates that the velocity profile has no time dependence.

With the wall shear stress τ_w defined as

$$\tau_w = \frac{1}{\rho\nu}\left.\frac{\partial U}{\partial y}\right|_{y=0}, \tag{2.6}$$

τ_w can be expressed as a function of the streamwise pressure gradient

$$\tau_w = -\frac{\partial p}{\partial x}\delta \tag{2.7}$$

derived from the simplified Navier-Stokes equation in streamwise direction (2.3). In dimensionless scaling, τ_w is referred to as the skin-friction coefficient C_f defined as

$$C_f = \frac{\tau_w}{\frac{1}{2}\rho U_b^2}, \tag{2.8}$$

where U_b is the bulk velocity defined as

$$U_b = \frac{1}{\delta}\int_0^{\delta} U \,\mathrm{d}y. \tag{2.9}$$

Due to the analytical solution for the velocity profile (2.5), the skin-friction coefficient C_f is directly related to the bulk Reynolds number

$$Re_b = \frac{2\delta U_b}{\nu} \tag{2.10}$$

through the expression

$$C_f = \frac{12}{Re_b}. \tag{2.11}$$

2.1.2 Turbulent Flow

For fully developed plane turbulent channel flow, "the flow may be considered to be the superposition of a basic or main flow with irregular stochastic fluctuations in the velocity or in other fluid mechanical quantities" [102]. Thus, the Reynolds decomposition can be applied to the individual velocity components such that

$$u_i(x_j,t) = \overline{u_i}(x_j) + u_i'(x_j,t). \tag{2.12}$$

$\overline{()}$ denotes time-averaged quantities in the following. For a more convenient notation, time-averaged velocity components are denoted $U_i(x_j) = \overline{u_i}(x_j)$ and the Reynolds stresses $u_i u_j = \overline{u_i' u_j'}$. Applying Reynolds averaging to the Navier-Stokes equations under fully developed plane turbulent channel flow conditions yields

$$0 = -\frac{1}{\rho}\frac{\partial \overline{p}}{\partial x} + \frac{\partial}{\partial y}\left(\nu \frac{\partial U}{\partial y} - uv\right). \tag{2.13}$$

In equation (2.13), $\nu \frac{\partial U}{\partial y} - uv$ can be interpreted as the total shear stress

$$\tau = \nu \frac{\partial U}{\partial y} - uv \tag{2.14}$$

consisting of the sum of the viscous and the Reynolds stress [89].

Consequently, the wall shear stress can still be expressed as a function of the streamwise pressure gradient as introduced in equation (2.7), except that quantities need to be considered in a time-averaged sense, i.e.

$$\tau_w = -\frac{\partial \overline{p}}{\partial x}\delta. \tag{2.15}$$

Dimensional analysis of equation (2.13) reveals that a convenient form to retrieve a dimensionless (hence universal) form of equation (2.13) is by introducing the friction velocity

$$u_\tau = \sqrt{\frac{\tau_w}{\rho}} \tag{2.16}$$

and a respective length scale

$$l_\tau = \frac{\nu}{u_\tau}. \tag{2.17}$$

Quantities in viscous scaling are denoted with a superscript $()^+$ throughout the thesis.

However, unlike for laminar plane channel flow, no universal solution for the velocity profile U can be derived from the streamwise Navier-Stokes equation (2.13). In search of a universal law for U, Pope

[89] argues that only two independent non-linear groups can be formed of $\rho, \nu, \delta, u_\tau, y$, e.g. Re_τ and y/δ, where

$$Re_\tau = \delta^+ = \frac{u_\tau \delta}{\nu} \tag{2.18}$$

is the friction Reynolds number. As an Ansatz for the streamwise velocity profile, $U^+ = F(\frac{y}{\delta}, Re_\tau)$ can be formulated and the logarithmic law of the wall

$$U^+ = \frac{1}{\kappa} \ln y^+ + B \tag{2.19}$$

with the a priori unknown von Kármán constant κ and the additive constant B follows. The logarithmic law of the wall is a good approximation of the streamwise velocity profile between $y^+ > 30$ and $y/\delta < 0.3$ for channel flow [89].

At high Reynolds numbers, the viscous and buffer layer regions of the velocity profile become small compared to the remainder of the wall-normal velocity profile. Moreover, only a small deviation from the logarithmic law of the wall (2.19) is found in the core region $y/\delta > 0.3$ of the channel [89]. Thus, the bulk velocity U_b can be approximated by assuming a logarithmic law over the whole channel and an expression for U_b can be obtained by integrating the velocity defect law:

$$\frac{U_{Cl} - U_b}{u_\tau} = \frac{1}{\delta} \int_0^\delta \frac{U_{Cl} - U}{u_\tau} \, \mathrm{d}y \tag{2.20}$$

$$\approx \frac{1}{\delta} \int_0^\delta -\frac{1}{\kappa} \log\left(\frac{y}{\delta}\right) \mathrm{d}y = \frac{1}{\kappa} \tag{2.21}$$

With this, a relation U_b/u_τ can be derived using equation (2.21):

$$\frac{U_b}{u_\tau} = \frac{1}{\kappa} \log\left[\frac{Re_b}{2}\left(\frac{u_\tau}{U_b}\right)\right] + B - \frac{1}{\kappa} \tag{2.22}$$

and therefore, C_f becomes predictable since

$$C_f = 2\frac{\tau_w}{\rho}\frac{1}{U_b^2} = 2\frac{u_\tau^2}{U_b^2} \tag{2.23}$$

Alternatively, Dean [23] experimentally studied the skin-friction of smooth high aspect ratio ducts and derived the widely used empirical correlation

$$C_f = 0.073 Re_b^{-\frac{1}{4}}. \tag{2.24}$$

The C_f vs. Re_b curves of the Dean correlation [23] and equation (2.22) are plotted in figure 2.2. Also the laminar solution (see §2.1.1, (2.11)) is included up to $Re_b = 3000$. Up to $Re_b < 1 \times 10^5$, equation (2.22) yields slightly lower C_f values with the constants set to $\kappa = 0.39$ and $B = 5.2$ compared to the empirical Dean correlation. Note that the experimental data used by Dean was compiled in a duct flow facilities. Hence, the slightly higher C_f can be attributed to side wall effects compared to theoretical considerations based on infinitely wide plates as equation (2.22). In figure 4.1, DNS results [51] are included for reference and agree well with equation (2.22) except for the highest Reynolds number $Re_b \approx 2 \times 10^5$ ($Re_\tau = 4200$). In the following, Dean's correlation stated as equation (2.24) is used as

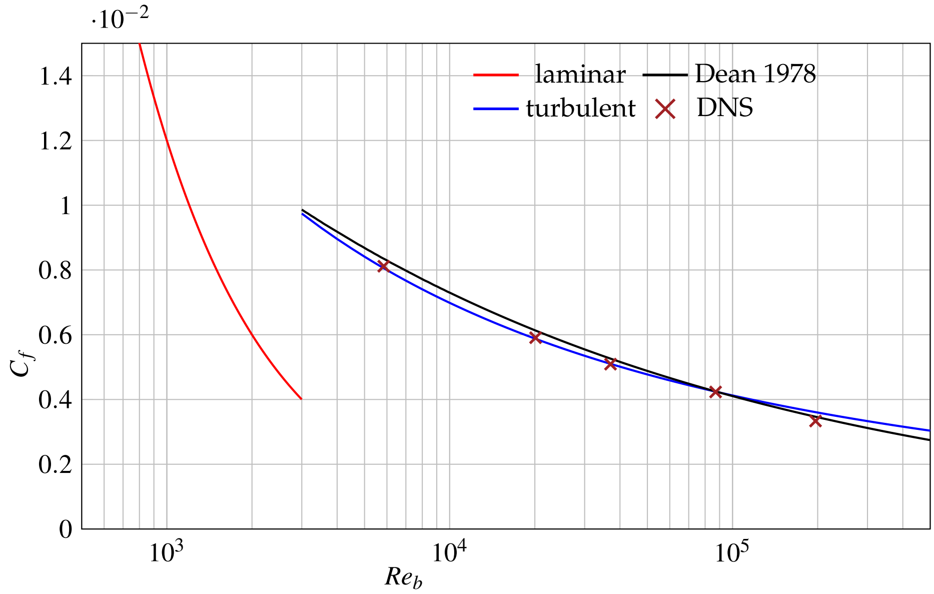

Figure 2.2: C_f vs. Re_b for the derived equations for laminar (2.11) and turbulent (2.22) flow. The correlation proposed by Dean [23] and DNS results of Hoyas and Jiménez [51] are included for reference.

a reference for smooth experimental results, given the similarity of Dean's facility to the one used in the present investigation.

2.2 Flow with Surface Topographies

Building on the theory derived for smooth wall internal flows, the implications of surface topographies on laminar and turbulent flow are discussed in the following, focusing on friction-related quantities. When the walls are not flat, the temporally- and spatially-averaged wall-shear stress τ_w defined in equation (2.15) "assumes the different meaning of an effective wall-shear stress, which balances the [streamwise] pressure gradient as if it was caused by a virtual flat wall placed at a distance δ from the channel centreline" [von Deyn et al., 2022a]. Hence, the definition of the wall-normal origin and the channel half height δ deserves special attention.

The effect of non-planar surfaces, i.e. surface topographies of some shape or form, commonly scales in viscous units and is felt by the flow when the characteristic length scale of the surface exceeds the viscous length scale [16]. In the following, important theoretical concepts to quantify, alter and ideally predict surface topography effects of the wall friction are discussed.

2.2.1 Laminar Flow

In case of laminar flow, Re_b and C_f are coupled through the analytical expression (2.11) discussed in §2.1.1 for a smooth wall flow. From a classical point of view, rough surfaces as investigated by Nikuradse [80] are expected to coincide with equation (2.11) in the laminar flow regime. However, studies on laminar flow commenced with a growing interest in micro-channel applications, where the flow is mostly laminar due to the small characteristic length scale, have reported significant roughness effects even in laminar flow conditions [64, 83]. Gamrat et al. [34] found an increase in friction independent of Re_b for their investigated roughness configurations that can be accounted for with an effective roughness height k_{eff}, i.e. a shift of the virtual wall perceived by the flow.

While studying the pressure losses related to 2D grooves in laminar channel flow, Mohammadi and Floryan [76] dissected the pressure losses into a change of the channel height matching the smooth reference and a flow modulation effect of the individual groove shape. This highlights the importance of the channel height for the global friction. This particular example even reveals drag-reducing potential when the surface topography is chosen accordingly [74]. Especially streamwise aligned trapezoidal grooves seem particularly well suited to reduce the drag of laminar flow [75]. However, the reported drag reduction found in laminar flow does not necessarily extend to turbulent flow due to the different underlying mechanisms, as e.g. shown by [22].

2.2.2 Turbulent Flow Subjected to Homogeneous Surface Topographies

When the walls are not flat, i.e. the viscous-scaled characteristic length scale k of a given surface does not fulfil $k^+ \ll 1$, significant roughness effects occur that alter the global drag penalty. Hence, the theory outlined in §2.1 that holds for smooth-wall flow needs to be adjusted to accommodate roughness effects. Due to the high relevance of the roughness problem (i.e. predicting τ_w of a given surface topography as a function of a priori known quantities), researchers took on the challenge of establishing a framework to account for roughness effects in turbulent flows. This is highly relevant for a wide range of applications from environmental flows such as the atmospheric boundary layer to engineering flows such as marine transportation or turbomachinery. Considering the vast parametric space necessary to characterise a specific surface topography, this is a daunting task and therefore an ongoing endeavour. Nevertheless, important concepts have been established, summarised in the following.

Generally speaking, surface topographies are known to induce a vertical and a horizontal shift in the logarithmic region of the viscous-scaled velocity profile [16]. As for the smooth wall case, a logarithmic law of the wall

$$U^+ = \frac{1}{\kappa} \ln y^+ + B - \Delta U^+ \tag{2.25}$$

can be formulated, where κ takes the same value as with smooth walls [59]. Note that y^+ is defined with respect to the virtual flat wall and the roughness function ΔU^+ accounts for the vertical shift induced by the surface topography [45]. As discussed in chapters 5 and 6, the placement of the virtual flat wall is of particular importance when assessing the drag of surface topographies. Different choices of the wall-normal origin are shown in §5.4.1 and §6.6.1 to asses its implications for friction related quantities. Commonly, the wall-normal origin is placed somewhere between the bed on which surface structures are mounted and the structure's crest, while the specific placement is determined by the flow [16]. Geometrical definitions such as the spatially averaged structure height k_{avg} are well defined a priori but may not result in the desired universality as discussed in §5.4.1.

Roughness Function

The roughness function ΔU^+ is a convenient way to quantify the drag penalty associated with a particular surface topography. Most rough surfaces increase turbulent drag, i.e. $\Delta U^+ > 0$, while negative values of ΔU^+ indicate drag reduction.

From an engineering point of view, the importance of the roughness function is that once ΔU^+ as a function of some roughness scale k is known for a given surface topography, it can be used in order to predict the drag at a given flow condition. Hence, researchers commenced studies on various roughness configurations and flow speeds, e.g. [26, 103] and found that ΔU^+ reaches a monotonic trend with k^+

$$\Delta U^+ = \frac{1}{\kappa} \ln k^+ + C \tag{2.26}$$

commonly referred to as the roughness function in the *fully-rough regime* [85]. Consequently, in the fully-rough regime, the roughness problem simplifies to finding a suitable roughness characterisation k. Following the famous experiments of Nikuradse [80], the concept of an equivalent sand grain size k_s is introduced [98]. Nikuradse measured the friction of uniform sand grains of size k_s, which he glued onto the wall of a pipe. The friction measurements reach well into the fully-rough regime and thus provide a well-defined reference case. In search of a suitable roughness scale, it is common practice to convert the physical roughness size k of an arbitrary surface to the hydraulic scale k_s, such that equation (2.26) can be rewritten as

$$\Delta U^+ = \frac{1}{\kappa} \ln k_s^+ + B - 8.5 \tag{2.27}$$

with the coefficients κ and B identical to the values of the smooth reference case. In doing so, full-scale drag predictions boil down to relating k_s to only topographical features of a given surface, which is subject of ongoing research [16]. Current empirical correlations of k_s as a function of statistical properties, e.g. as proposed by [13, 27, 32] are only applicable in a narrow parameter range within the scope where they are designed.

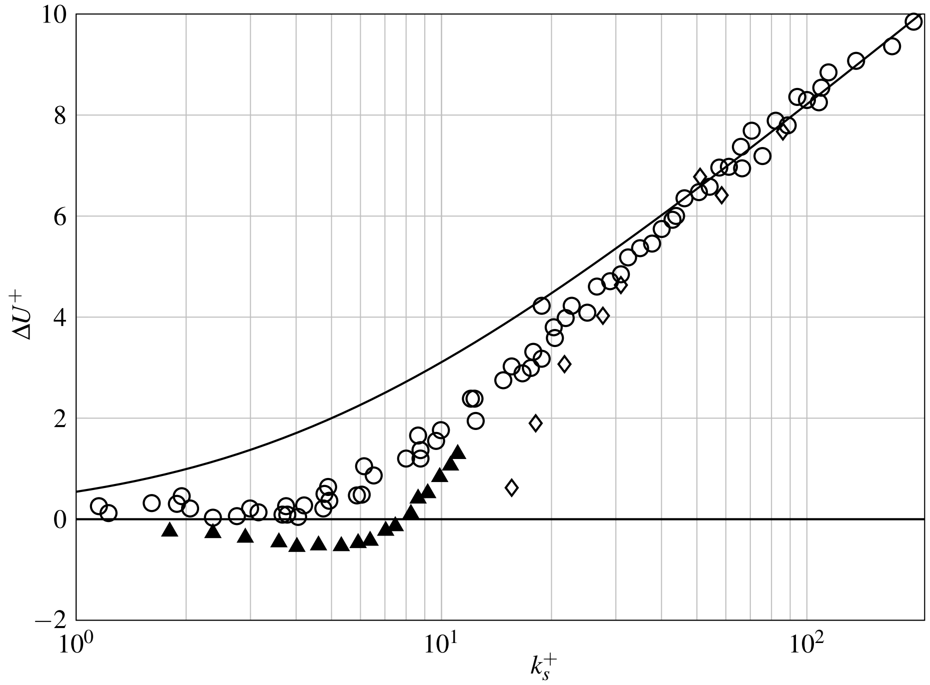

Figure 2.3: Roughness function ΔU^+ as a function of the viscous-scaled equivalent sand grain roughness k_s^+. Results are replicated from the review article of Jiménez [59]. The circles represent the uniform sand grain experiments of Nikuradse [80], while the solid line represents Colebrook's relation [19]. Open diamonds represent results on uniform packed spheres [63] and filled triangles on triangular riblets [7].

The roughness function ΔU^+ as a function of k_s is shown in figure 2.3 for literature data replicated from Jiménez review paper [59]. It can be nicely seen that ΔU^+ of Nikuradse's experiment shown as the open circles tends to the fully-rough regime after surpassing the so-called *transitionally rough regime* for small k_s. As further reference, results on uniform packed spheres [63] shown as open triangles in figure 2.3 show a different roughness behaviour in the transitionally rough regime but also tend to the fully-rough regime for $k_s \gtrsim 40$.

Drag balance measurements by Bechert et al. on triangular riblets shown as filled triangles in figure 2.3 reveal the expected drag reducing effect of riblets ($\Delta U^+ < 0$) for $k_s \lesssim 10$. Interestingly, towards higher k_s, Jiménez states that "their behaviour when $k \gg 1$ is that of regular k-surfaces" [59], i.e. tends to a fully-rough behaviour. The drag associated with triangular streamwise aligned surface structures is further assessed in the present study, as discussed in §5.4.2.

Roughness Function Computed from Bulk Flow Quantities

Commonly, the roughness function ΔU^+ is obtained from evaluating the viscous-scaled mean streamwise velocity profile experimentally (e.g. [26]) or numerically (e.g. [32]). However, in the present investigation, the global drag is assessed by means of global pressure-drop measurements, i.e the bulk flow rate $\dot{V}$ and the streamwise pressure gradient $\Pi = -\frac{\Delta \overline{p}}{\Delta x}$ are measured (see §3.1).

Assuming that the logarithmic law of the wall holds for the smooth wall and structured case with the same κ and wake function $G(y/\delta)$, equation (2.25) can be evaluated at the channel centreline for the structured and smooth case. Subtracting the smooth from the structured centreline velocity U_{Cl}^+ as illustrated in figure 2.4 yields the expression

$$\Delta U^+ = \frac{1}{\kappa} \ln \frac{Re_\tau}{Re_{\tau 0}} - \Delta U_{Cl}^+. \tag{2.28}$$

The subscript $()_0$ refers to quantities of the smooth reference case at matched Re_b. With

$$U_b^+ = \sqrt{\frac{2}{C_f}} \tag{2.29}$$

and

$$C_f = \frac{8 Re_\tau^2}{Re_b^2} \iff Re_\tau = \sqrt{\frac{C_f Re_b^2}{8}} \tag{2.30}$$

the ratio $\frac{Re_\tau}{Re_{\tau 0}}$ can be expressed as a ratio of the skin-friction coefficients

$$\frac{Re_\tau}{Re_{\tau 0}} = \sqrt{\frac{C_f}{C_{f0}}}. \tag{2.31}$$

In order to obtain ΔU^+ as a function of global quantities only, a relation between U_b and the centreline velocity U_{Cl} is needed. This can be obtained by approximating the streamwise velocity profile with the logarithmic law of the wall and integrating said profile

$$\frac{U_{Cl} - U_b}{u_\tau} = \frac{1}{\kappa}, \tag{2.32}$$

as discussed in §2.1.2. Thus, ΔU^+_{Cl} can be approximated as $\Delta U^+_{Cl} \approx \Delta U_b$. Utilising this approximation, the roughness function can be expressed as a function of the skin-friction coefficients C_f of the structured case and C_{f0} of the smooth reference case

$$\Delta U^+ = \frac{1}{\kappa} \ln \sqrt{\frac{C_f}{C_{f0}}} + \sqrt{\frac{2}{C_{f0}}} - \sqrt{\frac{2}{C_f}}. \tag{2.33}$$

This methodology is also employed in other studies dealing with pressure-drop measurements of flows over irregular roughness [5, 28].

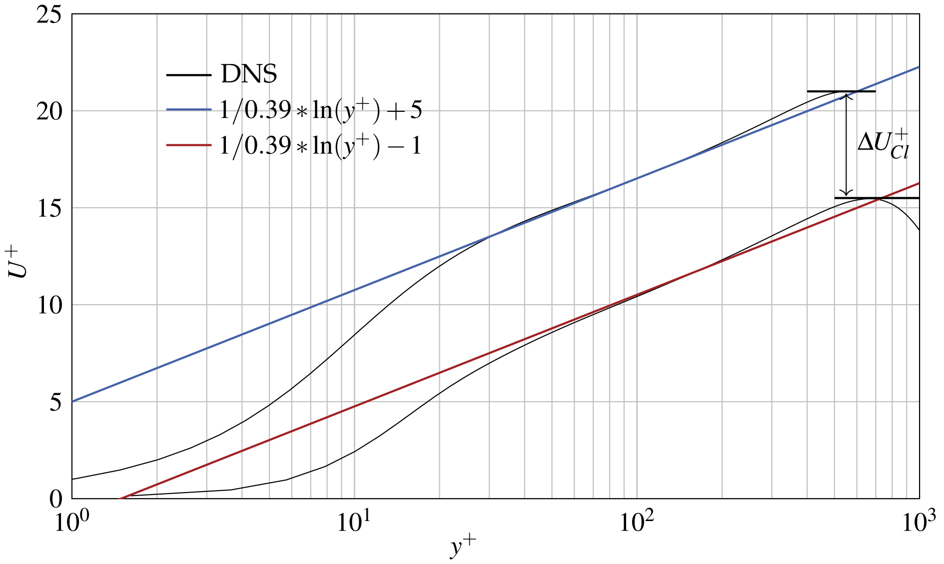

Figure 2.4: Plot to illustrate equation (2.28) to derive ΔU^+ from the centreline velocity shift U^+_{Cl} and Re_τ. The DNS results are the smooth and homogeneous rough case discussed later in §6.3. Note that smooth and rough cases are compared at constant flow rate in the present investigation, i.e. $Re_{\tau 0} \neq Re_\tau$.

Outer-Layer Similarity

The above-outlined framework to assess the roughness function ΔU^+ either by evaluating the vertical shift of the mean streamwise velocity directly or by the procedure outlined in §2.2.2 requires the flow to fulfil outer-layer similarity [16], i.e. that smooth- and rough-wall turbulence behave similarly, provided that they are sufficiently far away from the wall [106]. Specifically, this implies that the von Kármán constant κ remains unchained for rough-wall turbulence such that a logarithmic law of the wall with slope $1/\kappa$ can be formulated both for the smooth and rough case.

When the flow is subjected to some surface topography, the flow is most strongly affected in the vicinity of the wall. In the context of surface roughness, this region is often termed the roughness sublayer with an upper bound y_r [59]. Generally speaking, there is consensus that outer-layer similarly holds for sufficiently large scale separation $\delta \gg k$ such that a logarithmic region with $y > y_r$ and $y \ll \delta$ exists. For spanwise inhomogeneous surfaces, it is well established that the roughness sublayer extends to half the spanwise heterogeneity wavelength [11].

Despite numerous studies on outer-layer similarity [17, 30, 100, 117], it is subject of debate what quantitative criterion to prescribe as a requirement for outer-layer similarity, e.g. different suggestions regarding the wall-normal extent of the roughness sublayer exist [92, 30]. Moreover, it is also subject of ongoing research if outer-layer similarity holds for heterogeneous surface topographies [68].

2.2.3 Turbulent Flow Subjected to Spanwise Heterogeneous Surface Topographies

The procedure outlined in §2.2.2, which simplifies the roughness problem to predicting the equivalent sand grain roughness k_s for a given surface topography, is derived for homogeneous surface topographies. Nevertheless, heterogeneous roughness and particularly spanwise heterogeneous inhomogeneities are a crucial feature of many environmental and engineering surfaces [10, 21, 71].

Additional to the local roughness statistics, spanwise heterogeneous surfaces commonly exhibit a spanwise wavelength s. If s is in a similar order as δ, pronounced secondary motions occur [3, 110], which also determine the spatial extent of the roughness sublayer . "These vortical secondary motions are found in the temporally averaged flow field in the cross-plane perpendicular to the mean flow direction and only amount to a few per cent of the main flow's kinetic energy. Despite this relatively weak intensity, they can strongly alter the mean flow field, and, in consequence, the drag and heat transfer properties of a turbulent boundary layer [104]." [von Deyn et al., 2022b].

The phenomenon of domain-filling secondary flows is long known and dates back to the early works of Nikuradse [79] on non-circular pipe flow. Prandtl classified these secondary flows originating from turbulence anisotropy as secondary motions of the second kind and distinguished them from secondary motions of the first kind induced by mean flow skewness [90].

Secondary motions of Prandtl's second kind are often studied in square duct flow, where they are found to be very robust with Reynolds number [86] and contribute approximately six per cent of the total friction [73].

Investigations on roughness-induced secondary flows "date back to the work of [48] 1967 and are also mostly based on canonical wall-bounded shear flow configurations (turbulent duct, channel and boundary layer flow). For these equilibrium boundary layer flow conditions, there is a wide range of recent investigations, including e.g. the temporal dynamics of the secondary motions [116] or the link between secondary flows and very large scale motions [120]." [von Deyn et al., 2022b].

In the pioneering works by Hinze [48, 49], an upwelling motion above the smooth wall and a downwelling motion over the rough parts were observed. This sense of rotation of the secondary motions, i.e. where the upwelling and downwelling motion occurs with respect to the heterogeneous roughness, was subject of debate in recent years [96]. Recently, DNS by Stroh et al. [105] demonstrated that the rotational direction of secondary motions depends on the relative surface elevation, i.e. whether the roughness is protruding with respect to the "less rough" surrounding or recessed. Such configurations are further discussed in chapter 6.

Overall, the origins and topological details of secondary motions are subject of ongoing research, but there is consensus that the strength and relative size of secondary motions strongly depends on the ratio s/δ. This was shown by numerous studies systematically investigating spanwise heterogeneous roughness configurations of varying wavelength s [110, 120].

2.2.4 Open Research Questions and Refined Objectives

Many open questions in the field of roughness research remain to be adequately solved; first of all, an accurate prediction of k_s based only on statistical properties is needed. With particular focus on spanwise heterogeneous surface topographies, it remains to be uncovered whether the concept of matching the roughness function ΔU^+ as a function of k_s is applicable. This is particularly relevant since naturally occurring roughness is commonly patchy and inhomogeneous. It has been shown in the literature that secondary motions occur for spanwise heterogeneities with a length scale $s \approx \delta$ [110] and significantly impact the resulting friction [69, 104]. The physical mechanisms leading to the formation of secondary motions remain to be adequately addressed such that secondary motions can be incorporated into roughness predictions.

In the current work, two essential aspects related to the global drag of spanwise heterogeneous topographies are investigated, for which the present experimental approach (facilities described in the following chapter 3) is particularly well suited.

First, as mentioned in §2.2, the placement of the virtual flat wall, i.e. the definition of the half-channel height δ, is directly related to the resulting skin-friction through equation (2.15) and as such influences the reported values of C_f and ΔU^+. Hence, different possibilities to define δ are discussed in §5.4.1 and §6.6.1 and evaluated in terms of their suitability.

Second, it is investigated whether or to what extent the framework to define k_s established for homogeneous roughness also holds for spanwise heterogeneous roughness. By experimentally investigating the global drag expressed as ΔU^+ over a wide range of Reynolds numbers, it is assessed whether and how good the obtained friction measurements overlap with established concepts in the literature such as the fully-rough regime.

In order to reach these objectives, investigating the skin-friction drag of 2D streamwise-aligned surface structures is particularly well suited since 2D structures are well-defined and documented in the literature. Specifically, eight sets of 2D streamwise aligned trapezoidal grooves are investigated and the outcomes are discussed in chapter 5. On the lower bound of physical size, the drag behaviour of these structures resembles that of riblets which are known to reduce drag [7]. On the upper bound of physical size, the structures drag behaviour coincides with the drag characteristics of streamwise aligned bars termed ridges, which are investigated in literature as simplified models of spanwise heterogeneous roughness [69][von Deyn et al., 2022b].

Admittedly, 2D streamwise-aligned surface structures cannot resemble the random character of naturally occurring roughness topographies. Hence, a second experimental campaign is carried out, increasing the complexity towards spanwise alternating smooth and rough strips and thus investigating a three-dimensional surface configuration of random character. As roughness configurations, protruding and submerged sandpaper strips alternating with smooth strips are studied in chapter 6 with respect to the smooth and homogeneous rough reference cases.

Due to the different surface configurations chosen, deliberately designed to overlap with similar arrangements in the literature, the present study is expected to reveal different drag regimes and provide novel, unprecedented friction measurements.

The aforementioned investigations are completed by hot-wire and stereoscopic particle image velocimetry (sPIV) measurements. The results are presented for selected cases, occasionally accompanied by DNS results[1]. The provided velocity statistics are intended to enable insight into the underlying flow conditions and further link with velocity measurements in the literature.

---

[1] the DNS are conducted by A. Stroh or J. Yang. At the respective locations in the text, their contribution is acknowledged.

3 Experimental Setup

The present chapter describes the utilised experimental facilities and measurement techniques. Two different facilities with identically built test sections are employed that are optimised for different purposes. In doing so, different measurement techniques can be applied on the same sets of surface topographies, as the wind tunnel planes can be swapped between facilities.

The main facility for the present investigation is a high-precision blower wind tunnel built prior to this work [43]. Its composition, validation and accuracy are discussed in detail in [43]. For the present work, the range in Re_b is extended to 8.5×10^5 from approx. 2.5×10^5 in the initial work. Hence, the description of the facility in §3.1 is kept rather short and emphasis is given on changes with respect to [43]. The utilized measurement techniques in the high-precision blower tunnel, namely pressure-drop measurements and single hot wire anemometry are described in sections §3.1.1 and 3.1.2, respectively.

In order to gain insight into the cross-plane velocity information, which is particularly relevant for the investigated spanwise heterogeneous surface topographies, stereoscopic particle image velocimetry (sPIV) measurements are carried out. It has been decided to avoid any structural changes to the high-precision blower tunnel facility, which would be needed to introduce the required tracer particles in order to ensure the unaltered measurement quality with respect to [38, 43]. Instead, a designated wind tunnel for particle-based measurement techniques is used for which an identically built test section has been constructed. The experimental set-up and eventually the experiments were conducted jointly with Hehner [47], who studied plasma actuators in turbulent flow utilising the same experimental set-up. The facility and sPIV setup are described in §3.2, while more details including an uncertainty estimation can be found in [47].

Finally, a brief discussion of the manufacturing process of the wind tunnel plates is given in §3.3. Note that details regarding the experimentally investigated surface topographies are given in the respective chapters, sections §5.2 and §6.2.

3.1 High-Precision Blower Tunnel Facility

The high-precision facility consists of a blower-type wind tunnel [70] that generates a channel flow in the test section. "The schematic set-up of the facility is shown in figure 3.1. The flow is driven by a radial fan with a large operational range of $40 - 6000\,\frac{\mathrm{m}^3}{\mathrm{hr}}$ and progresses through a supply pipe into a large settling chamber. The air is blown towards the back wall of the settling chamber which is opposite to the nozzle directing into the actual test section, in order to ensure a homogeneous flow distribution. The air flows through five grids embedded in wooden frames and a honeycomb flow straightener on its way through the settling chamber towards the test section. The arrangement of the radial fan outside the settling chamber minimises the blockage and decouples the vibrations generated by the radial fan. A nozzle of contraction ratio 6:1 connects the settling chamber with the rectangular duct test section. [...] Changes in ambient conditions are accounted for by tracking the inlet and outlet temperature via PT100 thermocouples with a maximum error below 0.1 K and the ambient pressure p_{amb} and humidity a_q using Adafruit BMP 388 and BME 280 sensors, respectively. The BMP sensor has an absolute accuracy of 0.5 hPa, while the BME sensor resolves a_q with an error of $\pm 3\%$." [von Deyn et al., 2022a]

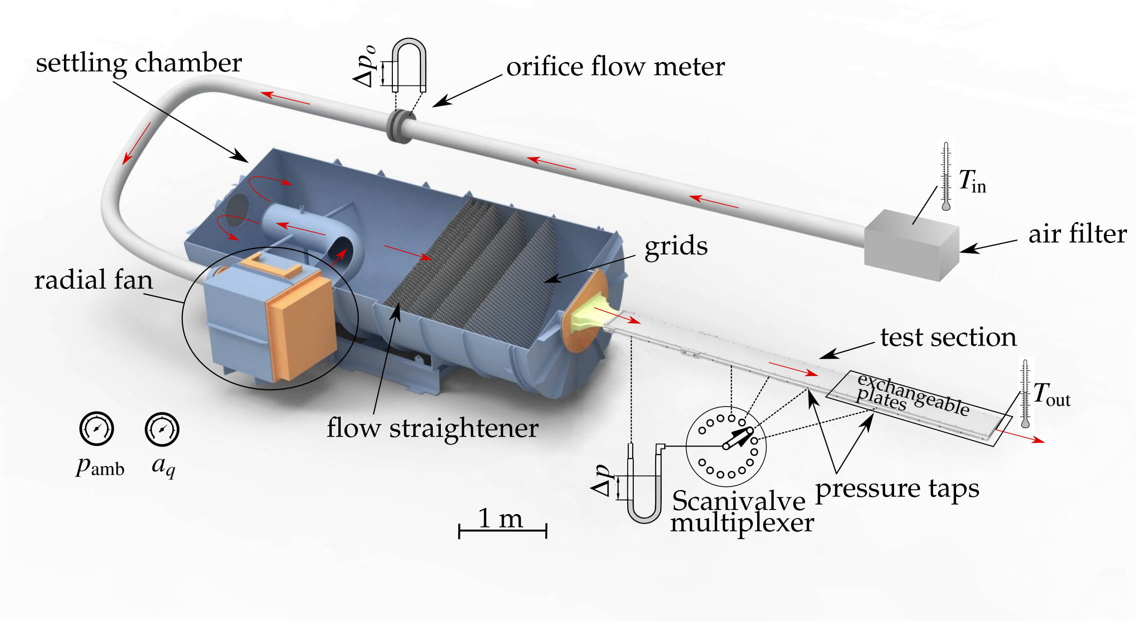

Figure 3.1: Schematic of the high-precision facility with respect to wind tunnel components and measurement instrumentation. Figure adopted from [von Deyn et al., 2022a].

Orifice Flow Meter

"On the suction side of the radial fan, an inlet pipe of diameter D is installed. A zig-zag tripping is located at the pipe entrance $32D$ upstream of an orifice flow meter of diameter d" [von Deyn et al., 2022a]. A technical drawing of the orifice flow meter built in agreement with the norm IS0 5167-2 [56] is shown in figure 3.2. The "diameter ratio $\beta = \frac{d}{D}$, across which the pressure drop Δp_o is measured, [is] related to the orifice flow rate [via]

$$\dot{V}_o = \frac{C}{\sqrt{1-\beta^4}} \varepsilon \frac{\pi}{4} d^2 \sqrt{\frac{2\Delta p_o}{\rho_{\mathrm{in}}}} . \tag{3.1}$$

The coefficients C and ε are derived from empirical expressions [56], where C depends on the diameter ratio β and the pipe Reynolds number Re_D [93]. As a result, the orifice flow rate $\dot{V}_o$ is computed with the iterative procedure outlined in norm EN [55], since Re_D itself is dependent on $\dot{V}_o$. The mass flow rate $\dot{m}$ through the pipe (and thus also the channel test section) is obtained based on the multiplication of the volume flow rate with the air density ρ_{in} deduced from the ideal gas law including humidity effects and a temperature measurement T_{in} at the pipe inlet.

In order to keep the dissipative losses generated by the orifice flow meter within reasonable limits and to avoid compressibility effects, a maximum differential pressure of $\Delta p_{o\mathrm{max}} = 625\,\mathrm{Pa}$ across the orifice is considered, thereby limiting the maximum achievable flow rate for a given d. For the sake of covering a range of the bulk Reynolds number of $4.5 \times 10^3 < Re_b < 8.5 \times 10^4$ (this corresponds to $150 \lesssim Re_\tau \lesssim 2000$ for the smooth wall case) in the test section, two different orifice flow meters are installed with inlet-pipe diameters of $D = 100\,\mathrm{mm}$ and $D = 200\,\mathrm{mm}$, respectively. Each custom-manufactured annular orifice measuring chamber can be equipped with orifice plates of varying inner diameters d. The configurations are specified in table 3.1. The orifice's pressure drop is measured with one of two Setra 239D (125 Pa and

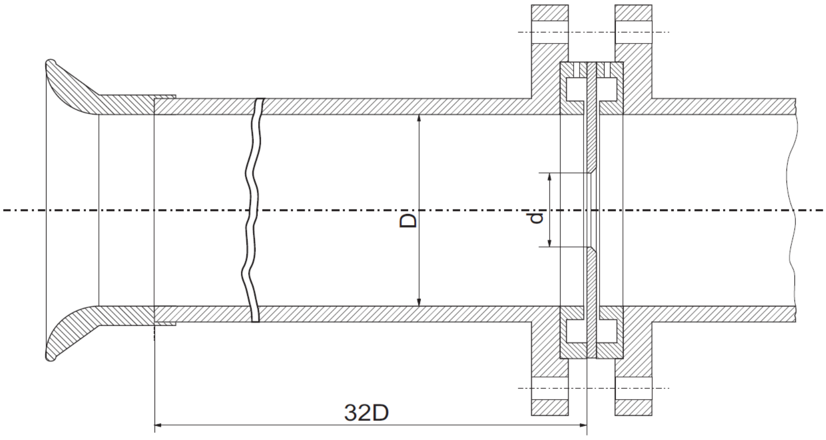

Figure 3.2: Technical drawing of utilised orifice flow meter with flange pressure tappings built according to the standard ISO-5167-2 [56].

marker	pipe diameter D	inner diameter d	approximate range in Re_b
△	100 mm	60 mm	$4.5 \times 10^3 < Re_b < 1.3 \times 10^4$
○	200 mm	105 mm	$6 \times 10^3 < Re_b < 2.3 \times 10^4$
◇	200 mm	120 mm	$7 \times 10^3 < Re_b < 3.8 \times 10^4$
□	200 mm	150 mm	$3 \times 10^4 < Re_b < 8.5 \times 10^4$

Table 3.1: Specifications of the different orifice flow meter configurations. Introduced markers are used in figures of chapters 5 and 6.

625 Pa full-scale) unidirectional differential pressure transducers with an accuracy of 0.07% of the full-scale, switching automatically depending on Δp_o." [von Deyn et al., 2022a]

Test Section

The test section, which is displayed in figure 3.3, "consists of a flat rectangular duct of aspect ratio AR $\approx$ 12, width $W_{\text{duct}} = 300$ mm and $\delta = 12.6$ mm in the smooth reference case. It extends in the streamwise direction $L = 3950$ mm, corresponding to $L = 313.5\,\delta$. Two plates for the top and bottom walls, as well as two monolithic rods for the side walls, form the test section. The duct walls are made of polished aluminium of average roughness $Ra = 0.4$ µm, and the top and bottom wall consist of three segments (950 mm, 1500 mm, 1500 mm) that can individually be exchanged."[von Deyn et al., 2022a]

As indicated in figure 3.3, in the most downstream section of the test section, the wind tunnel plates containing the investigated surface topographies are mounted. Note that in figure 3.3, the structured top plate is removed and the smooth top plate in the middle sector is cut for illustrative purposes. In the experimental investigations, structured wind tunnel plates are symmetrically installed on both the top and bottom walls.

"Two trip strips are installed at the inlet of the test section along the whole channel width. Each strip protrudes 1.6 mm ($0.13\,\delta$) from the wall and extends for 0.3 mm in the streamwise direction, resulting in 13% cross-section blockage. The trip provides fully-developed turbulent flow conditions for $Re_b > 4500$ starting $160\,\delta$ downstream of the tripping location [43].

21 pairs of pressure taps (diameter 0.3 mm) spaced at intervals of 200 mm are located along the side walls of the test section in order to measure the streamwise pressure gradient."[von Deyn et al., 2022a].

The yellow shaded areas in figure 3.3 highlight the positioning of the pressure taps utilised in the experimental investigation. At the exit of the wind tunnel test section, a traversing system is mounted (schematically included in figure 3.3 as the light blue box), which can be used for semi-automated hot-wire measurements. The measurement instrumentation, including the hot wire anemometer and the pressure transducer, is placed directly below the test section.

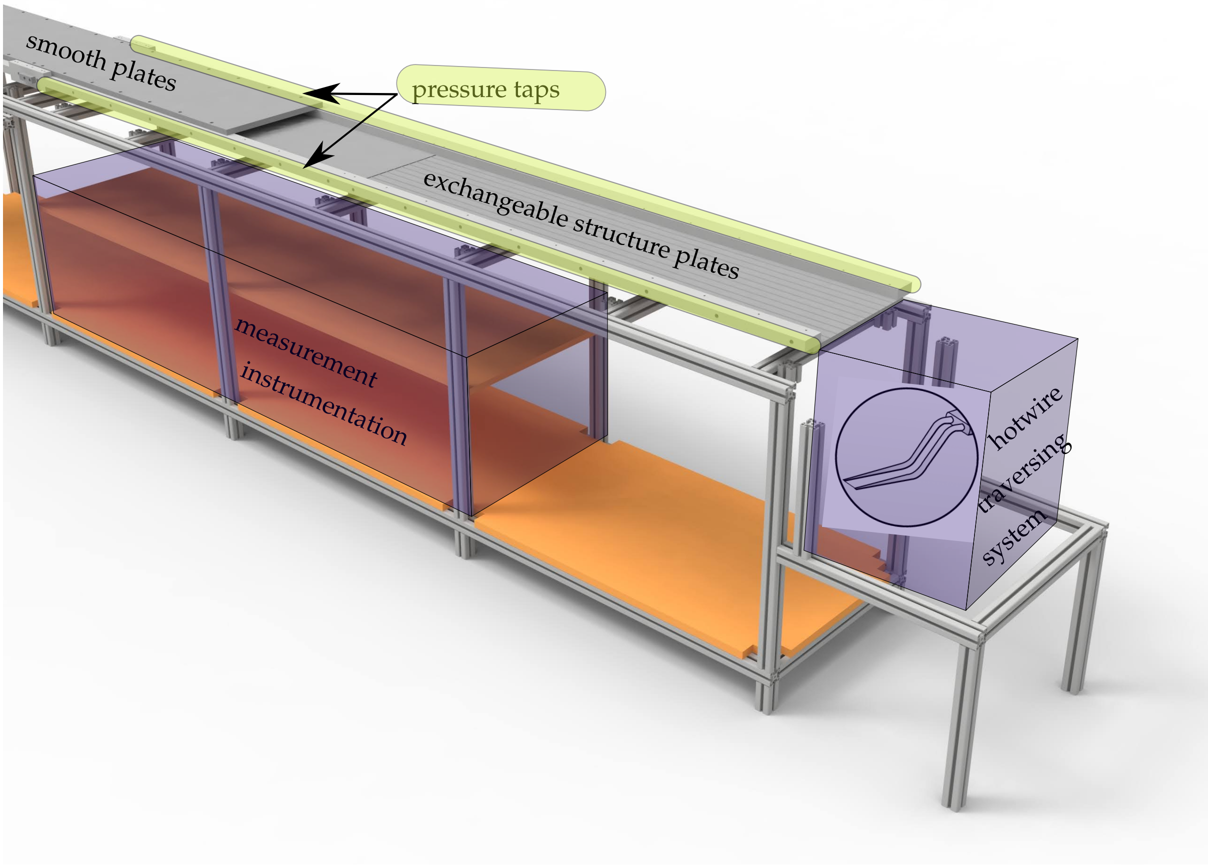

Figure 3.3: Schematic of the test section, where the top plate is removed in the downstream part of the test section.

3.1.1 Pressure-Drop Measurements

"The resulting (effective) wall-shear stress in the considered portion of the channel test section is determined by evaluating the streamwise pressure gradient at a given flow rate. Based on the measured pressure gradient $\Pi = -\frac{\Delta \overline{p}}{\Delta x}$ and the measured mass flow rate $\dot{m} = \dot{V}_o \rho_{in}$ the skin-friction coefficient is computed through

$$C_f = \frac{8 \Pi \delta^3 W_{\text{duct}}^2 \rho}{\dot{m}^2}, \tag{3.2}$$

where ρ denotes the density at the test section's outlet and W_{duct} the test section width. For the pressure measurement, a MKS Baratron 698A unidirectional differential pressure transducer with 1333 Pa maximum range and accuracy of 0.13% of the reading is employed. In order to measure the pressure drop at all streamwise pressure taps, a Scanivalve multiplexer is used, which switches mechanically between the individual pressure taps such that all pressure differences are measured with the same high-accuracy pressure transducer.

The bulk Reynolds number in the test section is constant along its length and computed through

$$Re_b = \frac{\dot{m}}{W_{\text{duct}}\,\rho\,\nu}. \tag{3.3}$$

Measurement Routine

The changes in skin-friction drag ΔC_f are obtained by comparing two consecutive experiments: first, a smooth wall measurement used as a common reference for all structured cases was conducted, followed by skin-friction measurements of the structured plates. The smooth data is fitted with a polynomial function of fifth order for each orifice configuration stated in table 3.1 enabling a comparison at constant flow rate between smooth and structured cases. All measurements are carried out in the most downstream third 1500 mm (or $119\,\delta$) portion of the test section, allowing $194\,\delta$ for flow development. The pressure taps in the second segment are used as a reference to confirm reproducibility between different measurements." [von Deyn et al., 2022a]

Since a single pressure transducer is used for the various pressure taps, sufficient measurement time is needed to ensure converged pressure signals. First of all, before commencing the first measurement of a day, a waiting period of $t_{\text{free}} = 60$ min is required in order to reach a steady state of the facility.

The sampling time t_{samp} is the time during which data is recorded. It has to be chosen such that a converged average value of the measured pressure difference is obtained. The data is sampled at a frequency of $f = 8$ Hz during that time. A higher sampling rate would not be beneficial due to the inert nature of the MKS Baratron pressure transducer, which is unsuitable for measuring dynamic behaviour. The waiting time t_{wait} refers to the time span in which no data is recorded after the multiplexer switches to the next pressure tap. This parameter is essential for the transducer to settle into a steady state again.

After a set of pressure measurements is recorded, which can be used to derive the streamwise pressure gradient, the engine speed is adjusted to record the next C_f vs Re_b data point. t_{change} is the time period during which no data is recorded after the velocity in the test section is adjusted. It serves the same purpose as t_{free} to allow the wind tunnel to settle into a steady state before the subsequent measurement is started. The time parameters are summarised in table 3.2 separated for the different orifice configurations.

inner orifice diameter d	t_{free}	t_{samp}	t_{wait}	t_{change}
60mm	60 min	180 s	45 s	15 min
105mm	60 min	90 s	45 s	15 min
120 mm	60 min	90 s	45 s	20 min
150 mm	60 min	60 s	45 s	20 min

Table 3.2: Time parameters chosen for skin-friction measurements for the different orifice flow meter configurations.

In the present work, the ninth pressure tap pair from the test section inlet is chosen as a reference since at the highest Reynolds number $Re_b \approx 8.5 \times 10^4$, the pressure difference between the first and the last pressure tap pairing would exceed the 1333 Pa range of the Baratron pressure transducer.

In total, a period of approx. 18 min ($d = 150$ mm) up to 40 min ($d = 60$ mm) is needed to obtain a singular data point in the Nikuradse type C_f vs. Re_b diagrams depending on the orifice flow meter configuration.

Measurement Uncertainty

"The measurement uncertainty is quantified via Gaussian error propagation at 95% confidence level, as outlined in the appendix of [38] for the utilised facility. The accumulated uncertainty of C_f is below $\pm 2.7\%$, where the biggest uncertainty contribution stems from the orifice flow rate measurement with $\pm 1.7\%$. Assuming the error in the flow rate measurement to be systematic and considering only the error arising from the measurement instrumentation (i.e. random error sources), the measurement uncertainty for drag change measurements $\Delta C_f / C_{f0}$ (C_{f0} denotes the smooth reference value at matched Re_b) reduces to 0.4% [43]." [von Deyn et al., 2022a]

3.1.2 Hot-Wire Anemometry Set-up

Hot-wire anemometry is employed in the high-precision wind tunnel in order to obtain turbulent velocity statistics. Predominately, a single wire hot-wire probe is used to measure the streamwise velocity at different wall-normal and spanwise positions. Moreover, an X-wire is used to measure velocity information in the cross-plane, for which measurement results are shown in appendix A in comparison to DNS and sPIV measurements.

For the two-component measurements, an off-the-shelf standard Dantec 55P61 miniature X-wire probe is used, whereas the single hot-wire probes are custom-built boundary-layer type probes as shown in the photograph in figure 3.4. The probe replicates a DANTEC 55P15 boundary layer type probe with a 2.5 µm diameter Platinum wire and a sensing length of about 0.5 mm, yielding the recommended wire length-to-diameter ratio of 200 [63]. This results in an inner-scaled wire length of $L^+ \approx 25$ at a friction Reynolds number of $Re_\tau \approx 550$. As shown in §4.3, the custom-built probes are necessary to fully resolve turbulent fluctuations without strong spatial filtering effects due to the relatively small channel half height $\delta = 12.6$ mm.

Figure 3.4: Image of an exemplary custom-built hot-wire probe.

Measurement Routine

A DANTEC Streamline Pro frame in conjunction with a 90C10 constant temperature anemometer (CTA) system is used and operated at a fixed overheat ratio of 80 %. Comparisons between structured and the smooth reference case are carried out at matched flow rates, i.e. setting the same bulk Reynolds number assessed via the orifice flow meter. Table 3.3 shows the selected Reynolds numbers for which hot-wire measurements are commonly conducted. They are chosen to match with standard DNS cases in the smooth cases (as can be seen from the stated Re_{τ_0} values) and are spread over the operating range of the high-precision wind tunnel. $Re_{\tau 0}$ is obtained by fitting the smooth reference measurements with a law of the wall proposed by [65], as discussed in sections §4.2 and §4.3. The sampling times t_{samp} stated in table 3.3 are chosen according to [52] such that recorded energy spectra are converged. As such, $t_{\text{samp}} U_{Cl}/\delta \approx 20000$ turnover times are recorded for each measurement. In table 3.3, Δt^+ denotes the viscous scaled time interval between samples.

Re_b	Re_{τ_0}	f_{samp}	t_{samp}	Δt^+	$t_{\text{samp}} U_{Cl}/\delta$
0.5×10^4	179	60 kHz	60 s	0.05	19170
1.2×10^4	385	60 kHz	26 s	0.25	20112
1.8×10^4	540	60 kHz	18 s	0.49	20748
3.7×10^4	1010	60 kHz	10 s	1.69	22706
5.8×10^4	1516	60 kHz	7 s	3.76	24988

Table 3.3: Reynolds numbers at which hot-wire measurements are carried out with respect to utilised sampling times.

"An offset and gain were applied to the top of the bridge voltage in order to match the voltage range of the 16-bit A/D converter used. In order to avoid aliasing at the higher velocities, an in-built analogue low-pass filter was set up at the Nyquist frequency prior to data acquisition."[von Deyn et al., 2022b]

For one-dimensional wall-normal velocity profile measurements, 39 positions in log-spacing with an automated traversing system are recorded. Since the investigated surface configurations are spanwise heterogeneous, additional 2D scans consisting of 1056 measurement points in the spanwise and wall-normal direction were carried out (z-y-plane). The HWA grid is schematically shown in figure 3.5 for protruding sandpaper strips discussed in §6.7. The 32 measurement points in the spanwise direction are spaced equidistantly in the valley and refined in the vicinity of the structures, while the 33 wall-normal locations are spaced logarithmically.

Calibration Procedure

The velocity calibrations for the hot-wire probes were performed ex-situ in an external high contraction ratio jet facility. The flow is driven by the laboratory building's compressed air supply, while the air temperature is also recorded during the calibration process.

The air velocity is controlled by a pressure regulator and a pneumatic valve system. The pressure difference is recorded with the MKS Baratron pressure transducer that is also used for the skin-friction measurements (see §3.1.1). The values for fluid temperature, velocity and hot-wire voltage are sampled for $10s$ with a frequency of $f_{samp} = 10kHz$.

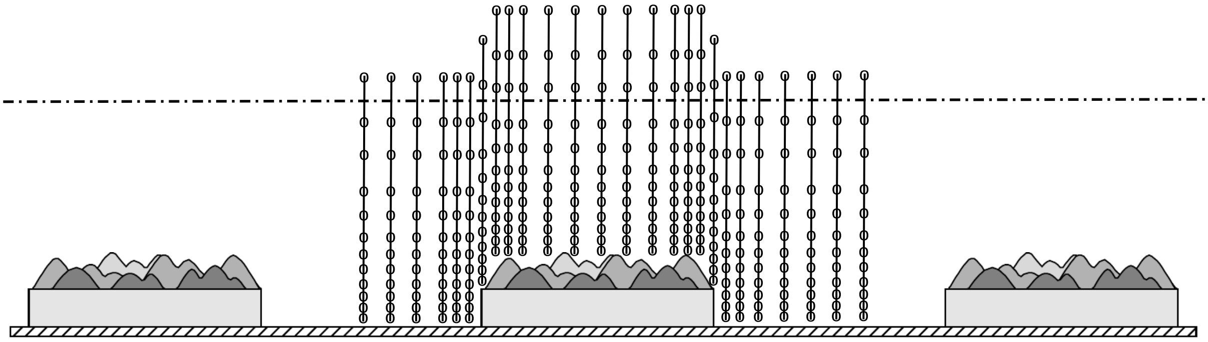

Figure 3.5: Schematic of the HWA grid exemplary shown for protruding sandpaper strips discussed in §6.7. Grid points are spaced logarithmically in wall-normal direct and equidistant in spanwise direct, except that the strip edges are spanwise refined.

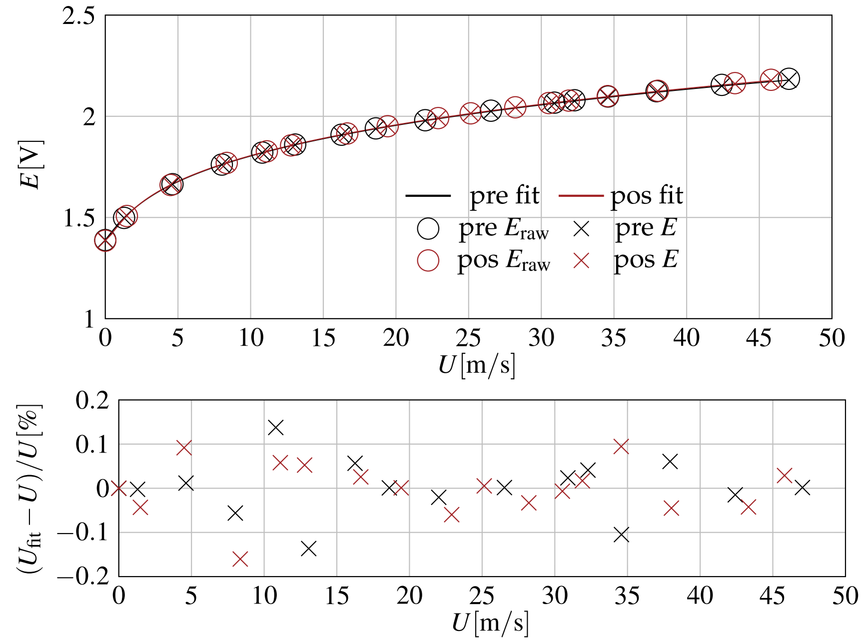

Figure 3.6: Single hot-wire calibration curve. The back markers represent the uncorrected E_{raw} and corrected voltage E with respect to the utilised fit shown as the solid black line. The respective post-measurement calibration is shown in red. In the bottom panel, the relative error of the fit with respect to the calibration velocity U is shown.

An exemplary calibration curve is shown in figure 3.6, where the calibrations before and after the measurement are shown with black or red markers, respectively. A polynomial fit of seventh order is used to convert the recorded voltage E_{raw} into velocity information. The polynomial relation has been chosen instead of a King's law approach since a better calibration fit compared to King's law is expected for small velocities. For all carried out calibrations, no issues with wiggly calibration fits have been observed. The relative error of the fit with respect to the calibration velocity is shown in the bottom panel of figure 3.6 and is always below 0.2 %.

Only small temperature variations are recorded within the high-precision blower tunnel so that temperature effects can be corrected with a linear formula [1]. The measured voltage E_{raw} is corrected as

$$E = E_{\mathrm{raw}} \sqrt{\frac{T_w - T_0}{T_w - T}}, \tag{3.4}$$

where T_w is the wire temperature, T_0 is the reference temperature, and T is the recorded ambient temperature.

Only minimal drift between the pre- and post-measurement calibration is detected, as can be seen in figure 3.6. To further reduce potential drift effects, a linear interpolation method (based on time) is used in order to correct drift effects.

For the calibration of the X-wire probes, an additional angle calibration is required, for which an automated calibrator is used to generate a two-dimensional lookup table. The pre- and post-measurement calibration are shown for an exemplary case in figure 3.7. Each calibration is fitted with a 2D function of seventh order, such that the two recorded voltages E_1 and E_2 are translated into velocity and angle information. As done for the single hot-wire measurements, a linear interpolation between pre and post-measurement calibration (based on time) is used in order to correct for drift effects.

During the X-wire measurement campaign, the u and v velocity and u and w velocity component pairs are measured in two separate campaigns. For this purpose, after the first measurements campaign measuring the streamwise and wall-normal velocity component, the X-wire probe is rotated by precisely 90° and a second measurement is carried out to measure the wall-parallel velocity.

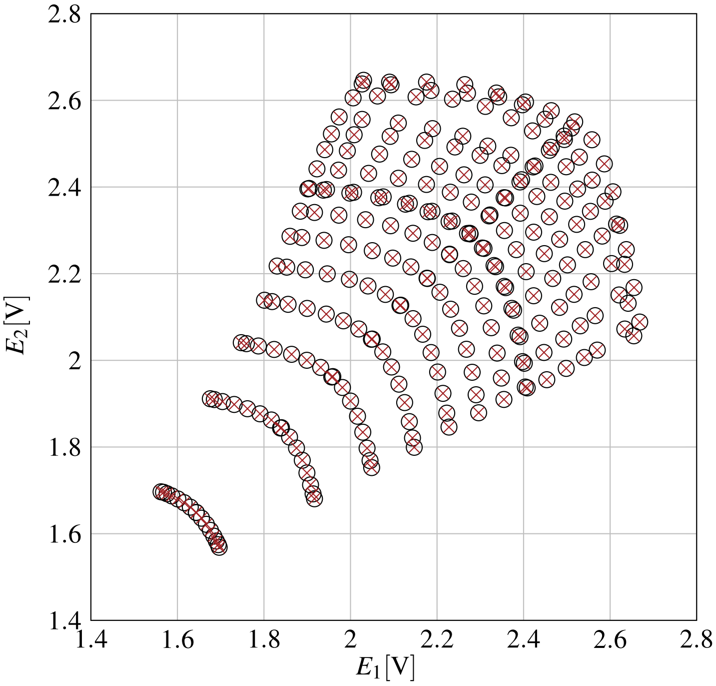

Figure 3.7: Exemplary X-wire calibration used to create a lookup table. Black circles and red crosses represent the pre- and post-measurement calibrations, respectively.

Measurement Uncertainty

Regarding the uncertainty of the employed hot-wire measurements, the major contributions stem from calibration error, temperature and electrical drifts as well as ambient pressure changes, which yields a typical uncertainty of 1-2% of hot-wire measurements [82].

Using linear error propagation and assuming the occurring sensitives are not interconnected, the uncertainty of the current hot-wire measurement set-up is estimated, as this particular set-up is used for the first time and not documented elsewhere.

A key uncertainty to consider is the accuracy of the reference velocity of the external calibrator, which is computed using the expression

$$U_{\mathrm{cal}} = \sqrt{\frac{2\Delta p}{\rho}}, \tag{3.5}$$

which is derived from Bernoulli's equation utilising the measured pressure difference Δp and the ambient density ρ. Using linear error propagation for U_{cal} yields a relative uncertainty of $\sigma_{U_{\mathrm{cal}}} = 0.97\%$

The polynomial used to relate the voltage E with the velocity U

$$U = a_0 + a_1 E + a_2 E^2 + a_3 E^3 + a_4 E^4 + a_5 E^5 + a_6 E^6 + a_7 E^7 \tag{3.6}$$

reveals a maximum relative fit error of $\sigma_{\mathrm{fit}} = 0.2\%$ that needs to be accounted for in the uncertainty propagation. The typical error of the measured voltage is estimated from the calibration with $\sigma_E = 0.2\%$. Note that temperature effects are compensated via equation (3.4) such that uncertainties in the temperature measurements propagate into the computation of U. Inserting all dependencies into equation (3.6) yields U as a function of E_{raw} and T such that the respective sensitivities for the error propagation are derived. The resulting uncertainty σ_U is computed via

$$\sigma_U = \sqrt{\left(\frac{\partial U}{\partial E_{\mathrm{raw}}}\sigma_E\right)^2 + \left(\frac{\partial U}{\partial T}\sigma_T\right)^2 + \sigma_{\mathrm{fit}}^2 + + \sigma_{U_{\mathrm{cal}}}^2}. \tag{3.7}$$

such that the total uncertainty of U amounts to $\sigma_U = 1.17\%$, with the typical uncertainty of the temperature $\sigma_T = 0.5\%$. The discussed relative uncertainties contributing to σ_U are summarized in table 3.4.

error source	σ_E	σ_T	σ_{fit}	$\sigma_{U_{\mathrm{cal}}}$	total σ_U
relative uncertainty	0.2%	0.5%	0.2%	0.97%	1.17%

Table 3.4: Relative uncertainties contributing to the total hot-wire uncertainty σ_U.

3.2 Optically Accessible Blower Wind Tunnel Facility

The investigated spanwise heterogeneous surface structures are expected to induce secondary motions that can be detected in the channel cross-plane. In order to resolve the wall-normal and spanwise velocity components, complementary sPIV measurements were carried out for selected cases. For this experimental campaign, the same wind tunnel structure plates as before are used but in a different facility that is suited for particle-based measurement techniques.

A schematic of the optically accessible blower wind facility is shown in figure 3.8. The flow and the Di-Ethyl-Hexyl-Sebacat (DEHS) seeding particles enter the facility through an exchangeable inlet nozzle, which can be chosen depending on the desired flow rate. The flow is driven by a radial fan placed in the most upstream part of the settling chamber.

Different test sections can be attached to the wind tunnel and for the present campaign, a new test section identical in its dimensions compared to the test section of the high-precision wind tunnel is used. The only differences are that the monolithic rods forming the channel side walls do not contain pressure taps and a 19 mm × 19 mm window is cut out 100 mm upstream of the test section outlet such that the cross-plane can be illuminated by laser light.

As for the pressure-drop and hot-wire measurements, comparison between structured and smooth cases is evaluated at matched flow rates. Although the facility is equipped with inlet nozzles to determine the global flow rate, those do not provide sufficient accuracy for the desired flow rates. Since for all sPIV cases, single hot-wire measurements are available at the desired Re_b, those measurements are utilised to adjust the wind tunnel to the correct speed. For this purpose, a Prandtl tube was positioned at the channel centreline to measure the velocity U_{Cl}. The pressure difference was recorded with the MKS Baratron 698A unidirectional differential pressure transducer otherwise used for high accuracy measurements of the streamwise pressure gradient §3.1.1. With respect to the surface topography, the Prandtl tube is placed at the same location as previously the hot-wire probe. Using the local centreline Reynolds number Re_{Cl} obtained from the hot-wire measurement, the respective Re_{Cl} is matched for the sPIV experiment.

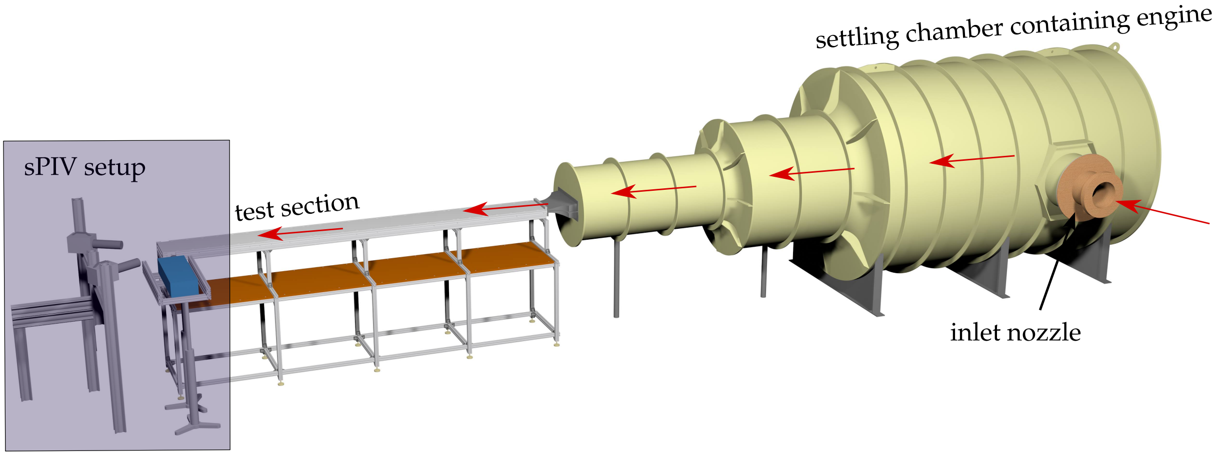

Figure 3.8: Schematic of the optically accessible blower wind tunnel.

Steroscopic Particle Image Velocimetry Set-up

The experimental set-up of the high-speed stereoscopic particle image velocimetry (sPIV) campaign is shown in figure 3.9 as a view on the test section exit. Two Photron SA4 high-speed cameras at the left (camera 1) and right (camera 2) side of the channel exit, positioned at approximately 28° with respect to the streamwise direction, were used to take the particle images. The cameras are positioned outside the jet exiting the test section to avoid blockage effects. Each camera is equipped with Nikon Nikkor lenses with a focal length of 200 mm and an aperture of $f/8$. The lenses are used in conjunction with a tele converter for each lens and mounted on Scheimpflug adapters fitted to accommodate the oblique viewing angles.

The particles were illuminated by a Quantronix Darwin-Duo Nd:YLF laser that accesses the channel test section through the cut-out windows in the side walls. In this window, a cylindrical plan-convex lens of 150 mm focal length is fitted such that the light entering the test section is parallelised, thus avoiding potential reflection issues on the aluminium wind tunnel plates.

The field of view (FOV) with respect to the test section is indicated in figure 3.9. It is placed in the spanwise channel centre to avoid potential side wall effects and has a size of approx $1.2\delta \times 1.2\delta$. This size is chosen as a compromise to resolve potential domain filling secondary motions ($\delta \times \delta$ size) while

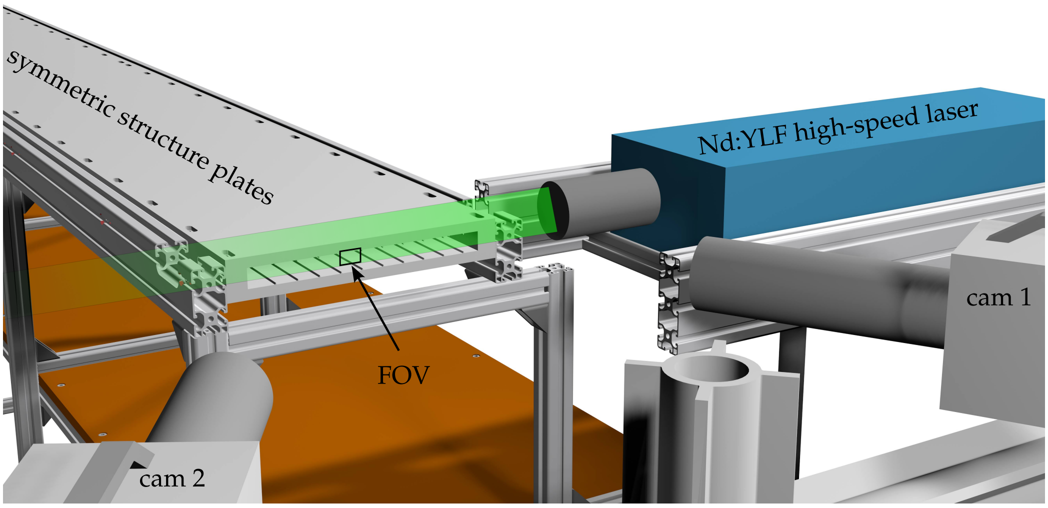

Figure 3.9: Schematic view from downstream on the test section, including the main components of the sPIV set-up.

ensuring a spatial resolution of about 60 px/mm that is necessary to resolve the cross-plane velocity components.

The cameras were operated in double-frame mode (sampling frequency 480 Hz) at full sensor size (1024×1024 px). The light sheet thickness was set to 0.5 mm corresponding to ≈ 30 px. In order to resolve the three velocity components as accurately as possible, an average streamwise displacement of $\Delta x = 10$ px is desired [91]. Hence, the laser pulse distance Δt is adjusted as a function of the centreline velocity U_{Cl}

$$\Delta t = \frac{\Delta x}{60\, U_{Cl}} 10^{-3}. \tag{3.8}$$

Matching Reynolds numbers with the hot-wire measurements are chosen as stated in table 3.3, although the maximum Reynolds number was limited to $Re_b = 3.7 \times 10^4$. Beyond this threshold, vibrations originating from the radial fan were detected. Furthermore, due to the use of the high-speed PIV system, motion blur occurs for higher velocities. If sPIV measurements of higher Re_b are desired, a different engine should be attached to the wind tunnel and a low-speed sPIV set-up should be used.

Due to the limited storage capacity of the employed Photron SA4 high-speed cameras, the particle images of consecutively repeated experiments are combined, while the ambient and operating conditions of the wind tunnel have been closely monitored. For each experiment, 2728 double frames are recorded and afterwards transferred to the data storage before the experiment is repeated. For all considered sPIV cases, combining five consecutive experiments amounting to a total of at least $N = 13640$ image pairs results in converged PIV statistics.

For the processing of the particle images, the software PIVview3C is used with a multigrid/multipass approach, where the raw images were cross-correlated on a final interrogation window size of 48 x 24 px with an overlap factor of 50 %. An averaged background image subtraction was used to avoid reflection issues in the first interrogation area closest to the wall. More details regarding the experimental set-up are documented by Hehner [47], who used the same experimental set-up to characterise plasma actuators in turbulent flow.

Measurement Uncertainty

The utilised sPIV set-up is particularly challenging as the out-of-plane velocity component is at least one order of magnitude larger than the in-plane velocities and thus making it hard to resolve secondary motions of a small magnitude. According to Hehner [47] who conducted an a posteriori uncertainty estimation of the employed set-up following the procedure outlined by Bhattacharya et al. [9], the resulting uncertainties of the mean velocity components U, V, W are stated in table 3.5 , estimated for a smooth wall case with a centreline velocity $U_{Cl} = 5.86\,\mathrm{m/s}$. This corresponds to the relative uncertainties $\Delta U/U_{Cl} = 0.2\,\mathrm{m/s}$, $\Delta V/U_{Cl} = 0.06\,\mathrm{m/s}$ and $\Delta W/U_{Cl} = 0.05\,\mathrm{m/s}$, respectively, when normalising with the centreline velocity.

velocity component	ΔU	ΔV	ΔW
uncertainty	0.2 m/s	0.06 m/s	0.05 m/s

Table 3.5: Relative uncertainties of the mean velocity components estimated by Hehner [47] for the employed sPIV set-up.

As additional information to further assess the limitations of the utilised sPIV set-up, a comparison to DNS and X-wire measurements is shown in appendix A for two surface configurations. The measurement uncertainties stated in table 3.5 agree well with the observed trends and limitations documented in appendix A and §5.5.2.

3.3 Surface Manufacturing

As mentioned in §3.1, the investigated surface structures are introduced in the most downstream part of the test section over a streamwise extent of $119\,\delta$. In physical units, this corresponds to a size of the structured wind tunnel plates of $1500\,\mathrm{mm} \times 300\,\mathrm{mm}$, keeping in mind the aspect ratio $\mathrm{AR} \approx 12$ of the test section.

This size of the structured wind tunnel plates has been chosen as a compromise between competing interests: First, in the experimental investigation, channel flow conditions are desired. Thus, a high aspect ratio as in the present facility is needed such that no effect of the side walls is felt in the spanwise channel centre. To what extent this holds true is discussed in §4.2. Also, a large characteristic length scale δ is desired such that high Reynolds numbers can be studied at moderate flow rates. At the same time, the test section length in terms of δ needs to be sufficiently large such that the streamwise evolution of the pressure gradient can be experimentally assessed. Therefore, the current size was chosen as a compromise. With the correct set-up, it is challenging to manufacture the small $h \approx 1\,\mathrm{mm}$ surface topographies for the required size and precision, but still practicable.

The two-dimensional surface structures discussed in chapter 5 are milled with a high-precision milling machine since the chosen trapezoidal shape can be milled with high precision when utilising the appropriate tools. For the wider spaced configurations (see §5.2 for dimensions), an angle milling cutter is employed that fits into the valley. A disc milling cutter has been used for sawtooth-like shapes, which required substantial machining time but resulted in adequate surface structures. This methodology reaches its limits at $h \approx 1\,\mathrm{mm}$ for the required substantial physical wind tunnel plate dimensions. The smallest surface structures investigated in chapter 5 with $h \ll 1\,\mathrm{mm}$ are specially designed surfaces that were bought externally.

In order to produce the spanwise heterogeneous rough surface configurations discussed in chapter 6, sandpaper was glued on otherwise smooth aluminium wind tunnel plates since the sandpaper is a well-defined standardised roughness. The key challenge in manufacturing the configurations discussed in §6.2 is the correct streamwise alignment of the individual roughness strips. For this purpose, a designated alignment frame has been built and used when glueing the sandpaper onto the carrier plates.

Since the manufacturing of the wind tunnel plates is a key challenge for performing extensive parametric studies and complex structure shapes cannot be manufactured with the conventional methods employed in the present study, an initial attempt is documented in appendix B to introduce additive manufacturing as an alternative approach for producing structured wind tunnel plates. The first results seem promising, although further optimisation is needed for large-scale integration in wind tunnel testing.

4 Smooth Reference Measurements

In this chapter, reference measurements conducted on smooth wind tunnel plates are discussed that serve as a reference for the measurements on spanwise heterogeneous surface topographies in chapters 5 and 6. Emphasis is given to reference measurements exceeding the range discussed in the doctoral thesis of Güttler who originally designed and built the utilized high-precision blower tunnel facility [43]. In the preceding doctoral thesis, an in-depth analysis of the streamwise development of the pressure gradient for different inflow conditions is presented in chapter 5 [43]. In summary, a fully developed turbulent flow is present in the most downstream section ($194\,\delta$ downstream of the test section inlet) of the wind tunnel test section for $Re_b > 4500$ while tripping the flow at the test section inlet with by introducing 13% blockage. This configuration is used in the present investigation and the investigated heterogeneous surface structures are introduced in the most downstream segment of the test section (see §3.3 for more details on the arrangement of the wind tunnel plates).

In the following, measurements on smooth wind tunnel plates are discussed, which are an important reference for the analysis of the heterogeneous surface configurations. This includes pressure-drop measurements (§4.1) of the global friction, the discussion of side wall effects of the aspect ratio AR $\approx$ 12 test section assessed via hot-wire measurements in the cross-plane (§4.2) and the comparison of turbulent statistics obtained via hot-wire measurements to literature DNS (§4.3).

4.1 Skin-Friction Measurements

The pressure-drop measurements of the smooth wind tunnel plates that later (in chapters 5 and 6) serve as a reference to assess the drag change are presented in figure 4.1. The measurement results are shown as black symbols, while the different marks represent different orifice flow meters as defined in table 3.1 which are used to obtain the flow rate (see §3.1).

As references, the correlation proposed by Dean [23], a turbulent analytical solution and DNS data [51] are shown. The turbulent relation is obtained by integrating the approximated wall-normal velocity profile by a logarithmic law of the wall [89] (see also §2.1.2), which yields the expression

$$\sqrt{\frac{2}{C_f}} = \frac{1}{\kappa}\ln\left(\frac{Re_b\sqrt{C_f}}{2\sqrt{2}}\right) + B - \frac{1}{\kappa}. \tag{4.1}$$

The constants are set to $\kappa = 0.39$ and $B = 5$. The smooth reference C_f vs. Re_b measurements shown in figure 4.1 collapse onto the Dean correlation up to $Re_b \approx 6 \times 10^4$ matching the results reported by Güttler [43] who recorded smooth C_f vs. Re_b measurements up to $Re_b \approx 2 \times 10^4$ that collapse onto Dean's correlation [23] as well. Beyond $Re_b \approx 6 \times 10^4$, the present measurements yield slightly higher C_f values compared to the Dean correlation towards $Re_b \approx 8 \times 10^4$. Keeping in mind that the assumptions leading to equation (4.1) improve for high Re_b, the Dean correlation seems to underpredict C_f for high Re_b when compared to the turbulent solution. Thus, the measured slightly higher C_f values towards $Re_b \to 8 \times 10^4$ compared to the Dean correlation seem reasonable. The difference in C_f between DNS and measurement points amounts to $\approx 5\%$ and can be attributed to side wall effects. Note that the well-known Prandtl-von Kármán friction law [113]

$$\frac{1}{\sqrt{4C_f}} = 2\log\left(Re_b\sqrt{4C_f}\right) - 0.8, \tag{4.2}$$

a widely used implicit correlation for the friction factor $\lambda = 4C_f$ of smooth pipe flow, yields higher C_f values compared to equation (4.1) and Dean's correlation. The measured higher C_f values in the test section towards $Re_b \approx 10^5$ thus also tend closer to the smooth pipe flow reference and the question arises whether this trend would continue for skin-friction measurements of $Re_b \gg 10^5$.

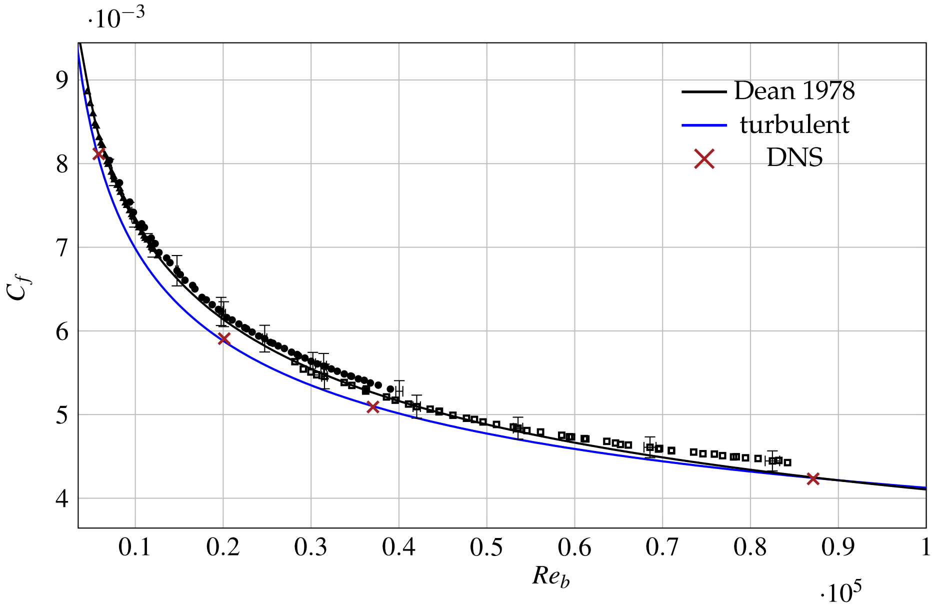

Figure 4.1: Measured C_f vs. Re_b for the smooth reference case, where different markers represent different orifice flow meter dimensions as introduced in table 3.1. Equation (4.1) (blue line) and the correlation proposed by Dean [23](black line) alongside DNS results of Hoyas and Jiménez [51] (red crosses) are included for reference. The horizontal and vertical error bars represent the measurement uncertainty for exemplary data points.

"Locally, e.g. [...] at $Re_b \approx 3 \times 10^4$, small ($< 2\%$) differences of C_f between the different orifice flow meter configurations can be observed. As specified in table 3.1, the different orifice configurations are necessary to cover the full range in Re_b. The observed scatter in the data points is related to systematic uncertainty arising from the flow rate measurement and is within the expected measurement uncertainty discussed in §3.1.1. Also, note that the flow rate uncertainty is a function of the orifice pressure drop Δp_o, increasing non-linearly for small Δp_o. Therefore, the overlap of C_f measurements obtained with different orifices is particularly challenging since one of them must work towards its lower Re_b limit of applicability, as specified in table 3.1, i.e. at low Δp_o and larger uncertainty. However, the offset in C_f induced by the flow rate measurement is independent of the investigated individual surface structure. Therefore, the offset error cancels when evaluating the relative drag change $\frac{C_f - C_{f0}}{C_{f0}} = \frac{\Delta C_f}{C_{f0}}$ or ΔU^+ discussed in [chapters 5 and 6]. In consequence, the resulting uncertainty for these relative quantities is significantly smaller." [von Deyn et al., 2022a].

Overall, the observed deviations from literature data, such as DNS data points and the Dean correlation, lay within a reasonable range.

4.2 Side Wall Effects

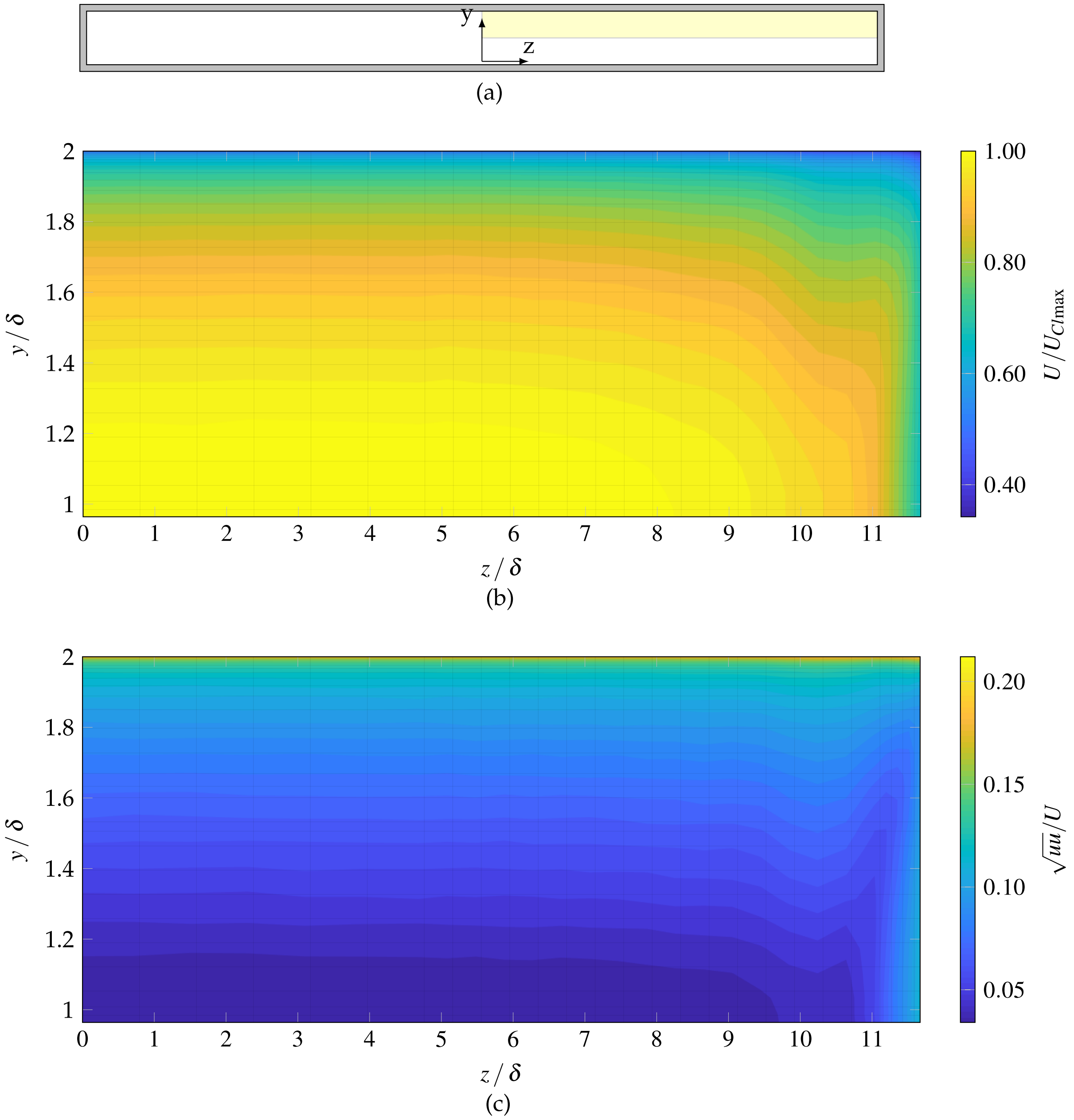

Figure 4.2: Cross-plane hot-wire measurements obtained in the top right quadrant of the test section at $Re_b = 5.8 \times 10^4$. The yellow highlighted area in panel (a) shows the measurement area with respect to the coordinate system. Panel (b) shows $U/U_{Cl\max}$ contours, where $U_{Cl\max}$ is the maximum occurring centreline velocity. Panel (c) shows the local turbulence intensity $\sqrt{\overline{uu}}/U$. The grid intersections shown in the contour plots indicate the measurement points. Note that the aspect ratio of the figure is not 1:1 to fit the page width.

Since in chapters 5 and 6 also 2D velocity statistics are shown obtained from hot-wire and sPIV measurements and compared against DNS utilizing periodic boundary conditions, it is important to assess to what spanwise extent side wall effects can be detected in the turbulent statistics. For this purpose, single hot-wire measurements are carried out in the $y-z$ cross-plane. As discussed in §3.1.2, the measurement grid contains 1056 measurement points with 32 measurement points in spanwise direction equidistantly spaced but refined towards the side wall and 33 logarithmically spaced wall-normal locations. 2D scans at the three different Reynolds numbers $Re_b = 1.8 \times 10^4$, $Re_b = 3.7 \times 10^4$ and $Re_b = 5.8 \times 10^4$ are carried out in the top right quadrant of the test section. The measurement area with respect to the coordinate system is shown in figure 4.2 (a) highlighted as the yellow area.

Figure 4.2 shows the two-dimensional field obtained at the highest Reynolds number $Re_b = 5.8 \times 10^4$ of the mean streamwise velocity U, which is normalised by the maximum centreline velocity $U_{Cl_{\max}}$ (panel 4.2 (b)), as well as the streamwise turbulence intensity $\sqrt{uu}/U$ (panel 4.2 (c)). The grid shown in the contour plots indicates the measurement points. As can be seen from figure 4.2, the contours for mean velocity and turbulence intensity are parallel to the wall for values of up to $z/\delta \approx 7$ which translates to physical coordinates of $z = 88\,\mathrm{mm}$ distance from the duct's spanwise centreline. Hence, in the spanwise duct centre, the desired channel flow conditions are met, i.e. the flow is spanwise uniform. To what extent comparison to spanwise periodic DNS is applicable if measurements are conducted in the spanwise channel centre is assessed in §4.3 . The contour plots for $Reb = 3.7 \times 10^4$ and $Reb = 5.8 \times 10^4$ look very similar and are thus not shown here.

Towards the side wall, the centreline velocity U_{Cl} decreases, while the turbulence intensity increases in the same area. In the area beyond $z/\delta > 10$, a particular behaviour for duct flow is observed, which is depicted in 4.3 without stretching the contour plots to fit the page width. The colour coding is equivalent to the one chosen for figure 4.2. For the corner area very close to the side wall ($y/\delta > 11$), the mean streamwise velocity increases when approaching the top right edge to then drop in the direct wall vicinity. A similar behaviour is evident for the turbulence intensity: near the side wall close to the vertical symmetry plane, an increase in turbulence intensity is observed close to the wall. Moving towards the top wall for the same spanwise position, the turbulence intensity first decreases significantly and then increases again in the top wall's vicinity.

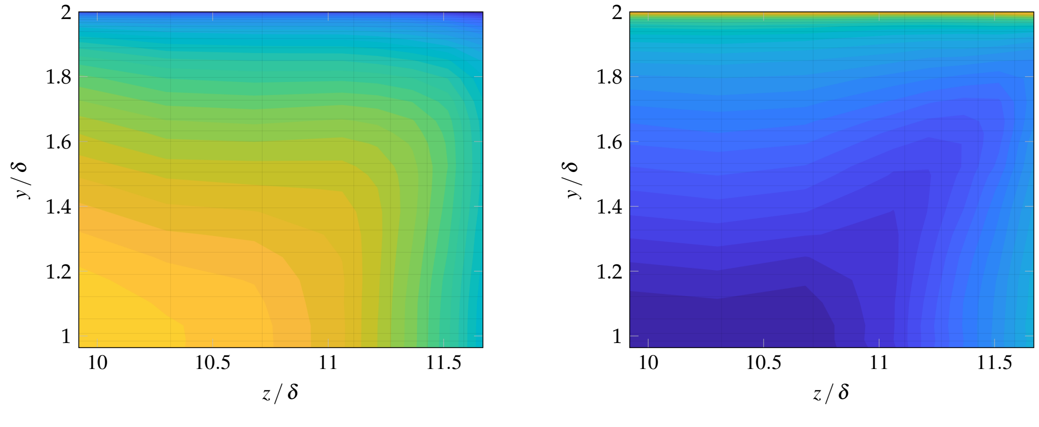

(a) $U/U_{Cl\max}$ contours.

(b) $\sqrt{uu}/U$ contours.

Figure 4.3: Same data as in figure 4.2, but zoomed view on the side wall vicinity ($y/\delta \gtrapprox 10$) without distorting the spanwise axis.

This is related to the emergence of secondary flow of Prandtl's second kind [90], as also discussed in §2.2.3. It is known from DNS of square ducts that secondary motions form an eight vortex pattern [108] such that faster fluid is pushed towards the corners along the corner bisectors [73]. A similar topology is maintained in the side wall vicinity when the aspect ratio is increased (schematically shown in figure 4.4, as confirmed by Vinuesa et al. [112] who carried out DNS of rectangular duct flow up to an aspect ratio of $AR = 7$. The footprint of the eight vortices is detected by the current hot-wire measurements such that a higher mean velocity and lower turbulence intensity are detected along the corner bisector, as shown in figure 4.3.

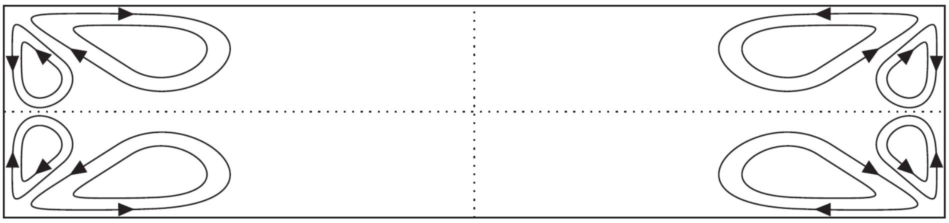

Figure 4.4: Qualitative depiction of the secondary flow of Prandtl's second kind in a rectangular duct according to Hoagland [50].

As a further criterion in order to quantify the spanwise distance until homogenous flow conditions are present, the local wall-shear stress is assessed. To this end, each acquired wall-normal velocity profile is fitted against a formulation of the viscous scaled mean velocity profile $U^+(y^+)$ proposed by Luchini [65] which includes a formulation for the buffer layer. In this formulation, the constants of the law of the wall are set to $\kappa = 0.392$ and $B_L = 4.48$, while seven additional fit coefficients are used for the buffer layer formulation. Note that the buffer layer formulation is weighted with an exponential function decreasing with the wall distance. Thus, $B_L = 4.48$ is not directly comparable to the otherwise stated additive constant B of the law of the wall. By fitting the data points against said law of the wall, the a priori unknown wall-offset of the first hot-wire measurement point y_0 and the friction velocity u_τ (and in consequence τ_w) is obtained.

The resulting spanwise distribution of the local wall shear stress τ_w is shown in figure 4.5 for the three Reynolds numbers $Re_b = 1.8 \times 10^4$, $Re_b = 3.7 \times 10^4$ and $Re_b = 5.8 \times 10^4$. In panel (a), τ_w is normalized with the maximum occurring wall-shear stress $\tau_{w\max}$ at the spanwise channel centre. The respective friction Reynolds numbers amount to $Re_{\tau_0} = 540$, $Re_{\tau_0} = 1010$ and $Re_{\tau_0} = 1516$, respectively. The obtained local wall shear stress ratio $\tau_w/\tau_{w\max} \approx 1$ does remain constant up to $z/\delta \approx 5$ for all three Reynolds numbers. Beyond this threshold, the ratio decreases, i.e. an effect of the side walls starts to occur.

Analysis of the spanwise distribution of the centreline velocity, i.e. the maximum streamwise velocity recorded for each wall-normal velocity profile, revealed spanwise homogeneity up to $z/\delta \approx 7$, as also observed in figure 4.2. Hence, the more conservative criterion based on the local wall shear stress distribution is used as a cut-off point. As a consequence, 2D velocity measurements are always carried out in the spanwise channel centre, never exceeding $z/\delta = 5$.

In panel (b), normalisation with the global wall shear stress $\tau_{w\Delta p}$ obtained from the pressure-drop measurements at matched Re_b is utilised. The criterion $z/\delta = 5$ also remains valid in this representation. However, now the difference between the local and global τ_w can be assessed: For $Re_b = 1.8 \times 10^4$ and $Re_b = 3.7 \times 10^4$, the local wall shear stress τ_w is five per cent smaller than $\tau_{w\Delta p}$, while for $Re_b = 5.8 \times 10^4$ the difference increases to 5.7 %.

4.3 Comparison to Plane Channel Flow

In the following, single hot-wire measurements are discussed in order to assess whether the turbulent flow conditions in the spanwise centre of the test section match the turbulent properties expected for plane turbulent channel flow. All measurements presented in this section are recorded at $z = 0$.

A Dantec gold-plated wire probe of type 55P05 is used to record wall-normal velocity profiles at different streamwise distances from the test section outlet instead of the otherwise used custom-built hot-wire probes described in §3.1.2. In doing so, it is assessed if the outlet of the wind tunnel has an upstream ef-

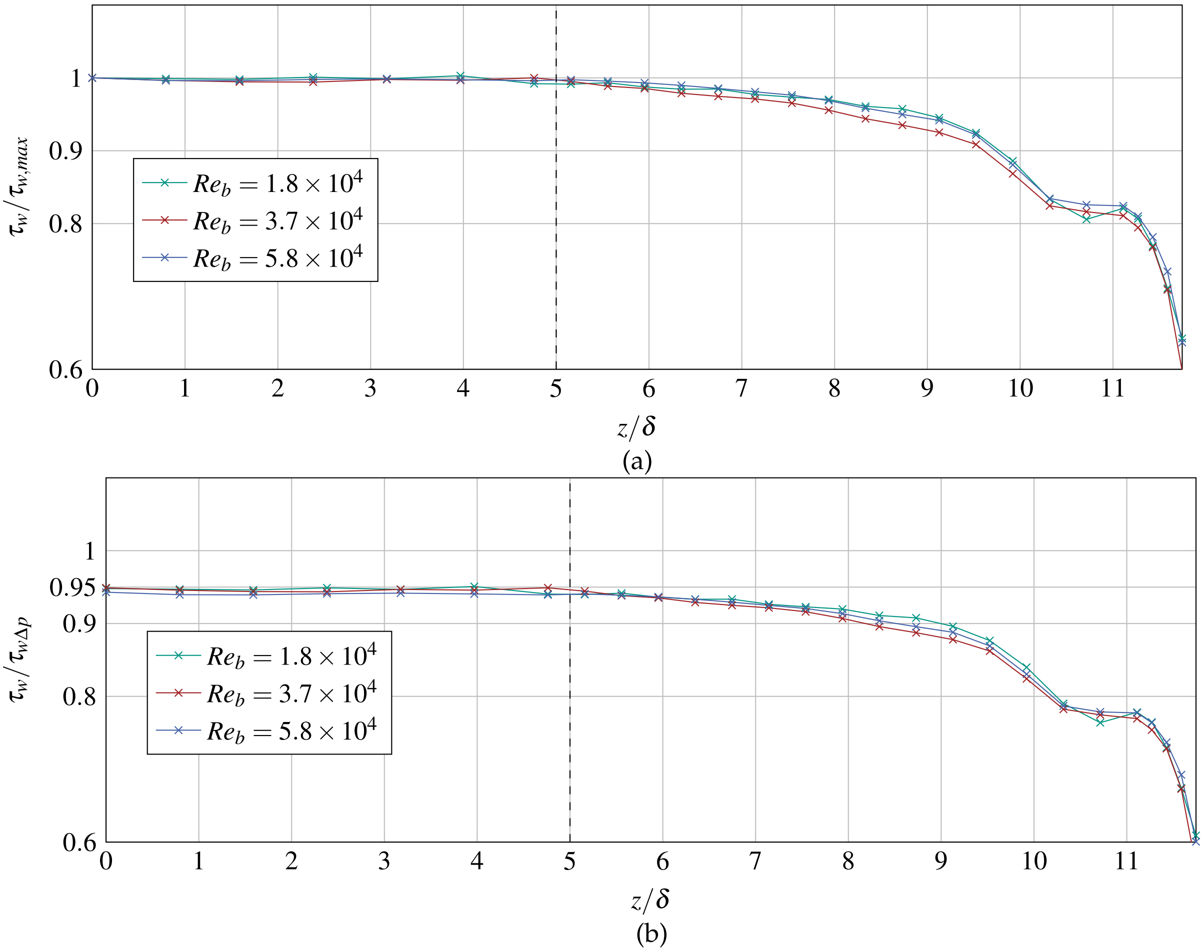

Figure 4.5: Spanwise wall shear stress τ_w distribution. Panel (a): normalisation with the maximum wall shear stress $\tau_{w\max}$. Panel (b): normalisation with wall shear stress $\tau_{w\Delta p}$ obtained from the pressure-drop measurements at matched Re_b. The vertical dashed line indicates the spanwise limit $z/\delta \approx 5$ for a spanwise homogeneous wall shear stress distribution.

fect on the turbulent properties. The measurements are carried out at $Re_b = 1.8 \times 10^4$ and the streamwise distance is set to 0, 1, 5 10 and 15 cm upstream of the test section. As described in the preceding section §4.2, the measured velocity profile is fitted against a law of the wall $U^+(y^+)$ proposed by Luchini [65]. In doing so, the local friction velocity u_τ and the otherwise unknown wall distance of the first measurement point y_0 are obtained. Based on the local u_τ, $Re_b = 1.8 \times 10^4$ corresponds to $Re_\tau = 540$. It is avoided to define u_τ based on the available pressure-drop measurements on this occasion since the discussed side wall effects in §4.2 lead to an increase in friction (see §4.1) and comparison to plane channel flow is desired.

In figure 4.6, the obtained viscous-scaled mean velocity U^+ and Reynolds stresses uu^+ profiles are shown in panel (a) and (b), respectively. DNS [51] at $Re_\tau = 550$ is included for reference in figure 4.6. As can be seen from panel (a), all $U^+(y^+)$ profiles recorded inside the test section collapse with the reference DNS. Only the profile measured directly at the test section outlet depicted as the yellow line deviates substantially from the expected turbulent profile.

For the Reynolds stresses, substantial spatial filtering effects occur such that the recorded profiles for all streamwise positions lay well below the DNS reference. This stems from the relatively large wire length of $L \approx 3\,\text{mm}$ with respect to the characteristic length scale, i.e. the channel half height $\delta = 12.6\,\text{mm}$. This corresponds to $L^+ \approx 125$ in viscous scaling. As observed for the U^+ profiles, the Reynolds stresses uu^+

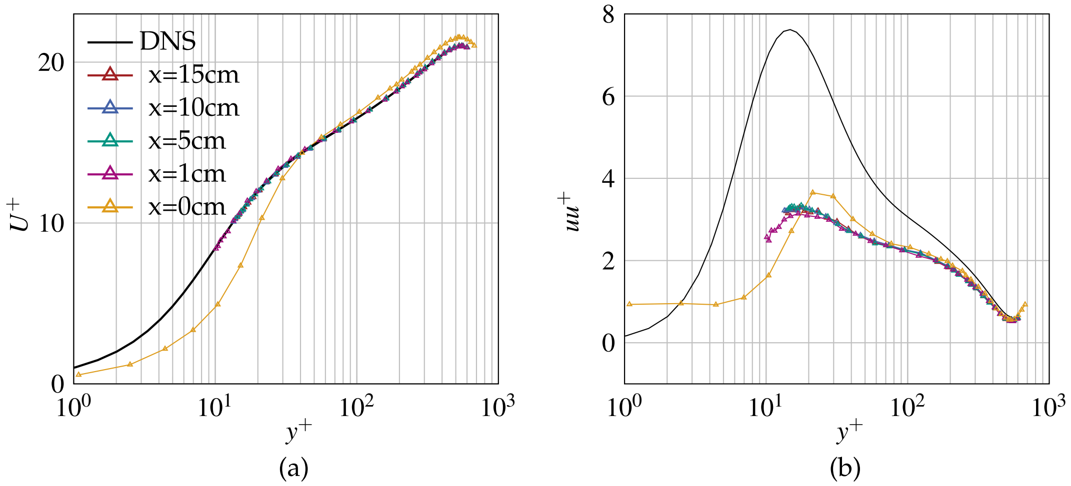

(a) (b)

Figure 4.6: Viscous-scaled single hot-wire measurements for different streamwise distances from the test section outlet obtained at $Re_b = 1.8 \times 10^4$ which corresponds to $Re_\tau = 540$. Panel (a): Mean streamwise velocity U^+. Panel (b): Reynolds stress uu^+. DNS of Hoyas and Jiménez [51] with $Re_\tau = 550$ included for reference. Legend of panel (a) is also valid for panel (b).

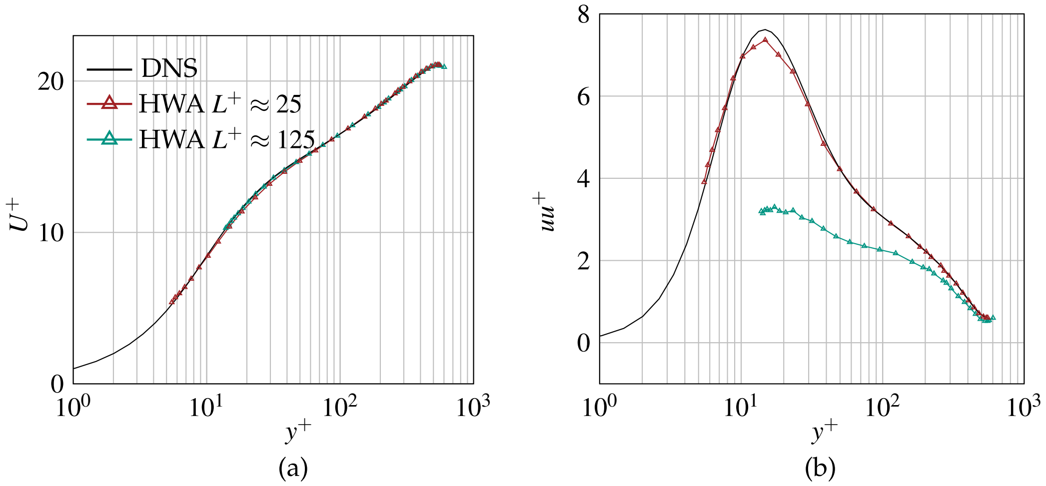

(a) (b)

Figure 4.7: Effect of wire length on turbulent statistics. Measurements obtained at $Re_b = 1.8 \times 10^4$ which corresponds to $Re_\tau = 540$. Panel (a): Mean streamwise velocity U^+. Panel (b): Reynolds stress uu^+. DNS of Hoyas and Jiménez [51] with $Re_\tau = 550$ included for reference. Legend of panel (a) is also valid for panel (b). "HWA $L^+ \approx 25$" denotes the custom-built hot-wire probes used in the present work (see 3.1.2). "HWA $L^+ \approx 125$" refers to a Dantec type 55P05 gold-plated wire probe.

collapse reasonably well within the wind tunnel section while a deviating signal is recorded only directly at the outlet. Therefore, all hot-wire measurements discussed in the following are conducted at a streamwise distance of 1 cm upstream of the test section outlet since the obtained statistics match the reference DNS and a position close to the outlet is desirable due to the better visibility of the hot-wire probe.

The importance of the custom built hot-wire probes introduced in §3.1.2 is illustrated in figure 4.7, where turbulent statistics obtained at $Re_b = 1.8 \times 10^4$ ($Re_\tau = 540$) for two different hot-wire probes are plotted against DNS [51] conducted at $Re_\tau = 550$. The results measured with the custom-built hot-wire probe with an active length of 0.5 mm ($L^+ \approx 25$ at $Re_\tau = 540$) depicted in red are shown in comparison to the DNS and the profiles measured with the gold-plated wire probe Dantec type 55P05 probe with $L^+ \approx 125$. As expected from literature [52], the turbulent statistics are almost correctly resolved with the custom-built miniature probe, i.e. matching reasonably well with the DNS reference. The error for a wire length $L^+ = 20$ is expected to be below 14 % [52], which matches the observed difference between HWA and

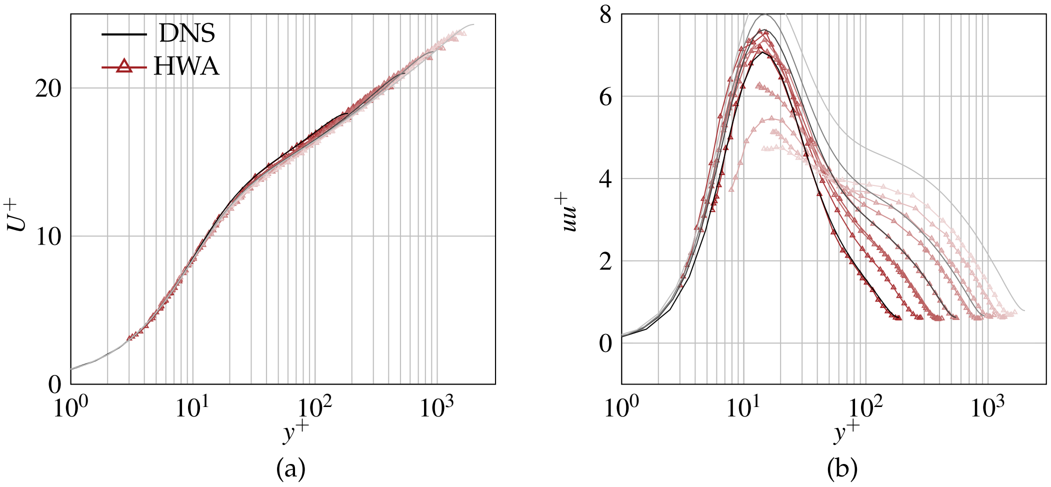

Figure 4.8: Viscous-scaled single hot-wire measurements for different Reynolds number numbers ranging from $Re_b = 0.5 \times 10^4$ ($Re_\tau = 179$) up to $Re_b = 5.8 \times 10^4$ ($Re_\tau = 1516$). Lighter colours represent increasing Reynolds numbers. In shades of black, DNS results of Hoyas and Jiménez [51] with $Re_\tau = 180, 550, 950$ and $Re_\tau = 2000$ are included for reference. Panel (a): Mean streamwise velocity U^+. Panel (b): Reynolds stress uu^+. Legend of panel (a) is also valid for panel (b).

DNS in 4.7 (b). Consequently, it is reasonable that the uu^+ profile recorded with the custom-built hot-wire probe lays slightly below the DNS reference in figure 4.7 (b). That leads to the conclusion to show only HWA measurements recorded with the custom-built hot-wire probes in chapters 5 and 6. Note that beyond $Re_b = 1.8 \times 10^4$ also for these probes, spatial filtering effects are expected to increase since the wire length is kept constant, i.e. L^+ increases.

This can be seen in figure 4.8, where hot-wire measurements utilizing the custom-built hot-wire probes over a wide Reynolds number range are presented. Starting from $Re_b = 0.5 \times 10^4$ the Reynolds number is increased up to $Re_b = 5.8 \times 10^4$, which corresponds to $Re_\tau = 179$ and $Re_\tau = 1516$, respectively. Lighter colours denote increasing Reynolds number in figure 4.8. As before, the DNS results of Hoyas and Jiménez [51] are included for reference, this time all available cases $Re_\tau = 180, 550, 950$ and $Re_\tau = 2000$. As expected, the mean velocity profiles shown in panel (a) of figure 4.8 agree very well with the respective DNS references when a local u_τ is used. Considering panel (b), since the physical size of the hot-wire probe remains unchanged for all measurements, the viscous-scaled hot-wire length increases from $L^+ = 6.6$ up to $L^+ = 56$ with the expected effect on uu^+.

Overall, the measured turbulent statistics match the expected conditions, while the limitations of the applied measurement techniques need to be kept in mind (i.e. effects of the hot-wire sensing length). Generally speaking, comparing recorded experimental data to (DNS) channel flow results is applicable.

5 Drag of Streamwise Aligned Surface Structures

As a first step in order to gain further insights into the drag behaviour of spanwise heterogeneous surface topographies, the drag of streamwise aligned trapezoidal grooves is experimentally investigated. After introducing the common terminology of riblets and ridges adopted from literature, an overview of the eight investigated surface configurations is given (§5.2). The procedure to define the channel half-height based on laminar flow solutions for the individual surface topographies is described in detail in §5.3. Afterwards, the resulting skin-friction measurements are discussed in detail (§5.4) with respect to different choices of the wall-normal origin and occurring drag regimes. To enable comparison to velocity measurements in literature and provide insight into the local flow in the vicinity of the triangular structures, selected hot-wire and sPIV measurements are presented in §5.5. The results discussed in this chapter were partially published in [von Deyn et al., 2022a].

5.1 Drag Reducing Riblets vs Drag Increasing Ridges

"Two dimensional (2D) surface structures aligned with the main flow direction and periodically repeating with a wavelength s in the direction perpendicular to it have been extensively studied over the last decades due to their capability to alter momentum and heat transfer properties of turbulent flows. Besides the details of the surface geometry, their height h and spacing s relative to the viscous length scale ν/u_τ determines the effect that such surfaces have on skin-friction drag [35, 41].

[...] Small riblets are surfaces that, when spaced at a wavelength of $s^+ \approx 15$, are known to reduce skin-friction drag up to 10% in canonical flows at low values of Reynolds number [7]. Various riblet shapes have been tested [115] and trapezoidal-grooved riblets, which yield 8.2% maximum drag reduction in similar conditions, are deemed a good compromise between drag-reducing performance, feasible manufacturing and durability [7].

On the other hand, significantly larger streamwise invariant surface structures exceeding 100 viscous units in size typically yield the opposite effect and increase skin-friction drag. These drag-increasing structures, named ridges, are object of many recent studies, see e.g. [53, 69, 104], where they are employed as a simplified model for laterally inhomogeneous roughness. Such roughness configurations are observed in a variety of natural and industrial turbulent flows, such as river bed flows [20] or flows over ablated turbine blades [4]. Incorporating lateral inhomogeneities in roughness predictions remains an unsolved challenge [16] and simplified 2D structures can serve as means to address the effect of spanwise inhomogeneities on skin-friction drag explicitly.

Despite the geometrical similarity of riblets and ridges, their skin-friction drag characteristics have not been related so far. Given the similarity, it is conceivable that observations and predictions made for riblets might extend to ridges and vice versa, and thus the question arises if a unifying framework can be found to describe the drag properties of both surfaces. Since we will frequently refer to the terms riblets and ridges in the following, it is worth considering whether a tentative quantitative distinction between these two structures can be proposed. Generally speaking, a 2D surface is termed riblet if it can yield drag reduction, a capability which depends on the specific operating range and dimensions of the experimental facility. However, it is known (see, for instance [24]) that typical riblet geometry such as the presently investigated trapezoidal grooves achieve drag reduction when the viscous-scaled square root of the groove area l_g^+ [36], i.e. the fluid area between two consecutive riblet crests, is $l_g^+ < 17$ (see also figure 5.1 (a)). Moreover, riblets reduce drag only in turbulent flows [7] such that the lower bound of the viscous scaled half-channel height δ^+ (i.e. the friction Reynolds number) has to be beyond $\delta^+ \approx 100$. Thus, only 2D structures that fulfil

$$\frac{l_g}{\delta} \lesssim 0.17 \tag{5.1}$$

can potentially lead to drag reduction. Such structures are referred to as riblets throughout the [thesis]. Thus, the distinction between riblets and ridges is purely terminological and we intend to provide experimental evidence by assessing the drag behaviour of surfaces characterised by $l_g/\delta < 0.17$ (riblets) and surfaces that exceed $l_g/\delta > 0.17$ (ridges).

Currently, only the skin-friction drag of small 2D riblets is predictable from the geometrical properties of the surface alone. In the so-called viscous or linear regime of riblets, the flow in the riblet vicinity is dominated by viscosity and thus, its behaviour can be described via Stokes flow solutions. Luchini et al. [66] characterised the flow above riblets with a streamwise and spanwise protrusion height, $h_\parallel$ and $h_\perp$, respectively. The protrusion height is measured as the distance below the riblet tips at which the spatially-averaged velocity profile obtained from the Stokes solution above the riblet tips predicts a zero velocity when extrapolated towards the wall. In this context, $h_\parallel$ is associated with the streamwise flow and $h_\perp$ accounts for the virtual origin perceived by the predominant turbulence effect in the wall vicinity, i.e. the spanwise velocity fluctuations. If $h_\perp$ is located closer to the riblet crest than $h_\parallel$, i.e. the virtual origin perceived by turbulent eddies is displaced further into the flow than the one perceived by the mean flow, the skin-friction drag is reduced. Quantitatively, $\Delta U^+ = -(h_\parallel^+ - h_\perp^+)$ holds for riblet sizes in the order of the viscous sublayer of the turbulent flow [66]. [...] Grüneberger and Hage [42] experimentally confirmed the drag behaviour suggested for very small riblets based on the protrusion height difference $h_\parallel^+ - h_\perp^+$, which corresponds to a linear relation between drag reduction and l_g^+. This behaviour is referred to as the viscous regime, which breaks down once the riblet size substantially exceeds the viscous sublayer. While the protrusion height difference captures the amount of achievable drag reduction, l_g^+ has been shown to be an appropriate choice of length scale to describe the collapse of the drag reducing regime for different riblet types [36].

Ridges are known to induce drag increase [69]. This drag increase can be quantified through the roughness function ΔU^+ if the mean velocity profile exhibits a logarithmic law of the wall similar to smooth wall turbulence. The downward shift of the logarithmic region of the rough wall velocity profile compared to the smooth wall one is given by ΔU^+ [16]. For rough surfaces (in particular so-called k-type roughness [59]) ΔU^+ increases linearly (slope $1/\kappa$) with the logarithm of the viscous scaled roughness size in the fully-rough regime.

The typical drag behaviour of 2D surfaces is sketched in figure 5.1, here panel a) shows ΔU^+ as a function of l_g^+. As noted before, negative ΔU^+ indicates drag reduction. Concerning riblets, we observe the linear viscous region, after which the breakdown of the viscous regime begins with the maximum drag reduction reached at $l_g^+ \approx 11$ [36]. A further increase of l_g^+ leads to an increasing friction with $\Delta U^+ = 0$ at $l_g^+ \approx 17$. The occurrence of secondary flows consisting of matched pairs of streamwise vortices [41] or alternatively the emergence of Kelvin–Helmholtz (KH) instabilities were proposed [37] as the mechanisms underlying the drag increase of riblets. Recent studies exploiting direct numerical simulations (DNS) in minimal channels indicate that KH-instabilities contribute to an increase of ΔU^+, but are not solely responsible for the breakdown of the viscous drag-reduction regime of riblets [24]. In fact, only sharp-triangular and blade riblets show a significant friction contribution of KH-rollers [24], whereas the breakdown of the viscous regime inevitably occurs for all riblets. Furthermore, Modesti et al. [72] showed that secondary flows significantly contribute to ΔU^+ for various riblet shapes by analysing the dispersive stresses as a footprint of secondary flows." [von Deyn et al., 2022a]

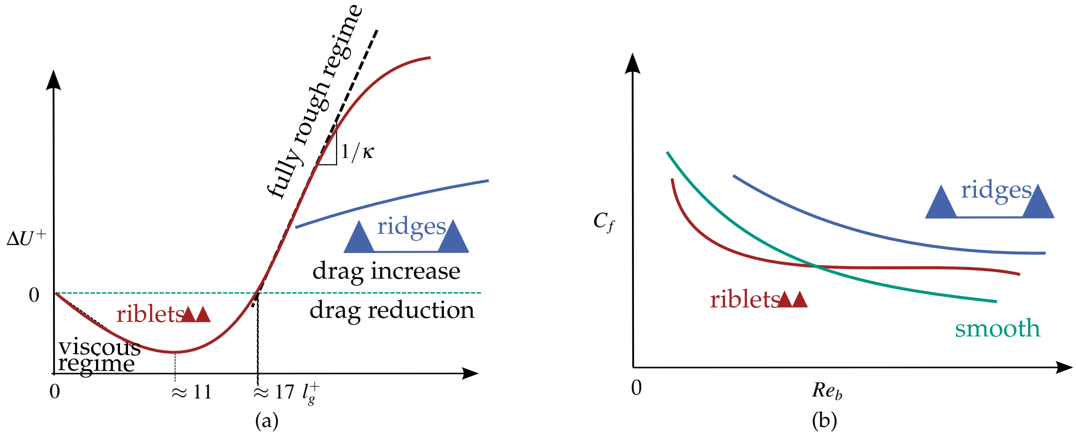

(a)

(b)

Figure 5.1: Schematic of different drag regimes. Hypothetical curves inspired by [Gatti et al., 2020] for riblets and by Medjnoun et al. [69] for ridges. Figure adopted from [von Deyn et al., 2022a].

5.2 Overview of Investigated 2D Surfaces

"For the present investigation, eight sets of 2D trapezoidal groove geometries of varying height h and spacing s are considered (see figure 5.2 for geometrical definitions), which are installed on both channel walls symmetrically in the most downstream $119\,\delta$ of the test section. All cases are listed in table 5.1. The naming convention is introduced following the distinction between riblets and ridges outlined in [§5.1]: an ID starting with dr refers to potentially drag reducing riblets with $l_g/\delta < 0.17$ and purely drag increasing ridges that exceed $l_g/\delta > 0.17$ are termed di.

The number part of the ID represents the ratio of the wavelength s and the base width of the riblet/ridge s_r, i.e. dr_1a$\cdots$dr_1c are sawtooth riblets (where $s = s_r$), while di_13 are widely spaced ridges. Both h and s are systematically varied over one order of magnitude. For the interested reader, note that mean flow data of di_13 up to $Re_b = 5 \times 10^4$ is discussed in [von Deyn et al., 2022b]. Moreover, set dr_2 corresponds to the one discussed in [Gatti et al., 2020]. In doing so, the evolution of the drag change with respect to a smooth surface is studied, starting from very small drag-reducing riblets submerged in the viscous sublayer up to widely-spaced drag-increasing ridges that protrude into the logarithmic flow region and are known to induce large scale secondary motions [69]. Note that di_2 was purposely designed as an enlarged trapezoidal riblet geometry. To quantify the increase in wetted surface area, the perimeter P to spanwise wavelength ratio P/s is included in table 5.1. For each geometry, the Stokes-flow solution (see §5.3) is computed to obtain the protrusion height values $h_\parallel$ and $h_\perp$.

The changes in skin-friction drag ΔC_f are obtained by comparing two consecutive experiments: first, a smooth wall measurement used as a common reference for all structured cases was conducted, followed by skin-friction measurements of the structured plates. The smooth data is fitted with a polynomial function of fifth order for each orifice configuration stated in table 3.1 enabling a comparison at constant flow rate between smooth and structured cases. All measurements are carried out in the most downstream third 1500 mm (or $119\,\delta$) portion of the test section, allowing $194\,\delta$ for flow development. The pressure taps in the second segment are used as a reference to confirm reproducibility between different measurements. The investigated structures were milled in 1500 mm-long aluminium plates with a high precision CNC milling machine, with the exception of sets dr_1a & dr_1b, which consist of a riblet foil manufactured by 3M glued onto aluminium plates. The net channel half-height $\widetilde{\delta}_{\mathrm{avg}}$, defined as the distance between the channel centreline and the average structure height h_{avg} (see figure 5.2), is adjusted to match the smooth reference value of $\delta = 12.6\,\mathrm{mm}$. In doing so, the net fluid volume in the channel is kept identical between different cases. [To achieve this, both side interfaces of the structured plates, where the structure plates are connected with the monolithic side rods, are elevated equivalent to h_{avg} such that the net fluid volume remains constant. This is achieved while milling the trapezoidal grooves, i.e. the whole spanwise distribution of the respective riblet/ridge configuration is offset by h_{avg}.] This set-up was initially chosen as we considered $\widetilde{\delta}_{\mathrm{avg}}$ an appropriate channel height for the comparison among different types of riblets and ridges. As it will be discussed in section 5.4.1, a more physically sound choice for interpreting the measurements is δ based on $h_{\|}$. Thanks to the use of dimensionless numbers, the choice of channel height in the experimental set-up can easily be converted to other choices in the data evaluation.

The geometrical parameters stated in table 5.1 were verified via optical (Sensofar S neox) and tactile measurements (perthometer Mahr MarSurf PCV). Next to the geometrical parameters s, h, s_r and α as defined in figure 5.2, the square root of the groove area l_g and the perimeter P are included in table 5.1." [von Deyn et al., 2022a]

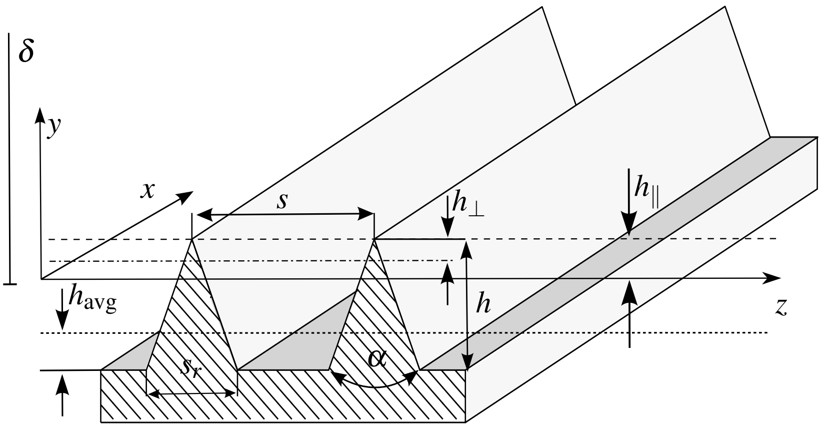

Figure 5.2: Sketch of investigated surface structures. $h_\|$ and $h_\perp$ represent streamwise and spanwise protrusion height [66], h_{avg} the averaged (melt-down) height. The half-channel height δ is defined as the distance between the channel centre line and $h_\|$ below the structure tip. Figure adopted from [von Deyn et al., 2022a].

5.3 Definition of the Wall-Normal Origin

"The wall-normal origin of the channel [is placed] at the streamwise protrusion height $h_\|$ below the structures tip for the present study (see figure 5.2). This ensures that the surface structures do not induce any drag variation under laminar flow conditions, as discussed in the following. In §5.4.1 we present the evaluated drag-change for alternative channel height definitions.

In order to determine $h_\|$ and $h_\perp$, a Stokes flow problem given by

$$-\frac{1}{\rho}\frac{\partial p}{\partial x_i} + \nu \frac{\partial^2 u_i}{\partial x_j \partial x_j} = 0 \tag{5.2}$$

in conjunction with the conservation of mass is solved numerically [...] via finite elements utilising the software FreeFem++ [46]." [von Deyn et al., 2022a]

ID	s[mm]	h[mm]	s/δ	h/δ	s/s_r	α [°]	l_g/δ	l_g/s	P/s	$h_{\|}/s$ $\times 10^{-1}$	$h_{\perp}/s$ $\times 10^{-2}$	η_c
dr_1a	0.086	0.09	0.0068	0.0072	1	51.1	0.0049	0.709	2.31	1.791	8.083	-
dr_1b	0.17	0.18	0.0136	0.0144	1	50.6	0.0099	0.729	2.34	1.795	8.089	-
dr_1c	1	0.87	0.0808	0.0703	1	60	0.0533	0.660	2.01	1.707	8.017	-
dr_2	0.614	0.294	0.0492	0.0235	2.07	53.5	0.0302	0.614	1.59	1.744	8.021	-
di_2	5.31	2	0.4423	0.1666	2.3	60	0.2401	0.543	1.44	1.643	7.946	0.933
di_4	9.23	2	0.7569	0.1639	4	60	0.3295	0.435	1.25	1.359	7.865	0.956
di_8	18.48	2	1.4909	0.1614	8	60	0.4749	0.319	1.13	0.869	6.538	0.97
di_13	27.31	2	2.1572	0.158	13.2	54.8	0.5726	0.265	1.09	0.635	5.23	0.974

Table 5.1: Dimensions of the investigated geometries as introduced in figure 5.2. P denotes the perimeter, l_g is the square root of the groove area [36]. $h_{\|}$, $h_{\perp}$ are the streamwise and spanwise protrusion heights measured from the tip [66]. η_c representing a constant hydraulic channel height relation $\delta_{\mathrm{hyd}}/\delta$ =const. (see equation (5.7) for definition of δ_{hyd}) obtained a posteriori from figure 5.12. Table adopted from [von Deyn et al., 2022a].

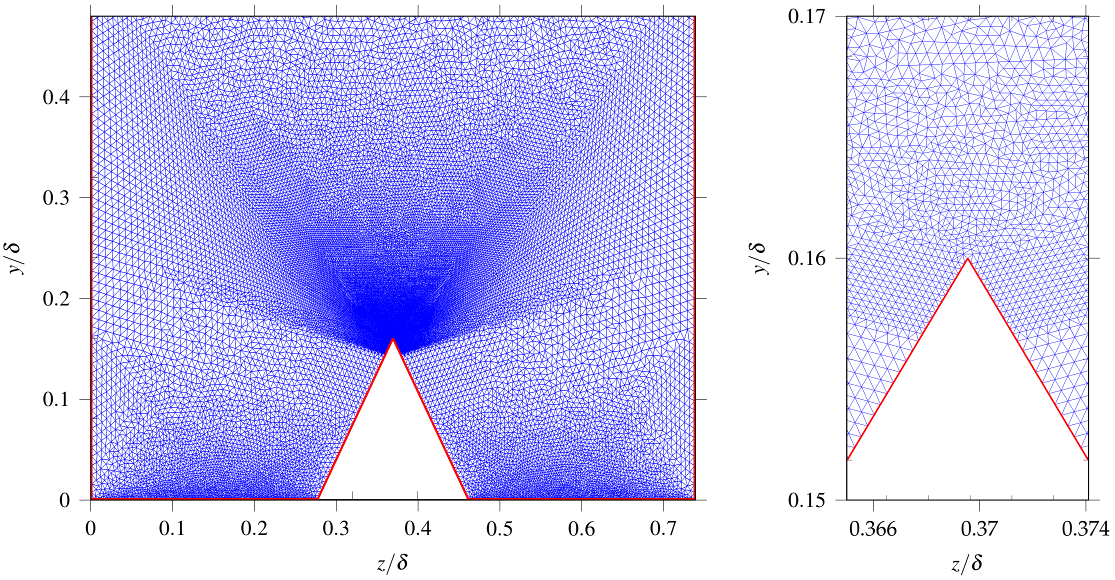

(a) (b)

Figure 5.3: Mesh used to compute the Stokes solutions for the surface di_4. Panel (a) shows the bottom half of the domain, while panel (b) shows a zoomed-in view of the structure's tip.

Figure 5.3 shows an exemplary mesh for the surface configuration di_4. The tip region is strongly refined to adequately resolve the Stokes solution, especially for flow perpendicular to the surface structure, as highlighted in the zoomed-in view of panel (b) in figure 5.3. As boundary conditions, a no-slip boundary condition is prescribed at the wall, while the velocity at the wall distance of the smooth reference case δ is set to a prescribed value U_{Cl} = const. Hence, Couette flow is considered in order to obtain $h_{\|}$ and $h_{\perp}$.

The procedure to retrieve $h_{\|}$ is visualised in figure 5.4: in panel (a), the resulting Stokes solution for streamwise flow aligned with the surface structuring is exemplarily shown for set di_4. After spanwise averaging the velocity U, the velocity profile is fitted with a linear function in the region well above the surface crest $y/\delta > 0.3$. The structure's crest is indicated in figure 5.4 (b) with the green vertical line. The position at which the linear fit depicted as the red line in figure 5.4 (b) predicts zero velocity (indicated as the yellow vertical line) marks the definition of the streamwise protrusion height $h_{\|}$.

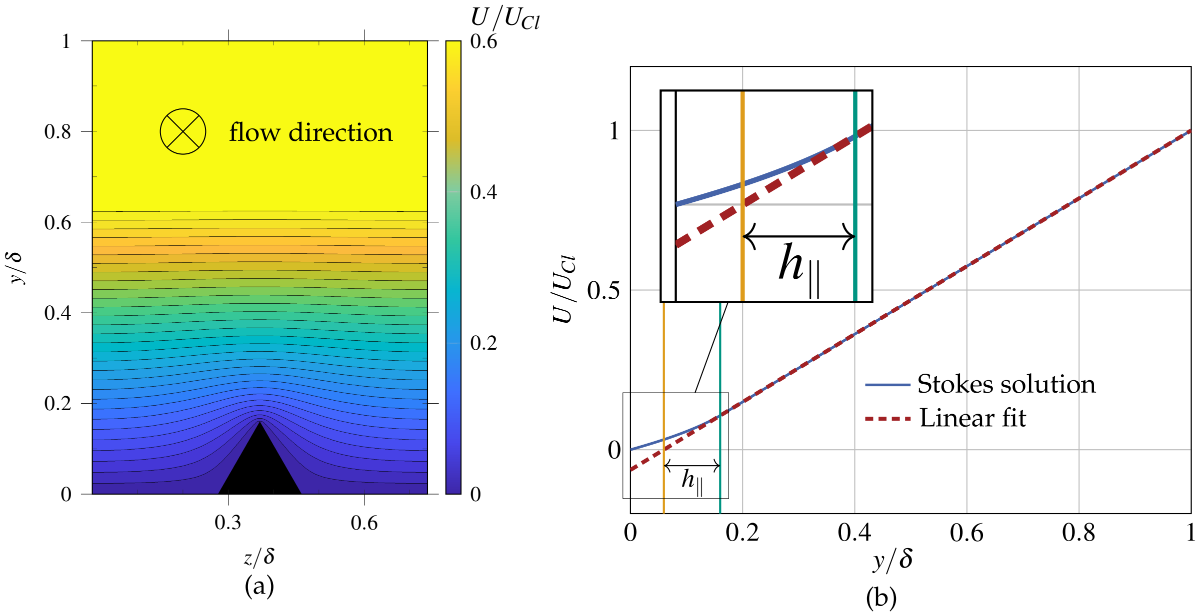

(a)

(b)

Figure 5.4: Stokes solution for shear flow aligned with the surface structure di_4. Panel (a) shows the streamwise velocity U. In panel (b), the procedure to obtain $h_\|$ is visualised based on the spanwise averaged velocity profile U shown as the blue line. The structure's tip is indicated by the green vertical line, while the yellow line marks $h_\|$.

Note that for this flow configuration, "equation (5.2) simplifies to the Laplace equation $\nabla^2 u = 0$ [...] and analytical solutions can be found in case of two-dimensional structures via conformal mapping [6]. [Thus,] the procedure [has been] validated against the analytical solution and literature references [7, 66]." [von Deyn et al., 2022a]

The Stokes solution for perpendicular flow for set di_4 is shown in figure 5.5, while panel (a) shows the spanwise velocity component W and panel (b) the vertical velocity V. This configuration is used to obtain $h_\perp$ in analogy to the procedure discussed above and highlighted in figure 5.4 (b) except that this time W is considered to retrieve $h_\perp$. The values of $h_\|$ and $h_\perp$ obtained with this procedure are included in table 5.1.

"For the present surface structures $h_\perp$ is located closer to the structure tip compared to $h_\|$, as visualized in figure 5.2. The figure also includes the melt-down height h_{avg}, which is located closer to the bottom of the surface structure.

For the investigated two-dimensional surface structures, the laminar channel flow solution and the Stokes flow solution for $h_\|$ coincide. Therefore, the channel height definition based on $h_\|$, as indicated in figure 5.2, provides a set-up in which the well-known $C_f - Re_b$-relation for laminar channel flow ($C_f = 12/Re_b$) also applies for a channel with riblets. Thus, by choosing the current definition of δ, we focus on the surface structure influence on turbulent drag since the laminar drag of smooth and structured channels is identical by definition. This is in agreement with the drag reduction prediction for the viscous regime as briefly outlined in §5.1, which suggests zero drag change for vanishing viscous scaled riblet size [66]." [von Deyn et al., 2022a]

5.4 Skin-Friction Measurements

"In order to assess the skin-friction drag and identify respective drag regimes, the pressure-drop measurement results obtained for all surface structures specified in table 5.1 and the smooth reference are analysed in the following. The skin-friction coefficient C_f as a function of Re_b is presented in figure 5.6.

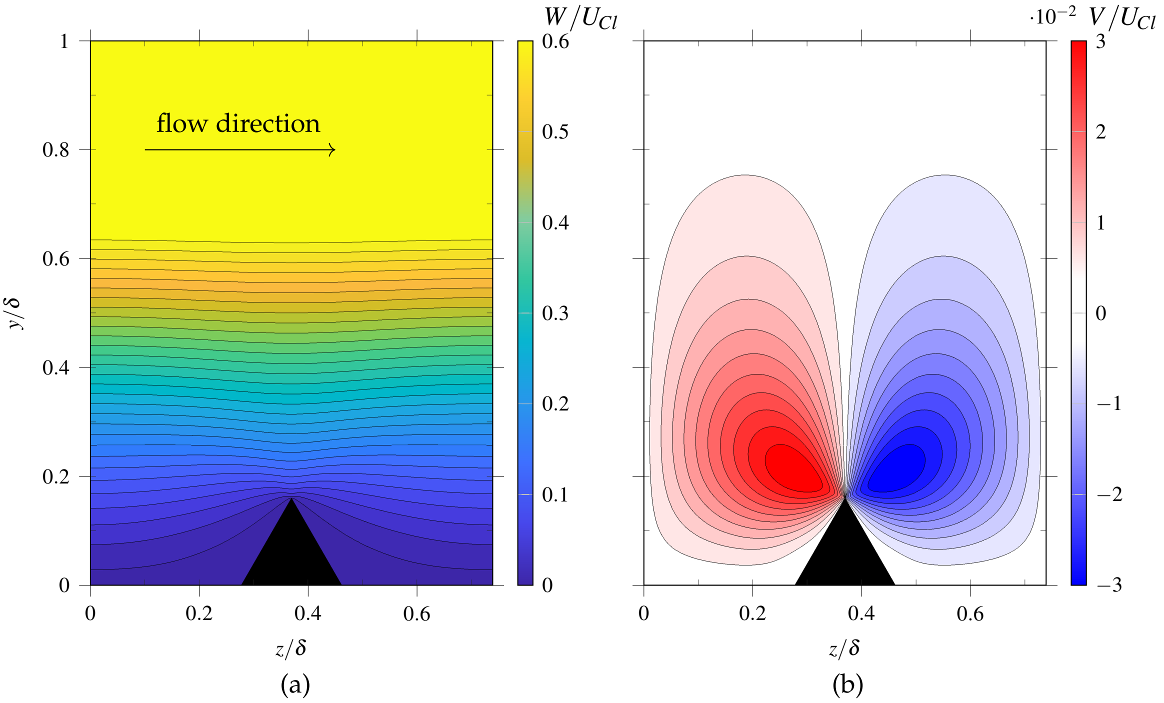

(a)

(b)

Figure 5.5: Stokes solution for shear flow perpendicular to the surface structure di_4. Panel (a) shows the spanwise velocity W, while panel (b) depicts the wall-normal velocity V.

The smooth results are shown as black markers with respect to the well-known correlation proposed by Dean [23]. The different markers denote the varying orifice flow meter size employed to measure the volumetric flow rate (see section 3.1). Overall, the reference results show very good agreement with the Dean correlation with detected deviations below 2.7%, i.e. within the measurement uncertainty margin. Also, note that the data collected by Dean [23] to derive his famous correlation is subject to significant scatter.

The colour code is introduced following the distinction between riblets and ridges: riblet data is depicted with red symbols in different shades, while ridge data is shown in shades of blue. Lighter colours indicate physically smaller riblets or more widely spaced ridges. Sets dr_1a$\cdots$dr_1c and dr_2 are at least partially located below the smooth reference in the Nikuradse type diagram of figure 5.6 indicating that these surfaces reduce skin-friction drag in this particular Reynolds number range in the present facility. The drag-reducing effect scales in viscous units [7], thus the drag-reducing regime of the different structures is shifted to lower Re_b with increasing ID/colour intensity (a,b,c and 2) due to their increasing physical size. All drag-increasing structures (in blue) reveal a monotonically decreasing C_f with increasing Re_b, indicating that none of the investigated geometries reaches an apparent fully-rough (i.e. C_f independent of Re_b) flow state in the investigated Reynolds number range.

The physically larger riblet sets dr_1c ($l_g/\delta = 0.0533$) and dr_2 ($l_g/\delta = 0.0302$) are one order of magnitude larger than the smallest riblet set dr_1a ($l_g/\delta = 0.0049$). The transition from a drag-reducing to a drag-increasing behaviour within the present Reynolds number range, exhibiting a region of constant C_f for a limited range of Reynolds number before eventually showing a similar $C_f(Re_b)$ behaviour as the drag-increasing ridges. A trace of nearly constant C_f is also present for di_2 ($l_g/\delta = 0.2401$) at very low Reynolds numbers, which hints at a similarity between the two surface structures di_2 and dr_2.

The measurement results of the differently spaced ridge configurations reveal that narrower spaced ridges (darker blue colour) of the same element height produce more skin-friction drag compared to

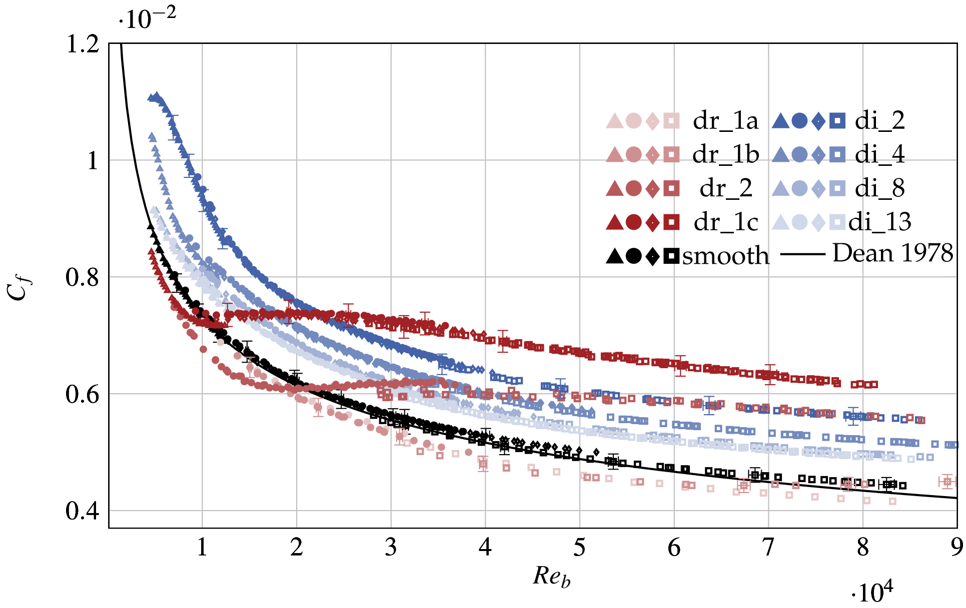

Figure 5.6: Skin-friction coefficient C_f as a function of the bulk Reynolds number Re_b. Different markers indicate different orifice diameters as introduced in table 3.1. Riblets (dr: drag-reducing) are depicted in red, and ridges (di: purely drag increasing) are shown in blue. The reference measurements (black markers) are shown in comparison to the correlation proposed by [23]. The horizontal and vertical error bars represent the measurement uncertainty for exemplary data points. Figure adopted from [von Deyn et al., 2022a].

wider spaced ridges, i.e. skin-friction drag increases with increasing perimeter P to wavelength s ratio P/s. However, we observe that the increase in C_f is not simply proportional to the ratio P/s. A further discussion of this geometrical parameter is presented in §5.4.2."[von Deyn et al., 2022a]

5.4.1 Implications of the Channel Height Definition

"As discussed in §2.2, the arbitrary choice of the effective channel half-height directly affects C_f and many other flow quantities. In the present work, the wall-normal origin has been placed at a streamwise protrusion height $h_{\parallel}$ below the surface crest, which is the position where the far-wall Stokes flow oriented in the mean turbulent flow direction predicts zero average velocity. For non-planar surfaces, the resulting channel half-height δ differs from the average channel half-height $\widetilde{\delta}_{\text{avg}}$, which is defined as the distance between the average structure height h_{avg}, see figure 5.2, and the channel centerline. This definition is commonly used for rough surfaces due to its relatively easy accessibility [13].

In order to show that the present choice of the effective channel height is particularly suited to assess the effect of 2D structures on turbulent drag, we compare how the relative drag change varies when it is computed assuming [different] channel half-height [definitions other than] δ. [Note that the same experimental data sets are utilized for this comparison. The resulting $\Delta C_f/C_{f0}$ and l_g^+ values are rescaled a posteriori using different choices of the half channel half height.] For the sake of clarity, quantities computed with $\widetilde{\delta}_{\text{avg}}$ are denoted with $\widetilde{(\cdot)}$.

The corresponding results for $\Delta C_f/C_{f0}$ are presented in figure 5.7 for the riblet data sets, where panel (a) shows $\Delta\widetilde{C}_f/\widetilde{C}_{f0}$. Utilizing $\widetilde{\delta}_{\text{avg}}$ as channel half-height, i.e. placing the wall-normal origin at the average (melt-down) height, corresponds to comparing $\widetilde{C}_f$ of the structured surface against $\widetilde{C}_{f0}$ of a reference channel with the same cross-sectional area and at the same Re_b. The physically small ($h < 0.3\,\text{mm}$, i.e. $h/\delta < 0.0235$) riblet sets dr_1a,dr_1b and dr_2 show the expected negative $\Delta\widetilde{C}_f/\widetilde{C}_{f0}$, in agreement with previous wall-shear stress balance results of [7]. Compared at the same viscous-scaled riblet size, one

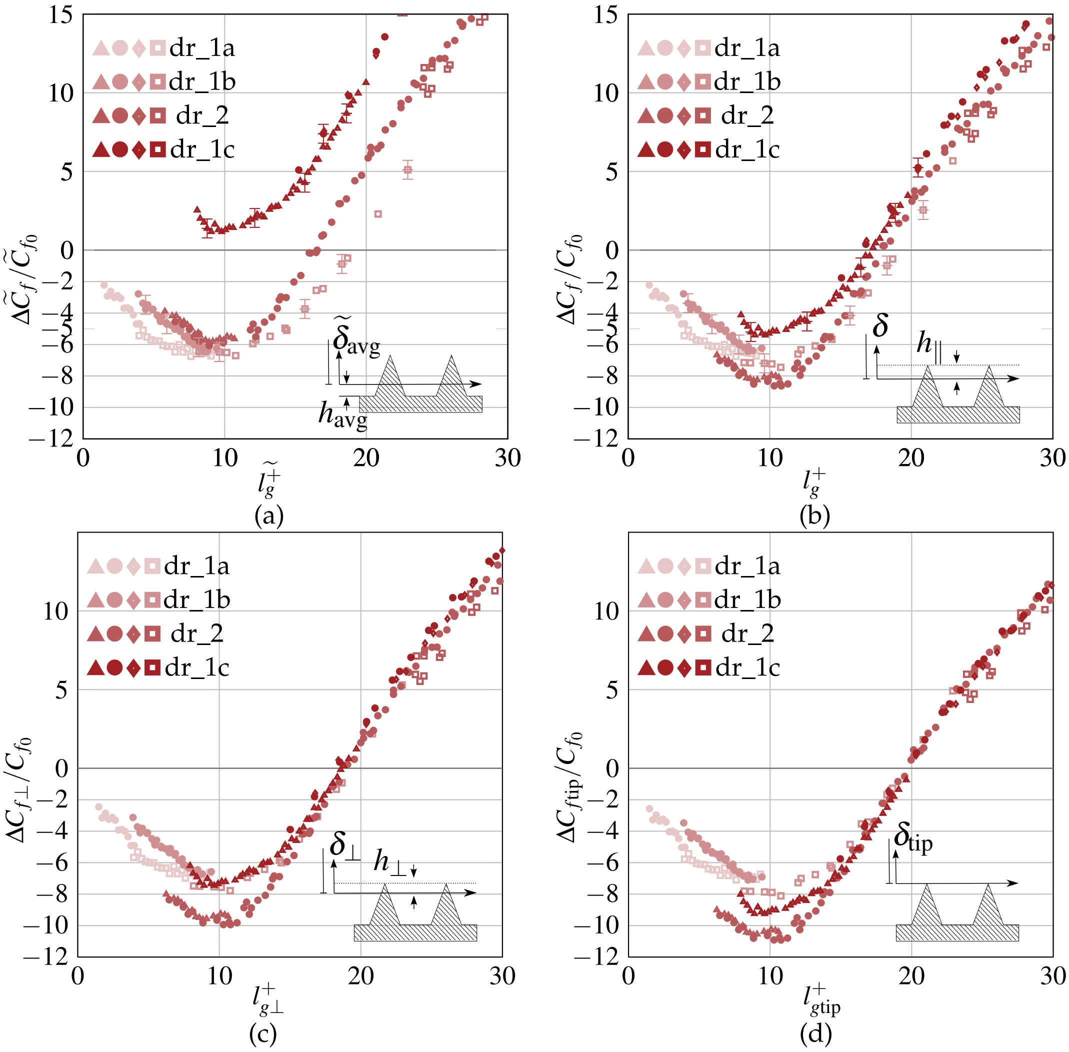

(a) (b) (c) (d)

Figure 5.7: Relative drag change $\Delta C_f/C_{f0}$ vs. the viscous-scaled square root of the groove cross-sectional area l_g^+. Zoomed view on $\Delta C_f/C_{f0} < 0$. Panel (a): Wall-normal origin placed at the averaged structure (melt-down) height h_{avg}. $\widetilde{()}$ used to denote the change of the wall-normal origin to h_{avg} above the structure valley. Panel (b): Wall-normal origin placed $h_\parallel$ below the structure crest. The vertical error bars in panels (a) and (b) represent the measurement uncertainty for exemplary data points. The horizontal error bars are negligible in this representation. Panel (c): wall-normal origin placed $h_\perp$ below the structure crest. Panel (d): wall-normal origin placed at the structure tip. Figure adopted from [von Deyn et al., 2022a].

would expect the geometrically similar but physically larger data set dr_1c ($h/\delta = 0.0703$) to behave similarly to dr_1a, dr_1b. However, this is clearly not the case as shown in figure 5.7(a), where $\Delta\widetilde{C}_f/\widetilde{C}_{f0}$ is generally positive for dr_1c. Moreover, the zero crossing $\Delta\widetilde{C}_f/\widetilde{C}_{f0} = 0$ for data sets dr_1b and dr_2 does not occur at $l_g^+ \approx 17$, as commonly reported for riblets [24, 35]. Therefore, even though $\Delta\widetilde{C}_f/\widetilde{C}_{f0}$ is an easily accessible quantity and thus might seem favourable at first glance, considering the drag change at matched cross-sectional area and flow rate does not result in collapsing drag curves for different data sets and yields evidence contrasting the present understanding of riblets from literature.

As an alternative, panel (b) of figure 5.7 shows $\Delta C_f/C_{f0}$. Note that δ is generally smaller than $\widetilde{\delta}_{\mathrm{avg}}$ for structured surfaces. Thus, utilising δ as channel half-height corresponds to comparing C_f of the structured surface against C_{f0} of a reference channel with a slightly larger cross-sectional area and at the same Re_b. The data presented in panel (b) can be directly related to the $\widetilde{\delta}_{\text{avg}}$-based scaling via the following expressions:

$$\frac{\Delta C_f}{C_{f0}} = \Big(\frac{\Delta \widetilde{C}_f}{C_{f0}} + 1\Big)\frac{\delta^3}{\widetilde{\delta}^3_{\text{avg}}} - 1\,, \qquad l_g^+ = \widetilde{l}_g^+\sqrt{\frac{\delta}{\widetilde{\delta}_{\text{avg}}}}\,. \tag{5.3}$$

[These expression are derived from (3.2), where it can be seen that $C_f \sim \delta^3$. Hereby, the same experimental data is used, only the half channel height is changed to a different value.] In comparison to panel (a), the differences are largest for the physically large riblets. This is due to the fact that in case of the physically smallest set dr_1a (h/δ=0.0072) δ is only 0.2% smaller compared to $\widetilde{\delta}_{\text{avg}}$, while for dr_1c ($h/\delta$=0.0703) the two heights differ by 2.2%. In panel (b), the expected $\Delta C_f/C_{f0}$ behaviour is recovered. All riblet data sets yield negative $\Delta C_f/C_{f0}$ for small l_g^+ and a better data collapse around the zero crossing at $l_g^+ \approx 17$ is obtained. This indicates that the $h_{\|}$ based definition of δ is better suited to compare data sets of strongly varying physical size at the additional expense of evaluating the Stokes flow solution.

In the drag reducing regime, sets dr_1a,dr_1b and dr_2 exhibit the expected $\Delta C_f/C_{f0}$ trends, while set dr_1c yields 38% less maximum $\Delta C_f/C_{f0}$ compared to the geometrically similar sets dr_1a,dr_1b. This is a result of the challenging manufacturing process: instead of the desired sharp tips, set dr_1c has rounded tips with 70 µm curvature radius, i.e $R/s = 0.07$. In this respect data set dr_1c agrees well with the findings of [114], who reported 40% decrease of $\Delta C_f/C_{f0}$ for a tip radius to spanwise spacing ratio of $R/s = 0.08$. Note that only the maximum $\Delta C_f/C_{f0}$ is affected by the tip rounding, while the optimum $\Delta C_f/C_{f0}$ still occurs at $l_g^+ \approx 11$, as previously discussed by [36]. It is noteworthy that sets dr_1a and dr_1b are expected to collapse due to their geometric similarity. The visible deviations and slightly smaller $\Delta C_f/C_{f0}$ of dr_1b can be an effect of local imperfections visually observable on the 3M riblet foils."[von Deyn et al., 2022a]

Also note that it is expected that Reynolds number effects impact the reported values of $\Delta C_f/C_{f0}$, i.e. for higher Re_b, smaller values of $\Delta C_f/C_{f0}$ are expected [101]. In literature, also other channel height definitions are discussed other than δ and $\widetilde{\delta}_{\text{avg}}$. "Other common choices include channel heights based on the spanwise protrusion height (see e.g. [54]) or the structure crests (see e.g. [99]). In figure 5.7 [panels (c) and (d)] , the drag change results for riblets are re-scaled for these channel height definitions. The variables are denoted by $()_\perp$ and $()_{\text{tip}}$, respectively, such that δ_{tip} corresponds to the smallest reference channel height among all discussed choices, whereas $\delta_\perp$ lies between δ and δ_{tip}.

In agreement with the observations with respect to [panels (a) and (b)] of figure 5.7, a smaller reference channel height leads to a larger relative change of C_f. This is particularly true for larger surface structures , while smaller ones (such as dr_1a and dr_1b, for which $h/\delta \ll 1$) hardly reveal any difference. In both representations [shown in panels (c) and (d)] of figure 5.7, the set dr_1c achieves a relative change of C_f comparable to or larger (in absolute value) than sets dr_1a and dr_1b. This result is unexpected, given that the shape of these sets is geometrically similar, but dr_1c has rounded riblet tips, which is known in the literature to be associated with reduced riblet performance [114].

It can be seen that also the zero crossing for ΔC_f is influenced by the channel height definition. Very good collapse of all data sets at this location is obtained for both channel height definitions in [panel (c) and (d) of] figure 5.7 albeit at different values of l_g^+.

Overall, these different types of data evaluation indicate that the choice of reference channel height strongly influences the drag values obtained through pressure-drop evaluation of internal flow when large-scale separation between the surface structure or roughness size and the boundary layer thickness is not fulfilled. It is thus of utmost importance that the choice of the reference channel height is clearly reported for such cases. A posteriori translation of the results for other reference channel heights can then be carried out following equation (5.3)." [von Deyn et al., 2022a]

5.4.2 Drag Regimes of 2D Surface Structures

"As introduced with the schematic in figure 5.1, the data evaluation in terms of roughness function ΔU^+ allows to distinguish different drag regimes. Figure 5.8 shows ΔU^+ against l_g^+ for all investigated cases."[von Deyn et al., 2022a]. ΔU^+ is retrieved from C_f and C_{f0} (2.33) as outlined in §2.2.2. For the remainder of this chapter, all reported quantities are based on δ defined with $h_\parallel$. "The viscous scaled mean velocity profile retrieved from DNS data [(see §5.5.2)], which is available for the case di_13, hints at the applicably of the described framework also for large ridges." [von Deyn et al., 2022a]

Drag-Reducing Regime

"The viscous prediction introduced by [66] for the physically smallest riblet set dr_1a is also included in figure 5.8 and can be expressed as

$$\Delta U^+ = \frac{h_\parallel - h_\perp}{l_g} l_g^+ = -0.14\, l_g^+ \tag{5.4}$$

for the viscous regime [35]. The measurement results show excellent agreement with this viscous prediction between $1 < l_g^+ < 7$, thus confirming its applicability as previously demonstrated by [42]. As noted before, the smaller drag reduction achieved with the geometrically similar data set dr_1b is probably related to local imperfections of this riblet foil. For increasing l_g^+, ΔU^+ deviates from the predicted behaviour and the well-known breakdown of the viscous regime occurs, leading to an increase of ΔU^+ past the point of maximum drag reduction. In agreement with literature data, the drag-reducing regime extends up to $l_g^+ \approx 17$ where $\Delta U^+ = 0$ is found." [von Deyn et al., 2022a]

Fully-Rough Drag Regime

"For even larger l_g^+, the fully-rough drag regime follows. In this regime, the riblet surfaces, which cannot induce any pressure drag due to their streamwise invariant surface, reveal an apparent fully-rough behaviour (typically attributed to the dominance of pressure drag on roughness elements). The data sets dr_1b, dr_1c and dr_2 show a remarkably good agreement. In addition, data set di_2 - which is geometrically similar to dr_2 - also reaches into this region and partially overlaps with dr_2. We note that this collapse between riblets and ridges is only obtained for a data evaluation based on the half channel height δ [defined with $h_\parallel$]. The alternative channel height definitions discussed in section 5.4.1 [...] do not yield this collapse. For reference, the Colebrook roughness function [19] is also included in figure 5.8 which does not capture the observed trends, as it is also found for irregular roughness [16].

The good collapse of all experimental data indicates that the combination of l_g^+ and a channel half-height definition based on $h_\parallel$ are particularly well-suited for the description of the fully-rough drag regime, which extends up to $l_g^+ \approx 40$. Note that choosing s^+ or h^+ leads to worse agreement between data sets compared to l_g^+. The corresponding relation between ΔU^+ and l_g^+ corresponds to the one of classical fully-rough surface [85] with l_g^+ as the roughness length scale

$$\Delta U^+(l_g^+) = \frac{1}{\kappa} \ln l_g^+ + C. \tag{5.5}$$

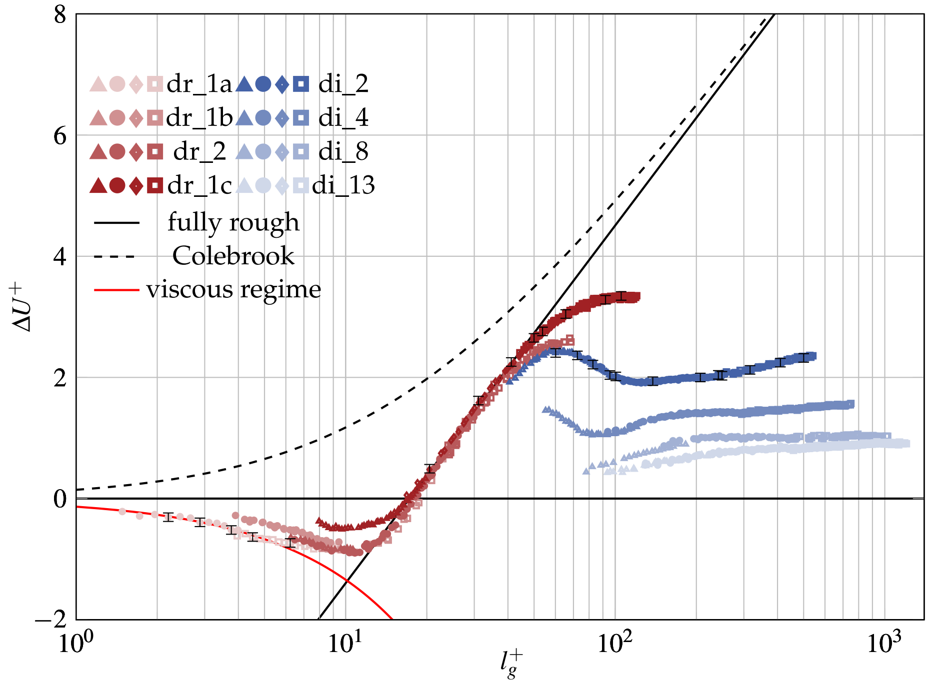

Figure 5.8: Roughness function ΔU^+ vs. l_g^+. The black solid line represents the fully-rough behaviour (see (5.5)) with $\kappa = 0.39$, $C = -7.3$. The red solid line represents the viscous friction prediction with $\Delta U^+ = \frac{h_\parallel - h_\perp}{l_g} l_g^+ = -0.14 l_g^+$ computed for set dr_1a. Additionally, the Colebrook roughness function is included for reference as the black dashed line [19]. The vertical error bars represent the measurement uncertainty for exemplary data points. The horizontal error bars are negligible in this representation. Figure adopted from [von Deyn et al., 2022a].

Employing a von Kármán constant of $\kappa = 0.39$ yields an additive constant of $C = -7.3$. A comparison with the corresponding relation for the Nikuradse sand grain roughness $\Delta U^+(k_s^+) = \frac{1}{\kappa} \ln k_s^+ - 3.5$ [16] results in an equivalent sand grain roughness of

$$k_s^+ = l_g^+ / 4.4 \tag{5.6}$$

for the investigated surface structures. The equivalent sand grain roughness of the identified fully-rough regime of riblets and ridges appears thus to be predictable based on the geometrical properties of the surface, in particular l_g and $h_\parallel$. This is a remarkable result since the identification of such links between surface topography and the hydraulic roughness scale k_s (and thus the related drag) is one of the key issues in roughness research due to large uncertainties in the existing predictive correlations [16]. In analogy to equation (5.4), equations (5.6) or (5.5) can thus be directly employed to predict the drag of 2D streamwise aligned trapezoidal grooved surface structures in a certain region of l_g^+, here $17 \lessapprox l_g^+ \lessapprox 40$." [von Deyn et al., 2022a]

Non-Monotonic Regime

"Beyond $l_g^+ \approx 40$, ΔU^+ exhibits a weaker increase with l_g^+ than in the preceding fully-rough drag regime. The present data sets confirm the deviation from the logarithmic increase of ΔU^+ around $l_g^+ \approx 40$ previously reported by [Gatti et al., 2020] (based on data set dr_2) for additional riblet (data set dr_1c) and ridge (data set di_2) structures.

ΔU^+ increases mildly for $200 < l_g^+ < 1000$. Before this mild increase is reached, data sets di_2 and di_4 reveal a particular behaviour, most striking for di_2, that is reported for the first time. Following the deviation from the fully-rough regime, ΔU^+ reaches a local maximum at $l_g^+ \approx 60$ before it decreases towards a local minimum at $l_g^+ \approx 100-200$. Set `di_4` also exhibits this non-monotonic behaviour in ΔU^+ with a local minimum around $l_g^+ \approx 85$.

Based on these observations, an additional regime can be introduced where ΔU^+ decreases unexpectedly and which we term the non-monotonic regime. This regime can only be identified in two of the present data sets and it remains to be investigated in future studies whether this non-monotonic behaviour of ΔU^+ featuring local maxima and minima is a universal feature of 2D longitudinally-aligned surface structures." [von Deyn et al., 2022a]

Hydraulic Channel Height Regime

"The observed mild increase of ΔU^+ for $200 < l_g^+ < 1000$ for the ridge cases corresponds to a Reynolds number range in which the data sets `di_2`$\cdots$`di_13` exhibit C_f-curves which seem retrievable by shifting the C_{f0} vs. Re_b curve upwards (see figure 5.6). In other words, the C_f-curves of the structured surfaces could be derived by multiplying the smooth reference by a constant factor. Such a procedure is comparable to the common definition of the hydraulic diameter $D_{\text{hyd}} = 4A/P$, where A corresponds to the duct cross-section and P to the wetted perimeter [97]. Pirozzoli [87] showed that this classic definition is not applicable for ducts with high aspect ratios and presented an alternative formulation for the hydraulic diameter. However, this formulation assumes a constant distribution of wall-shear stress across the span, which is a fair assumption for ducts whose cross-section varies mildly and regularly but clearly does not hold for the present trapezoidal groove surfaces.

In order to assess whether the present data can be described by a concept similar to a hydraulic diameter approach, we evaluate a *hydraulic channel half height* δ_{hyd} a posteriori for each surface structure and Re_b. If δ_{hyd} assumes a constant value independently of Re_b, the friction behaviour in this regime can be solely described by the ratio $\delta_{\text{hyd}}/\delta$ and the smooth-wall $C_{f0}(Re_b)$-correlation, in analogy with the well established hydraulic diameter concept for low-aspect-ratio ducts.

For each (C_f, Re_b)-pair measured for a considered 2D surface, we compute δ_{hyd} by answering the question “what would be the channel height of a smooth channel driven at the same flow rate that yielded the same skin-friction coefficient”. Therefore, δ_{hyd} is expressed based on the ratio C_{f0}/C_f through equation (3.2), such that

$$\delta_{\text{hyd}} = \delta \left(\frac{C_{f0}}{C_f} \right)^{\frac{1}{3}}. \tag{5.7}$$

In analogy to the definition of the smooth wall reference channel height δ (based on an identical $C_f(Re_b)$ correlation for smooth and structured walls under laminar flow conditions), δ_{hyd} represents the channel height of a smooth wall reference channel with the same friction coefficient under turbulent flow conditions. The ratio $\eta = \delta_{\text{hyd}}/\delta$ can thus be interpreted as a measure for the effective change in hydraulic channel height due to turbulence." [von Deyn et al., 2022a]

"Figure 5.9 shows η as a function of l_g^+. Riblets that yield $\Delta C_f/C_{f0} < 0$ (see figure 5.7) result in values of $\eta > 1$, while the opposite occurs for $l_g^+ > 17$ (where $\Delta C_f/C_{f0} > 0$), where turbulence is modified such that δ_{hyd} is smaller than δ ($\eta < 1$).

For high values of l_g^+, the ratio $\eta = \delta_{\text{hyd}}/\delta$ tends to a surface-specific constant value, which we denote as η_c. The corresponding values are included in table 5.1. The observed trend indicates that the friction behaviour of drag-increasing ridges can be described by a hydraulic reference channel height in the high Reynolds number regime (or high l_g^+ regime), which we term hydraulic channel height regime. Widely

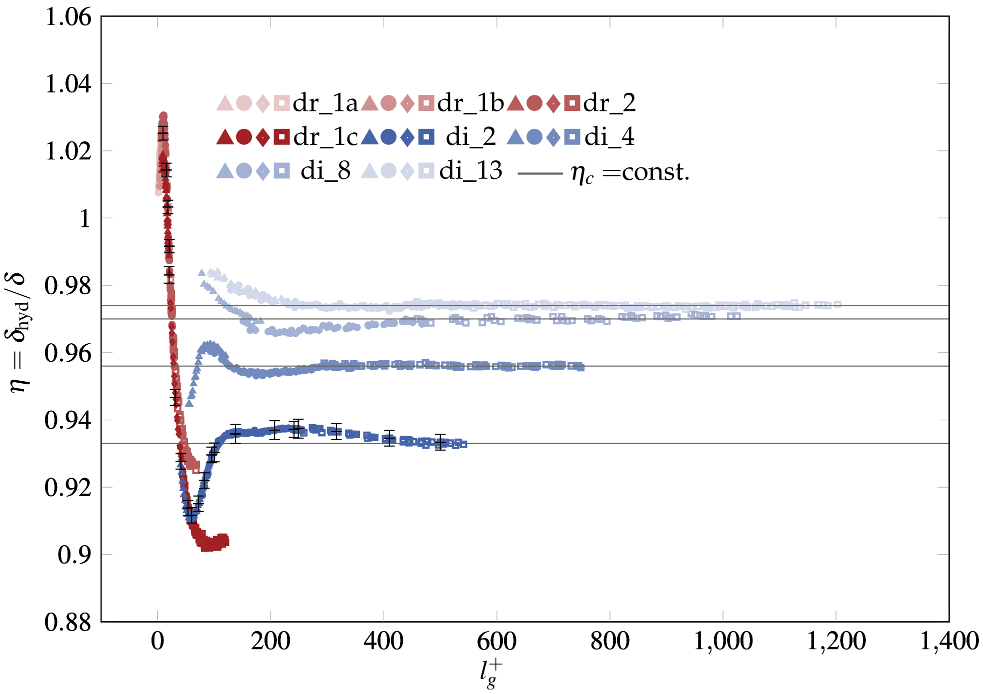

Figure 5.9: Hydraulic half channel height ratio $\eta = \delta_{\mathrm{hyd}}/\delta$ obtained from equation (5.7) vs. l_g^+. Grey lines indicate values for constant η, referred to as η_c. The corresponding values are included in table 5.1. The vertical error bars represent the measurement uncertainty for exemplary data points. The horizontal error bars are negligible in this representation. Figure adopted from [von Deyn et al., 2022a].

spaced ridges such as di_13 saturate to η_c at $l_g^+ \approx 300$, whereas the narrow-spaced ridges undergo a transient region and approach η_c at higher l_g^+: di_2 . . . di_8 at $l_g^+ \approx 500$. Given the discrepancy for the onset of the hydraulic channel height regime in terms of l_g^+, l_g^+ does not seem to be the suitable scaling to determine its onset. The existence of such scaling remains to be investigated in future studies. We note that the observed hydraulic channel height regime does not agree with a constant friction increase $\Delta C_f/C_0$ beyond the fully-rough drag regime postulated by [Gatti et al., 2020].

In order to obtain a complete predictive framework for the drag behaviour in the hydraulic channel height regime, an a priori definition of η_c would be required. The classical hydraulic diameter approach is built on the idea that geometrical parameters as the perimeter increase P/s determine the drag behaviour. Such parameters are considered in the following and figure 5.10 shows η_c as a function of different geometrical surface parameters, namely the relative increase of wetted surface area P/s, the square root of the groove area normalised by the tip distance l_g/s, and the reciprocal of the structure spacing normalised by the channel half height δ/s. The geometrical similarity of the surfaces for which we were able to achieve the hydraulic channel height regime does not allow the formulation of general predictive statements, albeit clear trends can be recognised." [von Deyn et al., 2022a]

"Figure 5.10 (a) reveals a nearly linearly decreasing η_c, and thus higher drag, with increasing P/s. For the limiting case of wide-spaced small ridges, for which the increase of wetted perimeter becomes negligibly small, P/s tends to one. One would thus expect to retrieve $\eta_c = 1$ at $P/s = 1$ which is approximately fulfilled with the observed trend in figure 5.10 (a).

Since l_g is a length scale commonly applied to capture and unify different riblet shapes, l_g/s can be understood as a measure of groove shape versus ridge spacing. The available four data points from the present study appear to follow a non linear decrease $\eta(l_g/s)$ in Figure 5.10 (b). The limit $\eta_c = 1$ is reached

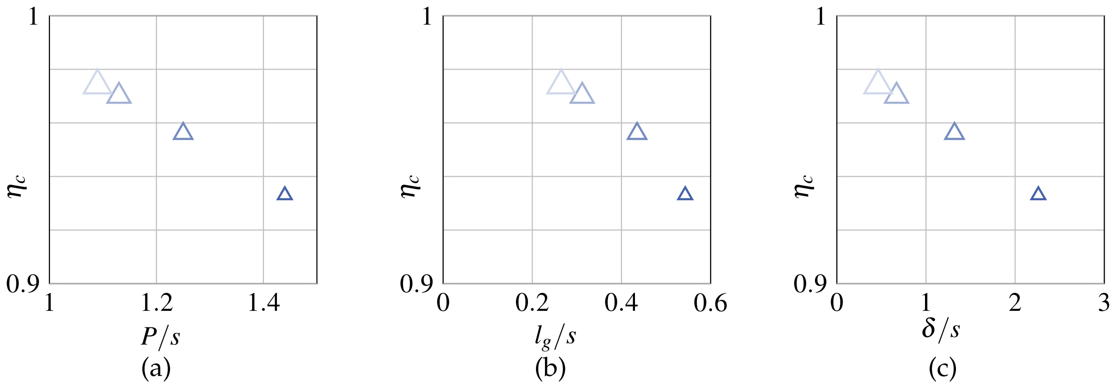

Figure 5.10: Constant hydraulic channel height ratio η_c obtained in the hydraulic channel height regime as a function of different geometrical surface properties. Larger markers indicate increasing s/δ with marker colours representing the individual data sets as introduced in figure 5.12. (a): perimeter increase P/s. (b): l_g/s. (c): reciprocal spanwise wavelength δ/s. Figure adopted from [von Deyn et al., 2022a].

in this representation for increasing s at fixed h, decreasing h at fixed s, or a combination of both. Again, this limiting data case is approximately retrieved by the observed data trend.

The constant hydraulic channel height ratio η_c as function of the reciprocal spanwise wavelength s/δ is plotted in figure 5.10 (c) such that the limiting case of a smooth wall ($\eta_c = 1$) is located at $\delta/s = 0$. In this representation, a linear trend is also observed, which agrees reasonably well with the limiting value for a smooth wall.

Overall, all investigated surface structure features seem equally suitable to obtain a predictive correlation for η_c. Additional ridge configurations of varying cross-sectional shapes need to be investigated in future studies in order to tackle a possible identification of a unified empirical or physics-informed predictive correlation for the hydraulic channel height ratio induced by ridges. This remaining challenge of an a priori definition for the hydraulic channel height ratio η can be compared to the “the bottleneck in our ability to make full-scale predictions of drag” [16] in roughness research by means of the equivalent sand grain roughness (which is also a hydraulic quantity) based on geometrical surface properties." [von Deyn et al., 2022a]

Hydraulic Channel Height Difference

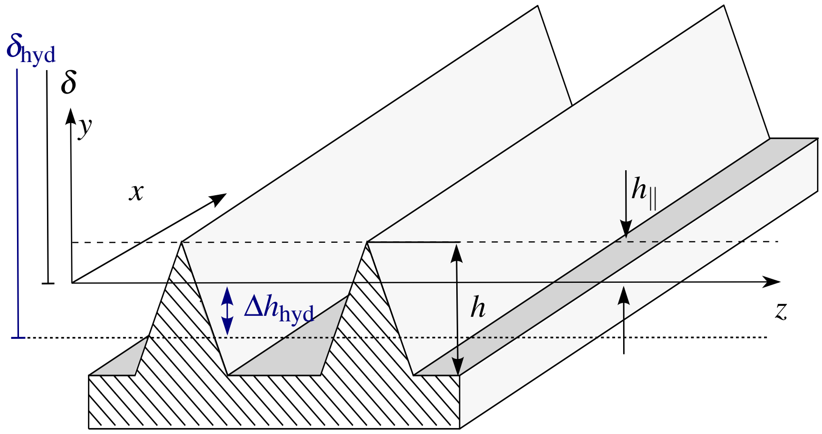

.

Figure 5.11: Sketch to illustrate the definition of the hydraulic channel height difference $\Delta h_{\text{hyd}} = \delta_{\text{hyd}} - \delta$. Note that Δh_{hyd} can assume positive and negative values depending on the drag regime. Figure adopted from [von Deyn et al., 2022a].

"To further assess the change of the hydraulic channel height induced by different surface structures in the drag decreasing and drag increasing regime, we introduce the hydraulic channel height difference defined as

$$\Delta h_{\mathrm{hyd}} = \delta_{\mathrm{hyd}} - \delta \qquad (5.8)$$

which is visualized in figure 5.11. Δh_{hyd} assumes positive values if $\eta > 1$ and is otherwise negative, thus offering an alternative way to visualise changes in C_f.

Figure 5.12 shows Δh_{hyd} normalized by the structure height h as a function of Re_b for all investigated surface structures. In this normalisation, all physically large ridge structures show small negative values indicating that the reduction of the effective channel height for turbulent flow conditions is larger than $h_{\|}$, i.e. larger than the one which would occur in a laminar flow, but still much smaller than the maximum height of the structures. In contrast, the physically smaller riblet surface structures result in values $\Delta h_{\mathrm{hyd}}/h$ that in modulo can be significantly larger than one. This indicates an interesting property of riblets: the origin for δ_{hyd} can be located below the riblet valleys in the drag-reducing regime and above the riblet tips in the drag-increasing regime.

In figure 5.12, constant values of $\Delta h_{\mathrm{hyd}}/h$ indicate the presence of the hydraulic channel height regime discussed above. In this plot versus Re_b, it appears as if this regime is also reached for the physically largest riblet case `dr_1c`. However, the result visualisation in figure 5.8 suggests that this might still be a transient behaviour. Therefore, this surface structure is not considered to have reached the hydraulic channel height regime within the Re_b-range of our experimental facility. In fact, we expect a decrease of $\Delta h_{\mathrm{hyd}}/h$ for `dr_1c` beyond the fully-rough regime, resulting in values more similar to the ones observed for ridges." [von Deyn et al., 2022a]

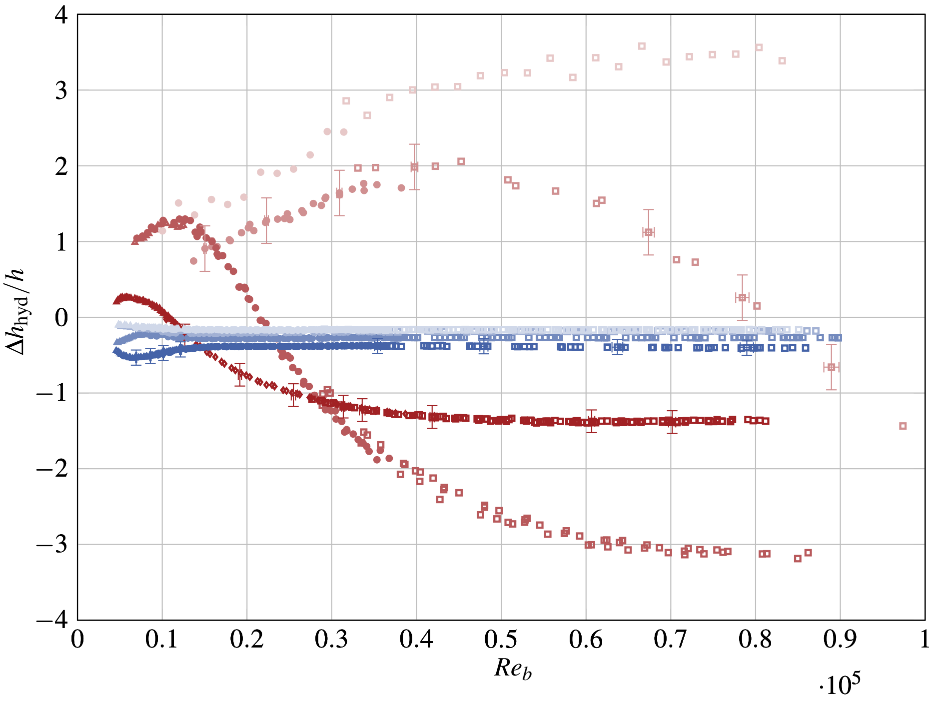

Figure 5.12: Hydraulic channel height difference Δh_{hyd} defined in analogy to the protrusion height (see sketch in figure 5.11 for definitions) normalized with the structure height h as a function of Re_b. Same markers as in figure 5.9. The horizontal and vertical error bars represent the measurement uncertainty for exemplary data points. Figure adopted from [von Deyn et al., 2022a].

5.5 Cross-Plane Velocity Measurements

In order to gain insight in the local flow phenomena that lead to the above described global skin friction and to further link with literature studies, sPIV measurements of riblet sets `dr_2` and `dr_1c` are discussed in §5.5.1. Moreover, concerted sPIV and single hot-wire measurements together with DNS results of the largest ridge geometry `di_13` are shown in §5.5.2.

5.5.1 Trapezoidal Groove Riblets

As mentioned in §5.1, different mechanisms are proposed that are related to the breakdown of the drag-reducing regime of riblets and the shift to the fully-rough regime (§5.4.2). While some studies attribute the breakdown of the drag-reducing regime to KH-instabilities [24, 36], the occurrence of secondary motions also contributes to the increase of ΔU^+, as shown by Modesti et al. [72].

Utilizing the sPIV setup described in §3.2, the 3D velocity statistics are measured in the $y-z$ cross-plane for the largest of the four riblet geometries `dr_2` and `dr_1c`]. The resulting "spanwise- wall-normal contours of the wall-normal velocity component V [...] are shown in figure 5.13, [...] normalised with the centerline velocity U_{Cl}. On the left side of figure 5.13, the results for [`dr_2`] (the physically smaller riblets) are shown. Re_b increases from top to bottom. For riblet set [`dr_2`], where all measurements are conducted in or close to the drag-reducing regime (in terms of Re_b), no vertical velocity in the riblet's near region can be detected. A different picture arises in case of the [`dr_1c`] riblet set: With increasing Re_b, an increasing V/U_{Cl} magnitude in the riblet vicinity is detected: Above the riblet's tip, fluid is moved upwards, while in the valley fluid pushed downwards. This observation indicates the emergence of secondary motions as the riblet's drag penalty increases.

It is worth noting that the small physical size of the riblets poses a significant challenge for the measurement equipment. The visible time-averaged contour levels at some distance from the wall stem from nonphysical artefacts in the processing. Due to the very small intensity of the secondary flow ($V/U_{Cl} \approx 0.2\%$), the mean streamwise particle displacement is three orders of magnitude larger than the in-plane motion. [As discussed in §3.2, the typical uncertainty of V is $\Delta V/U_{Cl} = 1\,\%$ and as such larger than the measured vertical velocity]. Thus, experimental detection of such secondary flows is hard to achieve. Nevertheless, the presented results show clear [indication] of the presence of secondary flows in the riblets' vicinity in agreement with the numerical findings of [72]. "[von Deyn et al., 2021b]

5.5.2 Wide Spaced Trapezoidal Groove Ridges

For the physically largest 2D surface structure set `di_13`, velocity measurements are conducted in the cross-plane, which is sketched in figure 5.14 with respect to the triangular ridges. From the literature, it is expected that set `di_13` induces domain-filling secondary motions, which are experimentally investigated with sPIV and hot-wire measurements. For a description of the experimental set-up see §3.2 and §3.1.2, respectively. As further validation of the experimental set-up, concerted DNS of `di_13` is carried out, which is also shown in appendix A.

Numerical Procedure

In order to match the experiment, "DNS of a fully developed turbulent channel flow in a smooth and structured configuration replicating [set `di_13`] are carried out under constant flow-rate conditions[1]. The

---

[1] The underlying surface distribution utilised for the DNS was provided by the author. The numerical simulation was set up and carried out by A. Stroh, identical to the procedure used in [104]. The data analysis was done by the author.

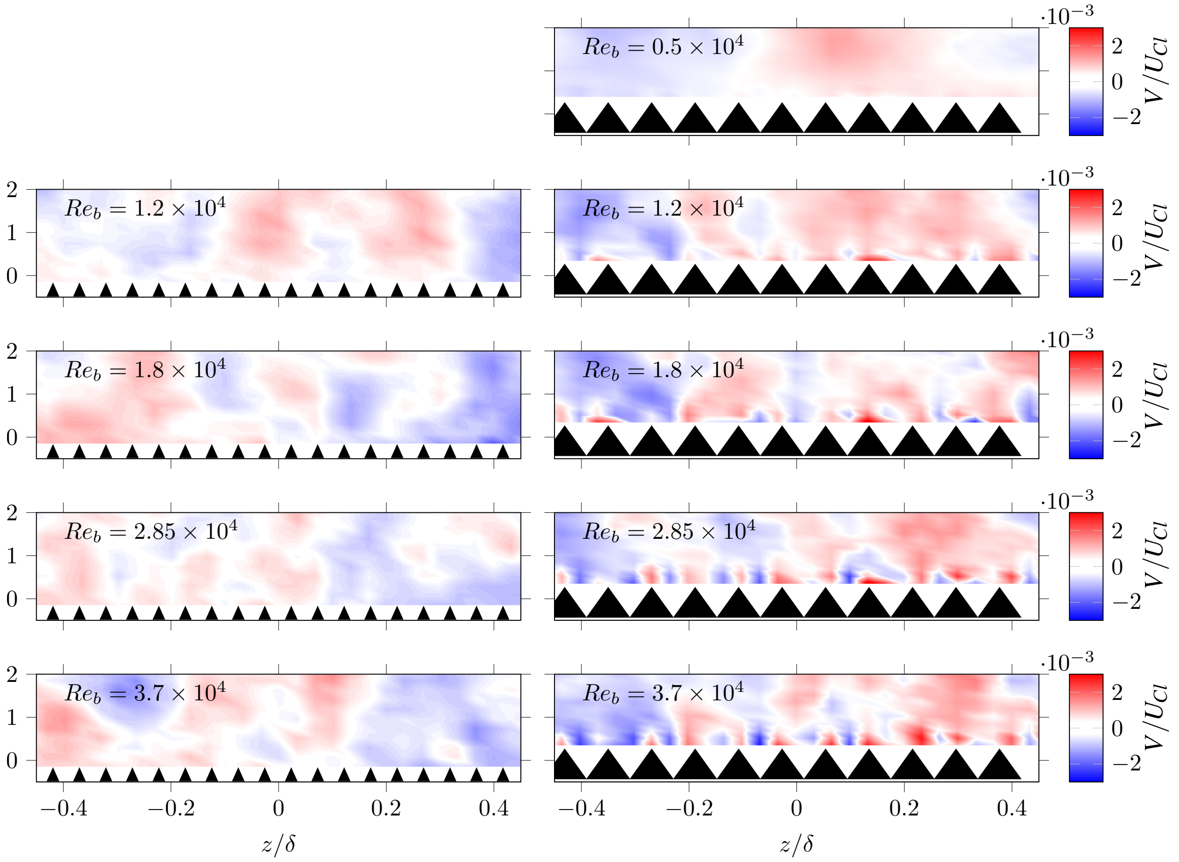

Figure 5.13: sPIV measurements of V/U_{Cl} contours for riblet sets dr_2 (left) and dr_1c (right) at various Reynolds numbers. Note that time averaged velocity contours V/U_{Cl} are shown. The measured velocity in the bulk region is not physical and stems from limitations in the spatial resolution of the employed sPIV set-up. Figure adopted from [von Deyn et al., 2021b].

ID	Re_b	Re_τ	$L_x \times L_y \times L_z$	Δx^+	Δy^+_{min}	Δy^+_{max}	Δz^+
refdns	1.8×10^4	496	$8\delta \times 2\delta \times 4\delta$	5.16	0.017	4.05	5.16
tridns	1.8×10^4	525	$8\delta \times 2\delta \times 4.32\delta$	5.66	0.018	4.44	6.16

Table 5.2: Simulation domain properties. Table adopted from [von Deyn et al., 2022b].

code implementation is based on the pseudo-spectral solver with Fourier expansions in the streamwise (x) and spanwise (z) directions and Chebyshev polynomials in the wall-normal direction (y) [15]. Periodic boundary conditions are employed in streamwise and spanwise directions such that, in contrast to the experiment, the DNS set-up does not contain any side walls. The required surface structuring is implemented with an immersed boundary method (IBM) according to [40]. The method imposes zero velocity in the solid region of the numerical domain utilising a volume force distribution F_i, which is added to the Navier-Stokes equations (2.2) at every time instant of the simulation. This IBM implementation was validated for rough surfaces by [33] and has been successfully used in previous works on secondary motions generated through longitudinal ribs [11, 104].

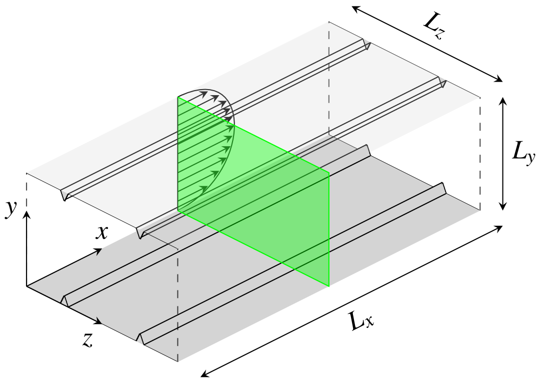

Figure 5.14: Schematic of investigated channel-flow configuration including ridge geometry. L_x, L_y, L_z denote the DNS simulation domain dimensions (table 5.2). The green plane indicates the laser-light sheet for the sPIV measurements.Figure adopted from [von Deyn et al., 2022b].

Details about the simulation domain and resolution for the present cases are presented in table 5.2. [...] A fixed resolution of $N_x \times N_y \times N_z = 768 \times 385 \times 384$ grid points was used. The spanwise simulation domain extent is adjusted to accommodate an integer amount of structure wavelengths s/δ in the computational box. Temporal and spatial averaging in the streamwise direction is applied to the DNS results since the secondary motion is observed in the cross-sectional plane perpendicular to the main flow direction. The transient of the simulation was excluded from time averaging, leaving at least 100 flow-through times for temporal averaging. The bulk Reynolds number Re_b for the comparison of hot-wire and sPIV results to numerical data is set to $Re_b = 1.8 \times 10^4$, which corresponds to a friction Reynolds number of $Re_\tau \approx 540$ in the smooth-wall case." [von Deyn et al., 2022b]

Secondary Motions Induced by Ridges

"The measured and simulated magnitudes $\sqrt{V^2+W^2}/U_{Cl}$ in the proximity of the triangular ridges [of set di_13] are compared in figure 5.15, where the sPIV has been recorded at the spanwise channel centre. $\sqrt{V^2+W^2}$ is normalized with the *global* centerline velocity U_{Cl}, derived from the spanwise averaged velocity profile. In the ridge vicinity, a significant secondary motion magnitude up to 4.5% is evident, caused by a domain-filling counter-rotating vortex pair (black vectors in figure 5.15).

In the $\delta \times \delta$ sized field of view of the sPIV experiment, very good agreement with the DNS results is found, indicating that the spanwise periodicity of the DNS does not induce any significant differences in the generated secondary flow compared to the duct flow of aspect ratio 1:12 in the experiment." [von Deyn et al., 2022b] Side wall effects and comparison to plane channel flow are further discussed in §4.2 and §4.3.

All obtained averaged velocities U, V, W and the respective Reynolds stresses recorded with sPIV at $Re_b = 1.8 \times 10^4$ are shown in figures 5.16 and 5.17, respectively. The domain-filling effect of the secondary motions becomes apparent in view of the U-contours presented in figure 5.16 (a): The vertical and spanwise velocity deflect fluid from the ridge vicinity, such that an up-welling motion over the ridge tip and a down-welling motion in the valley occurs that strongly bulges the mean streamwise velocity contours.

Also in the Reynolds stresses, the footprint of the secondary motions becomes apparent, as can be seen in figure 5.17. Above the structure's tip, strong fluctuations are induced that become domain filling. Especially the wall-normal spanwise fluctuations are particularly interesting as they highlight how the flow is deflected in the structure's vicinity and therefore mark the sense of rotation [105]. Note that the

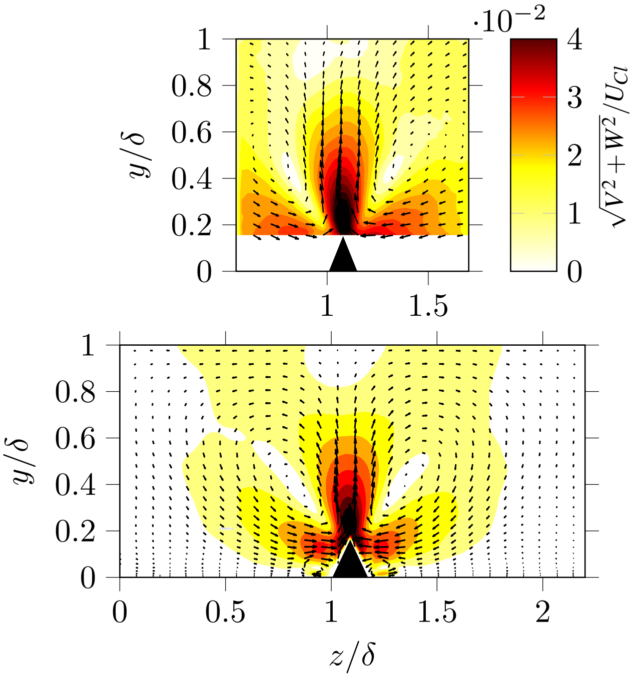

Figure 5.15: Secondary motion magnitude $\sqrt{V^2+W^2}/U_{Cl}$ contours for sPIV (top) and DNS (bottom) at $Re_b = 1.8 \times 10^4$. The direction of the secondary motion is represented by arrows. Figure adopted from [von Deyn et al., 2022b].

sPIV measurements shown in figures 5.16 and 5.17 are compared against DNS in appendix A, where good agreement between experiments and DNS is confirmed.

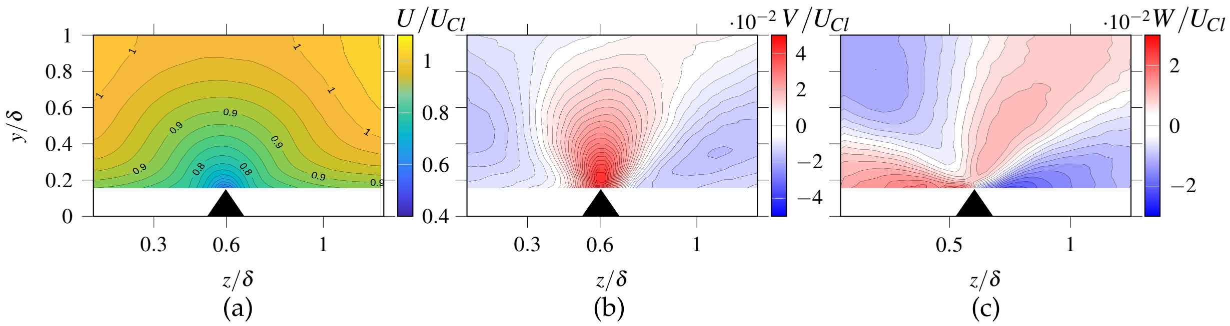

(a)

(b)

(c)

Figure 5.16: sPIV measurements of the mean velocity components for set di_13 at $Re_b = 1.8 \times 10^4$. Panel (a): U/U_{Cl}, panel (b): V/U_{Cl}, panel (c): W/U_{Cl} .

The bulging effect induced by the secondary flow is further highlighted in figure 5.18, where iso-lines of U obtained by hot-wire measurements and DNS are presented.

"The wall distance of the first hot-wire measurement point is not known a priori [81]. Thus, from the 2D hot-wire measurement grid, the mid-valley velocity profile between two ridges is fitted against a law of the wall proposed by Luchini [65]. In doing so, u_τ and the wall distance of the first measurement point y_0 closest to the wall is determined (only y_0 is used in the following since the velocity profiles are shown in outer scaling).

[...] Note that only a weak Reynolds number dependence of the bulging effect can be observed, which is consistent with previous studies [111]. For increasing Re_b, the iso-lines tend to be slightly closer to the

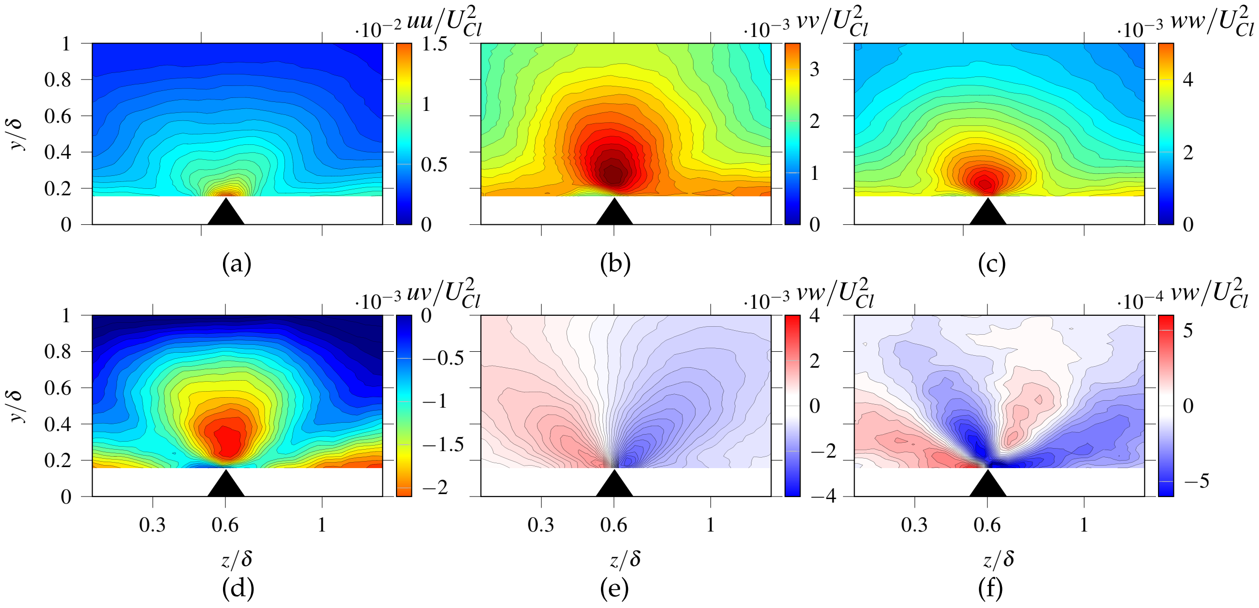

Figure 5.17: sPIV measurements of the Reynolds stresses for set di_13 at $Re_b = 1.8 \times 10^4$. Panel (a): uu/U_{Cl}^2, panel (b): vv/U_{Cl}^2, panel (c): ww/U_{Cl}^2, panel (d): uv/U_{Cl}^2, panel (e): uw/U_{Cl}^2, panel (f): vw/U_{Cl}^2.

wall in the ridge valley. However, overall the results in figure 5.18 indicate a robust behaviour of the secondary motion, largely independent of Re_b." [von Deyn et al., 2022b]

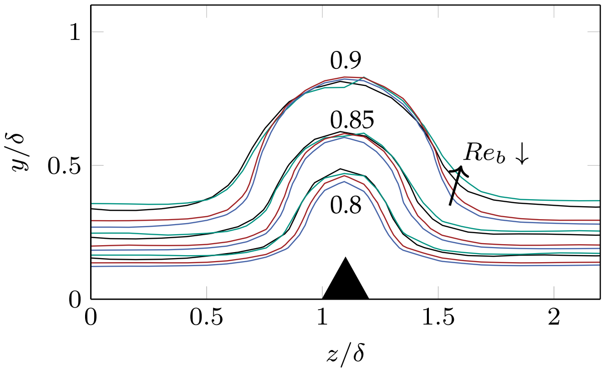

Figure 5.18: Contours of mean streamwise velocity U/U_{Cl} for set di_13. Green (hot-wire): $Re_b = 1.2 \times 10^4$. Black (DNS): $Re_b = 1.8 \times 10^4$. Red (hot-wire): $Re_b = 3.7 \times 10^4$. Blue (hot-wire): $Re_b = 5.8 \times 10^4$. Figure adopted from [von Deyn et al., 2022b].

Outer-layer Similarity

As discussed in §2.2.2, outer-layer similarity is required in the sense that the smooth and structured viscous scale spanwise averaged velocity profile U^+ can be approximated with a logarithmic law of the wall with the same von Kármán constant κ for the utilised procedure to compute ΔU^+ as shown in §5.4. The viscous-scaled spanwise-averaged mean velocity profile of the case di_13 obtained via DNS with respect to a smooth reference is shown in figure 5.19. It can be seen that both the smooth and di_13 velocity profile do agree with the logarithmic law of the wall beyond $y^+ > 30$ when placing the wall-normal origin $h_\|$ below the ridge tip, thus showing a slope of $1/\kappa$ in figure 5.19. Therefore, the assumptions described in §2.2.2 (where the computation of ΔU^+ as a function of C_f is introduced) are also applicable

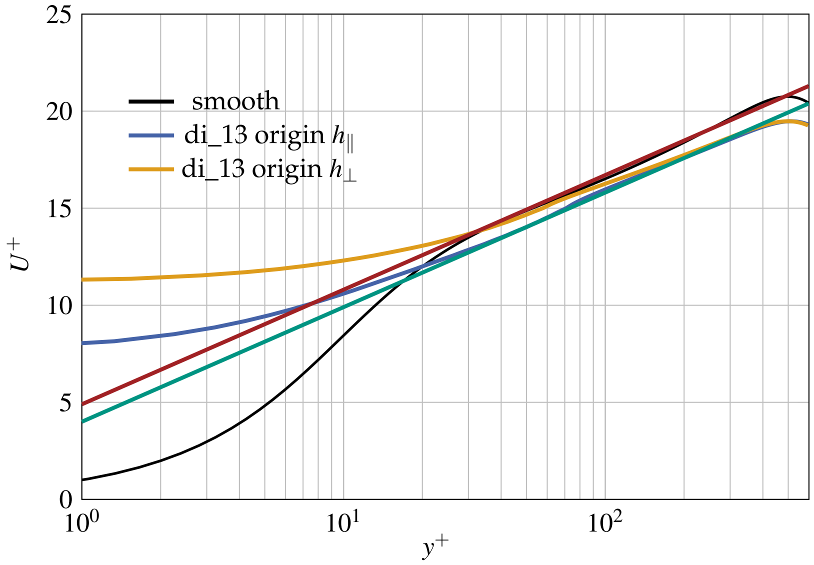

Figure 5.19: Viscous scaled spanwise averaged mean velocity profile of case di_13 in comparison to the smooth profile at matched $Re_b = 18000$. The blue and yellow lines represent the same DNS case, but different wall-normal origins are used. The red and green lines represent $1/\kappa$ slope with $\kappa = 0.39$.

for the largest ridge cases. Note that also the shift $\Delta U^+ \approx 0.9$ between the red (smooth) and green (ridge) line representing a slope of $1/\kappa$ matches reasonably well with the value of ΔU^+ reported in figure 5.8.

As an additional choice, $U^+(y^+)$ is shown when the origin is placed $h_\perp$ below the structure's crest. Judging from the DNS case presented in figure 5.19, placing the origin at $h_\perp$ below the tip seems less favourable for the particular ridge case di_13 shown as the yellow line. The slope of $1/\kappa$ is also apparent, but the match with the logarithmic law of the wall is shifted to significantly higher y^+.

The detected logarithmic behaviour of the ridge case agrees with the study of Castro et al. [11] on streamwise aligned rectangular ridges of various spanwise spacing, who state that "a log-law-like region in the spanwise-averaged axial mean velocity profiles [is apparent], even though local profiles may be very different." [11].

6 Drag of Spanwise Heterogeneous Roughness

Building on the insights gained from the study on streamwise aligned 2D surface topographies (riblets and ridges) presented in chapter 5, spanwise alternating smooth and rough strips are investigated in this chapter. As shown in the preceding chapter, the definition of the half channel height is of particular importance and it is favourable to use a definition based on a laminar reference. It is relatively easy to define the laminar reference for streamwise aligned structures by solving a Stokes flow problem (see §5.3). However, this is not the case for roughness elements, as the investigated sandpaper roughness is random and Stokes and laminar flow do not coincide for three-dimensional roughness. Therefore, DNS is used in conjunction with the experimental methodology in order to define a laminar reference case and to gain insight into turbulent statistics that cannot be resolved with the current experimental set-up. Furthermore, it is investigated if similar or different drag regimes can be distinguished with respect to the drag regimes discussed for riblets and ridges (see §5.4.2).

6.1 Strip-Type and Ridge-Type Roughness

In order to limit the parametric space and specifically investigate lateral heterogeneous surface effects, two simplified configurations of spanwise inhomogeneous roughness are often studied in literature termed strip-type and ridge-type roughness.

In case of ridge-type roughness, local details are neglected and exceedingly rough patches compared to the remaining surface distribution are simplified to smooth protruding ridges aligned in streamwise direction on a smooth wall. This abstraction has the clear advantage of an easily manufacturable well-defined surface distribution, where parametric studies can be carried out. Making use of this set-up, [110] reported strong secondary motions with an upwelling motion over the protruding ridges that is strongest when placing the ridges at a spanwise wavelength s in the order of the characteristic length scale δ of the flow. Moreover, [69] pointed out that the individual ridge shape needs to be accounted for to adequately capture the secondary motion and its impact on skin-friction drag.

Alternatively, when the boundary-layer thickness or half-channel height δ is much larger than the characteristic scale of the roughness height, the roughness elevation is often assumed to be negligible. In this case, spanwise inhomogeneous roughness may be approximated as strip-type roughness. This simplification can be exploited in numerical simulations in which a spanwise alternating wall-shear stress is prescribed on a geometrically smooth wall [3, 18]. The strip-type roughness produces a down-welling motion over the region of higher wall-shear stress [48]. Chung et al. [18] found the secondary flow to be domain filling between $0.39 \leq s/\delta \leq 6.28$.

As a further step towards more realistic inhomogeneous roughness, alternating smooth and protruding sandpaper strips, as depicted in figure 6.1 (a), are investigated in this chapter. Thus, the protruding roughness strips experience additional form drag, which is not present in studies featuring smooth ridges such as [68, 69, 120]. Furthermore, skin-friction measurements of smooth ridges of the same width and averaged height as the protruding sandpaper strips as depicted in 6.1 (b) are carried out. This allows to quantify the differences in global friction of protruding roughness strips and smooth ridges and links the present study to the available literature. Finally, sandpaper strips submerged between smooth strips, resembling strip-type roughness as depicted in figure 6.1 (c), are investigated. The smooth and sandpaper strips are equally spaced of width $w_{\mathrm{strip}} \approx \delta$ or $w_{\mathrm{strip}} \approx 2\delta$ resulting in a spanwise wavelength $s \approx 2\delta$ or $s \approx 4\delta$. In this regime, the chosen surface configurations are expected to generate secondary motions of Prandtl's second kind, as the stereoscopic particle image velocimetry measurements of [116] in a similar strip-type sandpaper configuration demonstrate.

It is of particular interest how the lateral inhomogeneity impacts the roughness function ΔU^{+}. As shown in chapter 5, a departure from the fully-rough behaviour for sufficiently large Reynolds numbers for riblets in the rough regime is found. Also, Medjnoun et al. [69] hypothesised the absence of fully-rough behaviour for 2D surface structuring based on their oil film interferometry measurements. Clearly, the investigated sandpaper strips experience form- and viscous drag impacting the overall drag. Therefore, the question arises whether a fully-rough flow state is reached for lateral inhomogenous roughness strips and how the expected presence of secondary flows impacts the global friction.

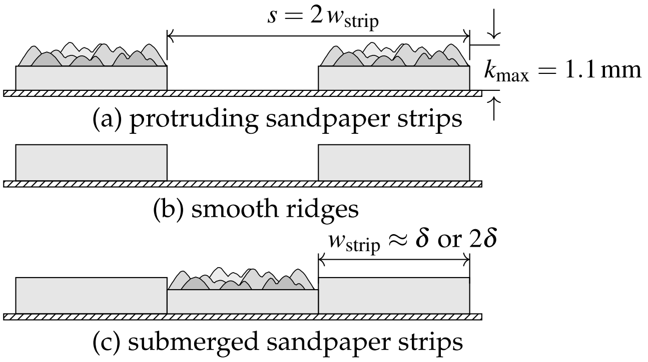

Figure 6.1: Schematic representation of the investigated types of lateral inhomogeneous surface configurations. Commonly, configurations (a) and (b) are referred to as ridge-type roughness and configuration (c) as strip-type roughness.

6.2 Overview of Investigated Roughness Configurations

Measurements are carried out in the three different configurations depicted in figure 6.1. Streamwise aligned spanwise alternating strips of smooth aluminium and P-60 grit sandpaper at two different spanwise wavelengths $s/\delta \approx 2$ and $s/\delta \approx 4$ are investigated. The protruding sandpaper roughness configuration denoted protruding_rgh_xδ, where x represents the approximated wave length s/δ, was manufactured by glueing sandpaper strips on a smooth aluminium plate, resulting in spanwise alternating smooth and protruding sandpaper strips. Thus, the domain-averaged roughness height is $h_{\mathrm{avg}} > 0$ (see sketch below table 6.1 for definitions).

Additionally, notches of the averaged sandpaper height's depth were milled in aluminium plates with a high-precision milling machine. This configuration was measured in the wind tunnel in order to quantify the effect of smooth protruding ridges (termed ridge_xδ in table 6.1) on friction drag without sandpaper roughness. Afterwards, sandpaper strips were glued in the notches, creating submerged roughness strips with $h_{\mathrm{avg}} = k_{\mathrm{avg}}$ of the homogeneous rough reference case. Thus, this configuration is named submerged_rgh_xδ.

The roughness properties of the surface distribution used as an input for DNS replicating the utilised sandpaper are specified in table 6.2. Optical measurements (Sensofar S neox) did not yield reliable roughness properties as the utilised sandpaper is highly reflective, making optical white light interferometry scanning challenging. Instead, tactile measurements (perthometer Mahr MarSurf PCV) and three-dimensional reconstruction of highly resolved photographs using photogrammetry [44] were used to obtain the statistical properties of the investigated sandpaper as stated in table 6.2. The experimental matrix is completed with measurements of a smooth reference aluminium plate and homogeneous sandpaper.

Complementary DNS of turbulent flow at $Re_b = 1.8 \times 10^4$ is carried out in order do enable a deeper physical analysis of cases protruding_rgh_2δ and submerged_rgh_2δ including DNS of the smooth and homogeneous rough reference cases. In order to define a laminar reference as discussed in §6.4, DNS of laminar flow at $Re_{Cl} = 100$ is carried out for all protruding_rgh_xδ submerged_rgh_xδ cases additional to the homogeneous rough reference case.

ID	s [mm]	k_{avg} [mm]	h_{avg} [mm]	h_{lam} [mm]	$\frac{\delta}{\delta_{\mathrm{avg}}}$	$\frac{s}{\delta_{\mathrm{avg}}}$	$\frac{k_{\mathrm{avg}}}{\delta_{\mathrm{avg}}}$	$\frac{h_{\mathrm{avg}}}{\delta_{\mathrm{avg}}}$	$\frac{s}{w_{\mathrm{strip}}}$	$\frac{h_{\mathrm{lam}}}{k_s}$	HWA	DNS
		10^{-1}	10^{-1}	10^{-1}			10^{-2}	10^{-2}				
smooth	-	-	-	-	-	-	-	-	-	-	✓	✓
homogen_rgh	-	6.7	6.7	7.59	0.9925	-	5.5	5.5	-	1	✓	✓
protruding_rgh_2δ	25	6.7	3.35	4.23	0.9926	2.038	5.4	2.7	1	1.169	✓	✓
protruding_rgh_4δ	50	6.7	3.35	3.86	0.9956	4.076	5.4	2.7	1	1.388	✓	✗
ridge_2δ	25	6.7	3.35	3.87	0.9962	1.926	5.3	2.6	1	-	✗	✗
ridge_4δ	50	6.7	3.35	3.642	0.998	3.852	5.3	2.6	1	-	✗	✗
submerged_rgh_2δ	25	6.7	6.7	7.29	0.9966	1.976	5.4	5.4	1	2.139	✓	✓
submerged_rgh_4δ	50	6.7	6.7	7.13	0.9977	3.952	5.4	5.4	1	2.55	✓	✗

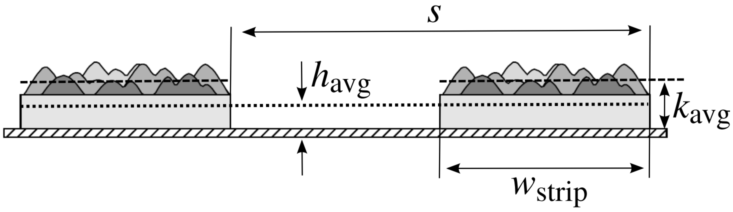

Table 6.1: Dimensions of the investigated sandpaper configurations. δ_{avg} denotes the average half-channel height defined with h_{avg}. δ is defined based on h_{lam}, see §6.4.

6.3 Numerical Procedure

Additional to the experimental pressure-drop, hot-wire and sPIV measurements, DNS of turbulent and laminar flow is carried out [1]. The utilised numerical method has been adopted in a number of numerical studies on roughness, e.g. [32, 105], where its general suitability for numerical roughness studies has been proven. The key challenge for the numerical simulations presented in this chapter is to prescribe matching surface boundary conditions with the experimental set-up.

A representation of the simulation domain is shown in figure 6.2, where the spatial domain size $L_x \times L_y \times L_z$ is noted. The DNS are carried out in plane channel flow, in which the flow is driven by a pressure gradient at constant flow rate. The roughness structures are installed on both the upper wall and lower wall.

---

[1] The numerical simulations were set up and run by J. Yang in close collaboration with the author. The data analysis was done by the author.

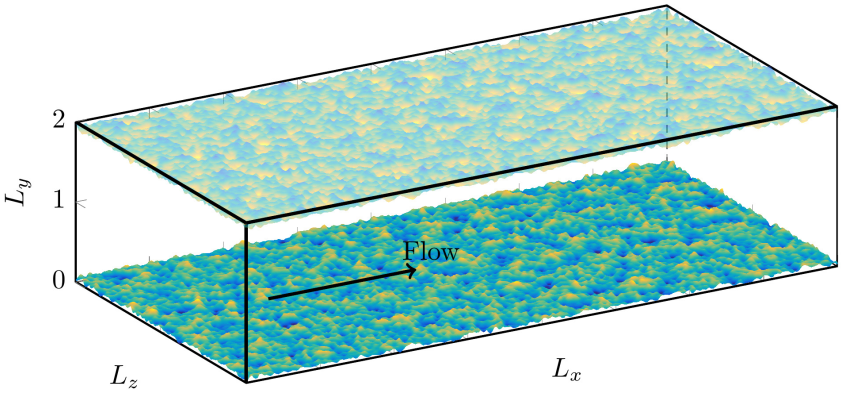

Figure 6.2: Schematic representation of the simulation domain with roughness mounted for the reference case homogen_rgh.

The incompressible Navier-Stokes equations are solved using the pseudo-spectral solver SIMSON [15], where the wall-parallel coordinates are discretised in Fourier space, while in wall-normal direction, Chevyshev discretisation is employed. An immersed Boundary Method (IBM) based on Goldstein's method [40] is used to impose the no-slip boundary condition on the roughness by introducing an external volume force field F_i directly to the Navier-Stokes equations (2.2). Periodic boundary conditions are applied in the streamwise and spanwise directions.

k_{avg}[mm]	k_{max}[mm]	k_{rms}[mm]	Sk	Ku	ES
0.68	1.1	0.674	0.6581	3.8010	0.6929

Table 6.2: Roughness properties of the surface distribution used as an input for the DNS replicating the utilised p60 sandpaper. The stated values are the mean roughness height k_{avg}, maximum roughness height k_{max}, root mean square k_{rms}, skewness Sk, kurtosis Ku and effective slope ES.

Different methods have been tried to generate the roughness distribution prescribed in the DNS. As a first test, an optical surface scan (Sensofar S neox) has been interpolated on the numerical grid, but the obtained C_f exceeded the experimental value by $\approx 20\%$. Tactile measurements (perthometer Mahr MarSurf PCV) and three-dimensional reconstruction of highly resolved photographs using photogrammetry [44] revealed that the highly reflective sand grains induce spurious data points in the surface scan such that the statistical properties of the sandpaper are not correctly resolved by white light interferometry.

For the presented simulations, a combination of the tactile measurements and photogrammetry scan has been used in order to make optimal use of the available data: the tactile measurements yield a highly resolved surface scan, but only in a 1D sense, while the photogrammetry scan resulted in converged 2D statistics, but the reconstruction algorithm smoothed small features.

ID	Re_b	$L_x \times L_y \times L_z$	Δx^+	Δy^+_{min}	Δy^+_{max}	Δz^+	C_f	Re_τ
smooth	1.8×10^4	$8\delta \times 2\delta \times 3.72\delta$	5.17	0.017	4.06	4.80	0.0061	496
homogen_rgh	1.8×10^4	$6.25\delta \times 2\delta \times 3.13\delta$	4.44	0.024	5.81	4.44	0.0122	703
protruding_rgh_2δ	1.8×10^4	$6.25\delta \times 2\delta \times 3.91\delta$	3.71	0.021	5.18	3.86	0.0098	629
sumberged_rgh_2δ	1.8×10^4	$5.97\delta \times 2\delta \times 3.73\delta$	3.47	0.021	5.14	3.62	0.0096	625

Table 6.3: DNS case overview of turbulent flow configurations.

The methodology to mathematically generate the roughness as boundary conditions in the DNS uses a random algorithm, in which the power spectrum (PS) and probability density function (PDF) of the surface height can be prescribed [84]. More details on this approach utilising the same numerical procedure are discussed in [118]. Consequently, the 1D-perthometer measurement can reflect the sandpaper's exact spatial structure. Therefore, the PS is expected to be accurate and used as an input to generate the roughness distribution. Accordingly, the photogrammetry measurement is employed due to its convenience in getting a converged PDF out of the 2D roughness distribution field to prescribe the PDF in the surface generation for the DNS simulation. This procedure also resulted in the best match with the pressure-drop measurements, as discussed in section §6.5. The resulting values of Re_τ and C_f are stated in table 6.3. The statistical properties of the sandpaper roughness surrogate prescribed in the DNS are specified in table 6.2.

Utilizing this setup, DNS of the configurations stated in table 6.3 of turbulent channel flow at $Re_b = 1.8 \times 10^4$ is carried out. The dimensions of the strip configurations are designed to match the experimental set-up. The spanwise domain size L_z is adjusted for the strip configurations such that two rough strips are contained in the simulation domain. The simulations are intended to match the experiments and provide further insights into the turbulent statistics since the cross-plane velocity statistics are difficult to resolve experimentally with the chosen set-up, as discussed in appendix A.

ID	Re_{Cl}	$L_x \times L_y \times L_z$	$N_x \times N_y \times N_z$
homogen_rgh	10	$6.25\delta \times 2\delta \times 3.13\delta$	$1000 \times 385 \times 500$
homogen_rgh	100	$6.25\delta \times 2\delta \times 3.13\delta$	$1000 \times 385 \times 500$
homogen_rgh	1000	$6.25\delta \times 2\delta \times 3.13\delta$	$1000 \times 385 \times 500$
protruding_rgh_2δ	100	$6.25\delta \times 2\delta \times 3.91\delta$	$1080 \times 385 \times 648$
protruding_rgh_4δ	100	$6.25\delta \times 2\delta \times 7.82\delta$	$1080 \times 385 \times 1296$
sumberged_rgh_2δ	100	$6.25\delta \times 2\delta \times 3.73\delta$	$1080 \times 385 \times 648$
sumberged_rgh_4δ	100	$6.25\delta \times 2\delta \times 7.46\delta$	$1080 \times 385 \times 1296$

Table 6.4: DNS case overview of the laminar simulations.

Additional to the turbulent simulations, DNS of all sandpaper configurations is carried out for laminar flow at $Re_{Cl} = 100$, as specified in table 6.4. These simulations are used to define a laminar channel half-height, as discussed in the next section §6.4. Also for the laminar cases, two roughness strips are accommodated in the simulation domain. Thus, for the wide strip configurations with $s \approx 4\delta$, the spanwise domain size L_z and grid points N_z are doubled, such that the resolution remains unchanged. In order to investigate potential Reynolds number effects, additional simulations at $Re_{Cl} = 10$ and $Re_{Cl} = 1000$ are carried out for the case homogen_rgh.

6.4 Definition of the Wall-Normal Origin

As discussed in §2.2, the choice of the wall-normal origin and consequently the half channel height δ directly impacts the reported C_f or ΔU^+ values. In chapter 5, it is shown that a well-suited choice of the wall-normal origin is based on a laminar solution for a given surface topography (see §5.3). For the 2D surface structures, the "channel height definition based on $h_\parallel$[...] provides a set-up in which the well-known $C_f - Re_b$-relation for laminar channel flow ($C_f = 12/Re_b$) also applies for a channel with riblets." [von Deyn et al., 2022a] Since laminar and Stokes flow aligned with the homogeneous surface direction coincide for 2D surface structures, an inexpensive Stokes flow problem is considered to obtain

$h_{\parallel}$. This is obviously not the case for three-dimensional rough surfaces and consequently, the Navier-Stokes equations are solved by means of DNS for laminar flow at $Re_{cl} = 100$ in order to define a laminar reference height h_{lam}. The numerical procedure is outlined above in §6.3 and all considered cases are listed in table 6.4.

The laminar reference height h_{lam} is defined in analogy to the streamwise protrusion height $h_{\parallel}$ for 2D structures (see §5.3). The definition of h_{lam} is schematically sketched in figure 6.3. h_{lam} denotes the distance of the laminar reference wall-normal origin from the reference smooth plane on which the roughness (strips) are mounted. For the presently investigated cases defined in table 6.1, $h_{\mathrm{lam}} > h_{\mathrm{avg}}$ holds true, while $h_{\mathrm{lam}} < k_{\mathrm{max}}$, i.e. the laminar reference wall-normal origin is always placed below the roughness crest.

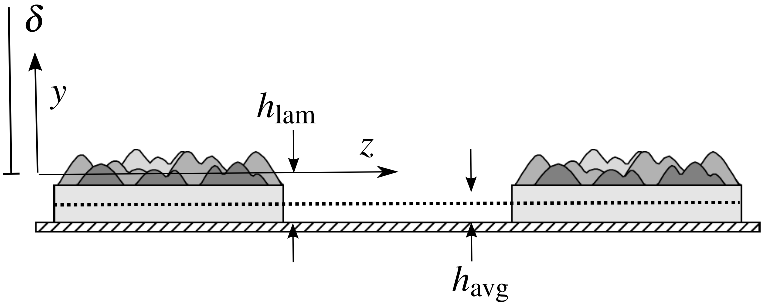

Figure 6.3: Sketch of protruding sandpaper strips to illustrate the definition of h_{lam}, which is used to define the effective channel half height δ.

As an exemplary case, the streamwise velocity contours U are shown for protruding_rgh_2δ in figure 6.4. A weak bulging above the rough strip is evident that propagates up to the channel centre. Note that the bulging and the orientation of the iso-lines changes substantially for turbulent flow as shown in §6.7.

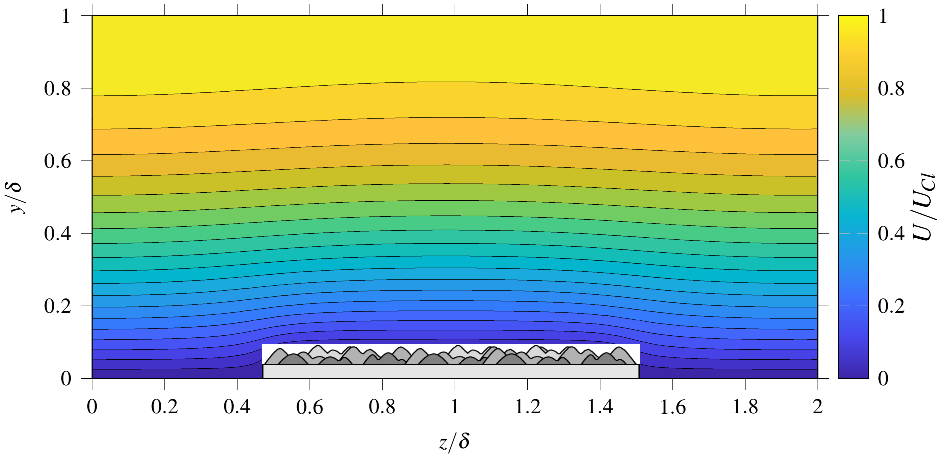

Figure 6.4: Laminar flow 2D streamwise velocity U contours obtained via DNS of protruding_rgh_2δ at $Re_{Cl} = 100$.

h_{lam} is obtained by fitting the spanwise averaged velocity profile U against a parabola, as shown in figure 6.5 for the case protruding_rgh_2δ. The green vertical line marks the maximum roughness height, and the $U(y/\delta)$ profile is fitted for $U/U_{Cl} > 0.05$, i.e. always above the roughness crest. The laminar wall-normal origin used to obtain h_{lam} is defined as the wall-normal position at which the parabola fit predicts zero velocity, highlighted as the yellow vertical line. This procedure is very similar to the one used to extract $h_{\parallel}$ as described in §5.3, except that for the roughness cases, Poiseuille flow is considered instead of shear (Couette) flow for practical reasons (the same numerical set-up was used for laminar and turbulent simulations, see 6.3).

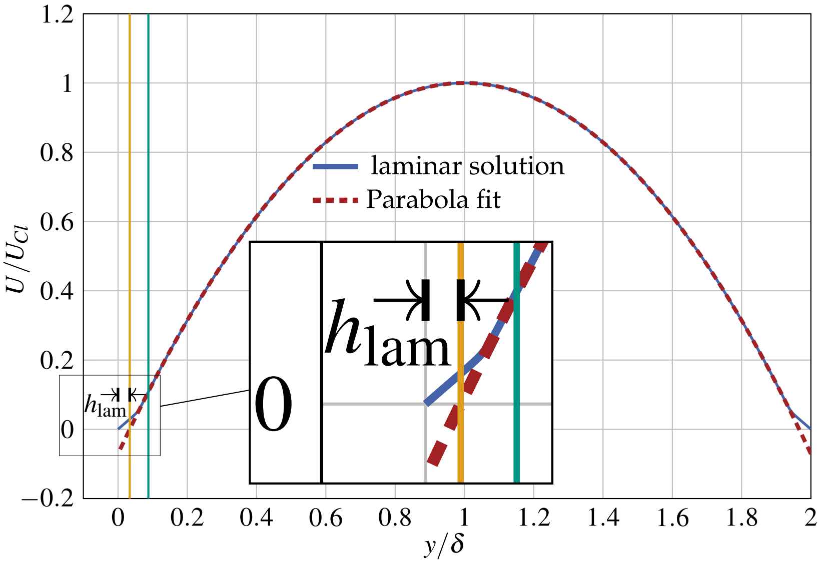

Figure 6.5: DNS solution for laminar flow at $Re_{Cl} = 100$ for the case protruding_rgh_2δ. The procedure to obtain h_{lam} is visualised based on the spanwise averaged velocity profile U shown as the blue line. The green vertical line indicates the maximum roughness height $k_{\max}$, while the yellow line marks h_{lam}.

It is important to note that the procedure to retrieve h_{lam} is analogous to the definition of $h_{\parallel}$ for 2D structures, but the physical interpretation is different: while channel flow subject to 2D structures fulfills $C_f = \frac{12}{Re_b}$ (see §5.3) when placing the wall-normal origin $h_{\parallel}$ below the structure's crest, this is not the case for roughness with the origin placed at h_{lam}. Due to the significant drag increasing effect of the investigated roughness topographies, fulfilling $C_f = \frac{12}{Re_b}$ would lead to negative values of h_{lam}, i.e. a laminar reference height that exceeds the maximum roughness height $k_{\max}$. Thus, the definition of h_{lam} assumes a different meaning compared to $h_{\parallel}$.

For all investigated cases, the obtained ratios of the laminar channel half height δ with respect to the geometrically spanwise averaged half channel height δ_{avg} are stated in table 6.1. Note that for the smooth ridge cases ridge_xδ the procedure described in §5.3 is applied since these geometries do not vary in streamwise direction. In the following, the effective half channel height δ defined with the laminar reference is used if not explicitly stated differently.

In view of the laminar flow considered, the centreline Reynolds number Re_{Cl} is varied over two orders of magnitude for the homogeneous rough reference case in order to assess potential Reynolds number influence on the definition of δ. The resulting ratios $\delta/\delta_{\text{avg}}$ are stated in table 6.5. It is observed that the evaluated δ slightly increases when increasing Re_{Cl} from 10 to 100, which can be attributed to an expected increasing relevance of inertial effects (wake drag) with increasing Reynolds number. Almost no difference is detected between the simulation at $Re_{Cl} = 100$ with respect to $Re_{Cl} = 1000$ in terms of $\delta/\delta_{\text{avg}}$.

Re_{cl}	10	100	1000
Re_b	13.3	133.3	1333.3
$\delta/\widetilde{\delta}_{\text{avg}}$	0.99449	0.99252	0.99259

Table 6.5: Reynolds number study of the ratio $\delta/\delta_{\text{avg}}$. DNS results obtained for the homogeneous rough reference case homogen_rgh.

6.5 Homogeneous Sandpaper Roughness

The skin-friction coefficient C_f of the smooth and homogeneous sandpaper reference cases are presented in figure 6.6 as a function of Re_b. The smooth results are shown as black markers with respect to the Dean correlation [23]. The different markers denote the varying orifice flow meter size employed to measure the volumetric flow rate (see table 3.1). Overall, the reference results show very good agreement with the Dean correlation with detected deviations below 2.7%, i.e. within the measurement uncertainty margin.

The measurements of the homogeneous rough reference consisting of p60 sandpaper with its roughness properties specified in table 6.2 are shown as the green markers in figure 6.6. For small Reynolds numbers, a gradual increase of C_f is evident, indicating a transitional rough behaviour. Above $Re_b > 3 \times 10^4$, C_f converges to a constant $C_f \approx 0.013$, indicating fully-rough behaviour. For reference, Nikuradse's original data [80] of his famous rough pipe experiments is included in figure 6.6. Note that Nikuradse used uniform-sized sand grains of size k_s to fabricate the rough pipes featured in his experiments. The presently investigated sandpaper is also made of sand grains but of varying sizes. Thus, in general the averaged height $k_{\mathrm{avg}} = h_{\mathrm{avg}} \neq k_s$. However, the ratio k_{avg}/k_s can be obtained by rescaling the roughness length scale to match the roughness function ΔU in the fully-rough regime with Nikuradse's data, as done in section 6.6.2 (see figure 6.11). In this framework, k_s is interpreted as the equivalent sand grain roughness size. The relative roughness size normalised with the respective characteristic length (half-channel height δ or pipe radius r) is denoted in figure 6.6 for the individual data sets.

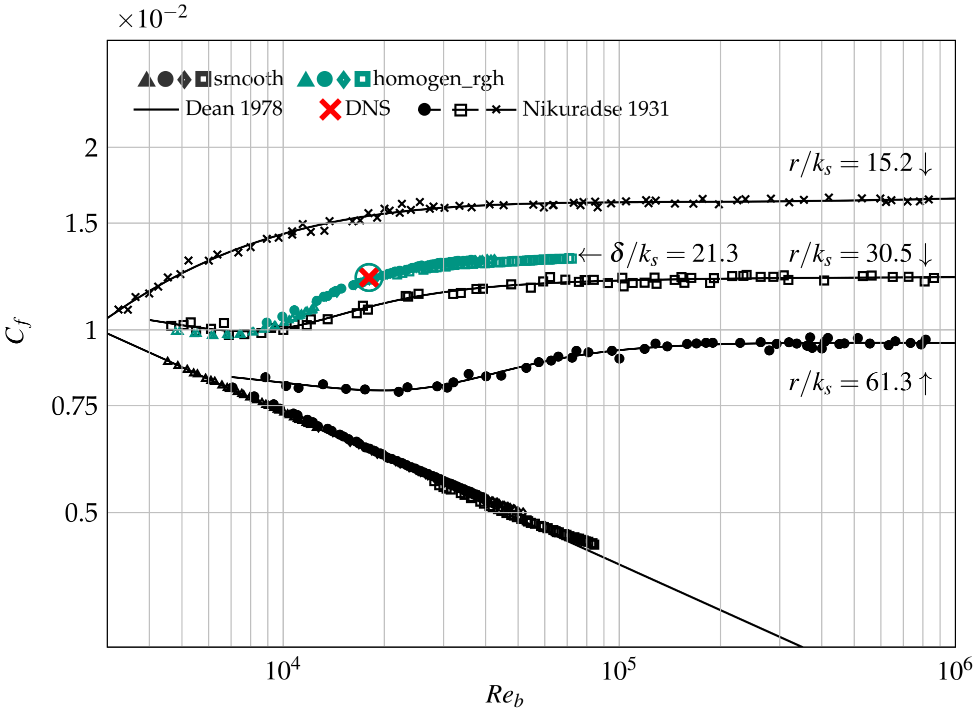

Figure 6.6: C_f vs. Re_b of smooth and homogeneous rough reference vs. experimental data of Nikuradse [80] and the correlation proposed by Dean [23] . k_s denotes the sand grain size in Nikuradse's experiments or the equivalent sand grain roughness in case of the current measurements. The ratio h_{lam}/k_s is obtained from figure 6.11.

Overall, the newly presented data set agrees very well with Nikuradse's measurements. For increasing r/k_s, i.e. smaller relative roughness size, the onset of the fully-rough regime is shifted towards higher Reynolds numbers. The homogeneous sandpaper data set with $\delta_{\mathrm{avg}}/k_s = 21.3$ satisfies this trend very well as it fits nicely in between the data sets with $r/k_s = 15.2$ and $r/k_s = 30.5$.

At $Re_b = 1.8 \times 10^4$, the DNS yields $C_f = 0.0122$ matching surprisingly well with the pressure-drop measurements with only 0.8% deviation. Note that in the smooth case, the DNS yields a $\approx 5\%$ lower C_f compared to the smooth pressure-drop measurements due to the periodic boundary conditions in the spanwise direction, i.e. neglecting the side walls of the test section. It is expected that for increasingly rough surfaces, as for the reference case homogen_rgh with approx. 100% increase in friction at $Re_b = 1.8 \times 10^4$, the effect of the side walls in the experiments becomes less pronounced. Thus, the difference between periodic DNS and pressure-drop measurements becomes smaller in accordance with the observations.

A comparison of single hot-wire measurements of the smooth and rough reference case obtained at the spanwise centre of the test section with DNS results are presented in figure 6.7. For the smooth reference case, the measured mean velocity is fitted against a law of the wall description proposed by Luchini [65]. In doing so, u_τ and the wall distance of the first measurement point y_0 closest to the wall is determined. This procedure results in a very good collapse of U^+ and uu^+ (dashed lines) in panels (a) and (b), respectively, of figure 6.7. The collapse of DNS and pressure-drop measurements for homogen_rgh suggests that side wall effects can be neglected. Consequently, the measured C_f is used to obtain u_τ for the viscous scaled hot-wire profile of case homogen_rgh. Applying the fitting method as for the smooth reference is deemed unreliable since additional to y_0 and u_τ, also the additive constant of the law of the wall B needs to be obtained. Instead, u_τ and B are obtained from the pressure-drop measurements and only y_0 is fitted based on the law of the wall provided by [65]. This leads to a good collapse of the homogen_rgh profiles in figure 6.7 (a) and in the outer region of figure 6.7 (b) for $y^+ > 200$. Below $y^+ < 200$, the hot-wire measurement yields slightly lower uu^+ compared to the DNS counterpart, which is related to spatial filtering effects of the hot-wire: the viscous scaled hot-wire length L^+ increases from the smooth case $L^+ = 25$ to $L^+ = 48$ leading to substantial attenuation as recently shown for a fully-rough surface by Gatti et al. [39].

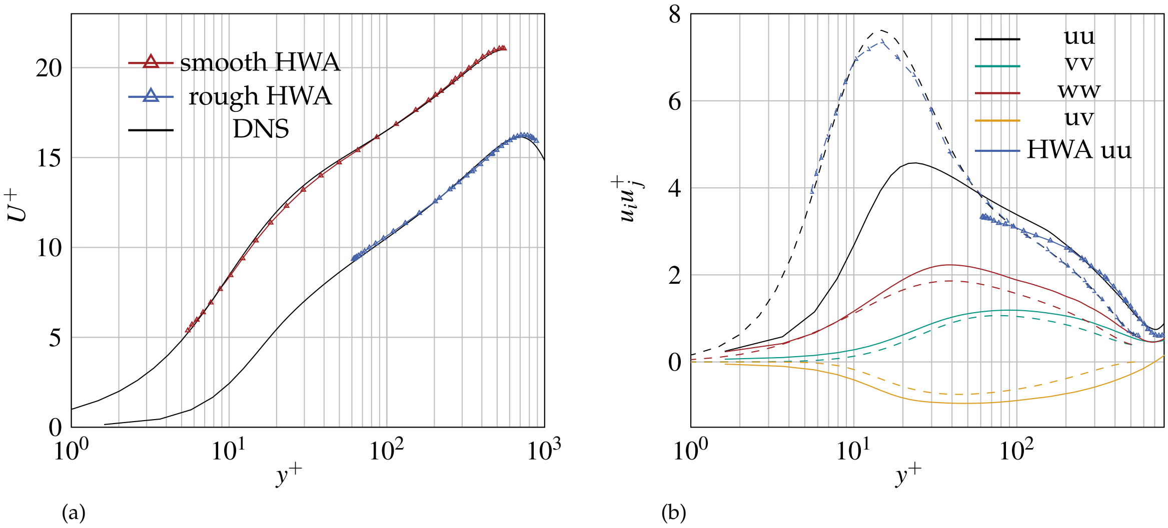

(a) (b)

Figure 6.7: Comparison of mean streamwise velocity U^+ (panel (a)) and Reynolds stresses $u_iu_j^+$ (panel (b)) at matched $Re_b = 1.8 \times 10^4$ for the smooth and homogeneous rough reference case. In Panel (b), dotted lines represent smooth results, while solid lines denote the case homogen_rgh. Viscous scaled hot-wire length $L^+ = 25$ for the smooth and $L^+ = 48$ for the homogenous rough case.

Experimentally, Reynolds number effects are studied and presented in figure 6.8. In panel (a), diagnostic plots of the smooth reference case are shown for a Reynolds number variation in the range of $Re_b =$

1.2×10^4 up to $Re_b = 5.8 \times 10^4$. As expected, with increasing Reynolds number, the linear region in the diagnostic plot extends to lower local velocities U/U_{cl} which can be fitted by a linear relation

$$\frac{u'}{U} = a + b\frac{U}{U_{Cl}} \tag{6.1}$$

with slope b and offset a. Equation (6.1) with $a = 0.314$ and $b = -0.267$ reported by Alfredsson et al. [2] is included for reference in figure 6.8. The measurement points are highlighted with markers for the velocity profile measured at $Re_b = 1.2 \times 10^4$ but omitted for the remaining cases for the sake of clarity. Note that the same miniature hot-wire probe was utilised for all presented Reynolds numbers. Thus, with increasing Reynolds number, stronger spatial filtering effects occur as the viscous scaled hot-wire length L^+ determines whether turbulent fluctuations are attenuated [52]. Comparison of the measured velocity profiles to DNS [51] reveal attenuation below $y^+ < 3L^+$ if $L^+ > 20$. Consequently, the respective wall-normal extent of the velocity fluctuation profiles is highlighted in figure 6.8 as dashed lines to mark potentially biased data. Comparing the smooth diagnostic plots at the highest Reynolds number $Re_b = 5.8 \times 10^4$ indeed reveals a slight mismatch with the reference fit of Alfredsson et al. [2] caused by spatial filtering of turbulent fluctuations.

In panel (b) of figure 6.8, diagnostic plots of the homogeneous rough reference case are shown with respect to the smooth empirical reference of Alfredsson et al. [2]. The distinction between diagnostic plots in the transitionally rough regime depicted in blue and the fully-rough regime depicted in red is made based on the global friction measurements shown in figures 6.6, 6.9 and 6.11, where the onset of the fully-rough regime is $Re_b \approx 3 \times 10^4$. Here, darker colours represent higher Re_b. Based on the attenuation reported in figure 6.7 below $y^+ < 200$, a more conservative criterion is applied to highlight potential attenuation in figure 6.8: the respective $y(U/U_{Cl} = 0.75)$ is set as a threshold for homogen_rgh. $U/U_{Cl} = 0.75$ was found at $y^+ = 200$ for the hot-wire profile with $L^+ = 48$. Interestingly, with increasing Re_b, the diagnostic plots are shifted upwards in the transitionally rough regime and collapse in the fully-rough regime. Castro et al. [12] investigated diagnostic plots above rough surfaces and found collapsing profiles for various roughness configurations in the fully-rough regime. Thus, the collapse of the measured diagnostic plots confirms the reported fully-rough regime beyond $Re_b > 3 \times 10^4$.

6.6 Global Friction Characteristics

As a further step towards a better understanding of the global friction of lateral inhomogeneous surface structures, pressure-drop measurements of the cases specified in table 6.1 are analysed in the following. The skin-friction coefficient C_f as a function of Re_b is presented in figure 6.9. The smooth and homogeneous rough results are shown as black and green markers, respectively. Here, the different markers denote the varying orifice flow meter size employed to measure the volumetric flow rate (see section 3.1.1 and table 3.1 for marker definitions).

As depicted in figure 6.1, three different lateral inhomogeneous configurations are investigated with its dimensions specified in table 6.1. Individually, the two different wavelengths $s/\delta_{\text{avg}} \approx 2$ and $s/\delta_{\text{avg}} \approx 4$ were measured amounting to a total of six measurement campaigns not counting the reference cases. The naming convention introduced in figure 6.1 attached with $2\delta_{\text{avg}}$ or $4\delta_{\text{avg}}$ representing the spanwise wavelength are used in the following. Lighter colours represent a greater spanwise spacing.

Overall, as qualitatively observations drawn from figure 6.9, the smooth ridge cases ridge_xδ, in literature termed as strip-type roughness [68, 69], resemble the $C_f(Re_b)$ behaviour of the smooth reference case with a mild skin-friction increase. Thus, with increasing Re_b, C_f decreases, indicating the lack of

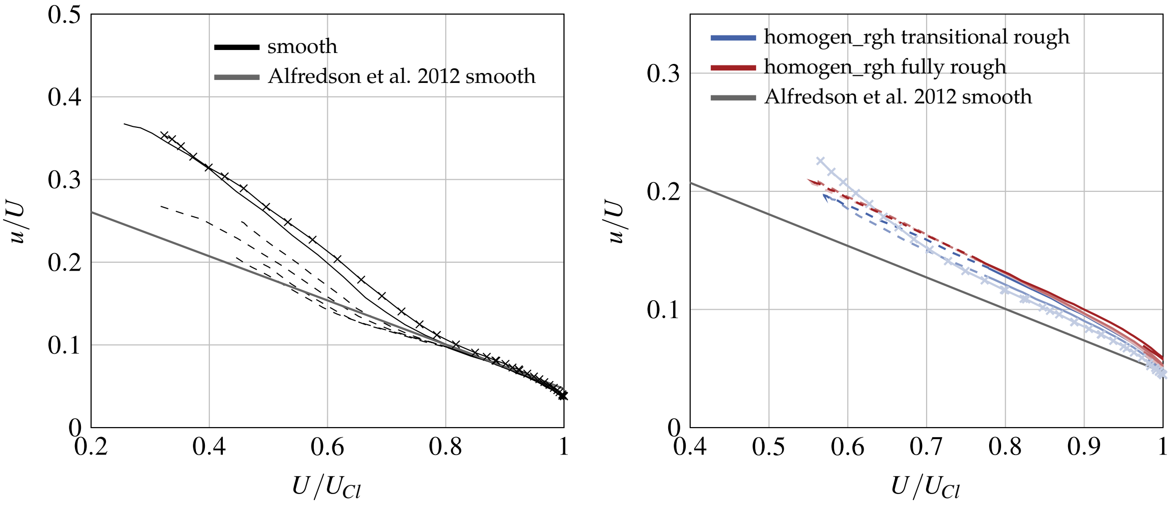

(a)

(b)

Figure 6.8: Diagnostic plots for the smooth (a) and homogeneous rough (b) reference cases. Empirical fit equation (6.1) with parameters for channel flow reported by Alfredsson et al. [2] included for reference. Velocity profiles measured at matching bulk Reynolds numbers for smooth and rough cases. In panel (b) darker colours indicate increasing Re_b. Transitional rough: $Re_b = 1.2, 1.8, 2.85 \times 10^4$. Fully rough: $Re_b = 3.7, 5.0, 5.8 \times 10^4$. Dashed lines represent potential attenuation. Criterion for smooth case: $y^+ < 3L^+$ if $L^+ > 20$, homogen_rgh: $y < y(U/U_{Cl} = 0.75)$ if $L^+ > 20$. Markers included for $Re_b = 1.2 \times 10^4$ indicate the measurement grid used for all cases.

a fully-rough regime for purely two-dimensional surface structuring as discussed in chapter 5. Considering the cases featuring lateral strips of sandpaper strips protruding_rgh_xδ depicted in red and submerged_rgh_xδ depicted in yellow, an interesting observation can be made: while the homogeneous rough reference case homogen_rgh tends to a constant C_f beyond $Re_b > 3 \times 10^4$, i.e. a fully-rough behaviour, cases protruding_rgh_xδ and submerged_rgh_xδ show a slight decrease of C_f with $Re_b \uparrow$, thus indicating the absence of a fully-rough regime. The drag increase is substantially higher compared to

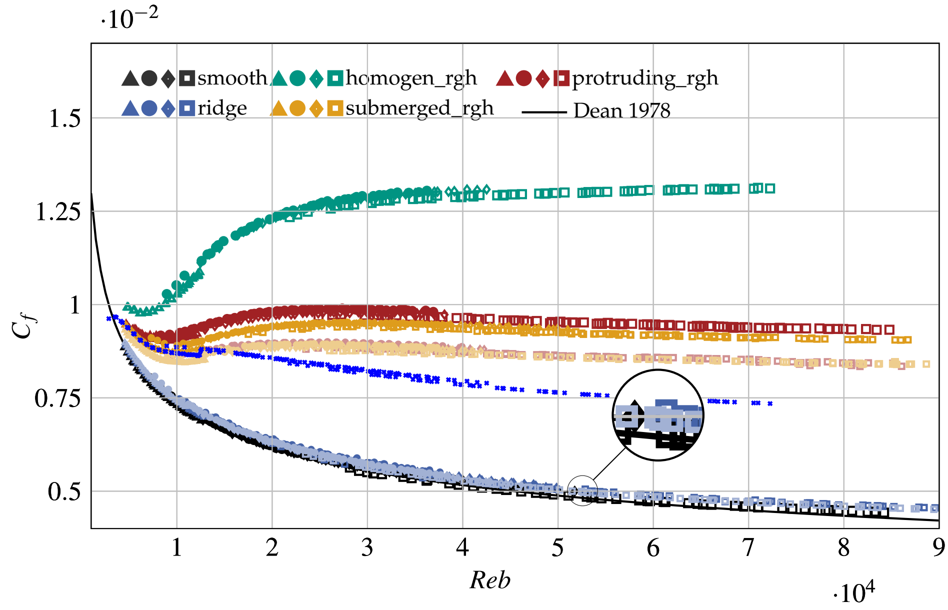

Figure 6.9: Skin-friction coefficient C_f vs. Re_b and for investigated cases as listed in table 6.1. As introduced in table 3.1, different markers indicate different orifice diameters. Dark colour: $s \approx 2\delta_{\text{avg}}$, light colour: $s \approx 4\delta_{\text{avg}}$. $C_{f\,\tau_w=\text{const}}$ (see equation (6.2) for definition) represented as the blue markers.

the smooth ridge cases due to the pronounced introduced roughness effects. The $C_f(Re_b)$ trend of cases protruding_rgh_xδ and submerged_rgh_xδ appears as an intermediate case between ridge_xδ and homogen_rgh, inviting to hypothesize that the observed absence of the fully-rough behaviour is caused by the lateral inhomogeneity.

6.6.1 Implications of the Channel Height Definition

As mentioned before, "the arbitrary choice of the effective channel half-height directly affects C_f and many other flow quantities." [von Deyn et al., 2022a] In this section, the relative drag change $\frac{C_f - C_{f0}}{C_{f0}} = \frac{\Delta C_f}{C_{f0}}$ is discussed as a quantitative measure to assess the implications of different channel height definitions. In panel (a) of figure 6.10, $\frac{\Delta \widetilde{C_f}}{\widetilde{C}_{f0}}$ is shown computed with $\widetilde{\delta}_{\text{avg}}$, which is defined as the distance between the average structure height h_{avg}. For the sake of clarity, quantities computed with $\widetilde{\delta}_{\text{avg}}$ are denoted with $\widetilde{(\cdot)}$.

As an additional reference, the average of smooth and homogen_rgh cases assuming the same τ_w over the smooth and the rough strip

$$\Delta C_{f\,\tau_{\text{w}}=\text{const}} = \left(\frac{1}{2}\left(\frac{1}{\sqrt{C_{f\text{homogen\_rgh}}}} + \frac{1}{\sqrt{C_0}}\right)\right)^{-2} - C_{f0} \qquad (6.2)$$

is shown as the solid blue line. As an initial guess, this could be the expected skin-friction drag of protruding_rgh_xδ and submerged_rgh_xδ since the lateral inhomogenous cases feature 50% sandpaper and 50% smooth aluminium in the experimental domain. However, in figure 6.10(a), all sandpaper cases produce significantly higher drag increase. Comparing the protruding (red datasets) and submerged (yellow) sandpaper configurations, the yellow submerged roughness data points lay below their respective protruding counterparts. Interestingly, the drag increase of the red protruding roughness data points exceeds the sum of $\Delta C_f / C_{f0}$ of the respective smooth (blue) ridges and submerged roughness data points. These observed differences in drag increase are probably related to varying strengths of the large-scale secondary motions. Note that the $s \approx 4\delta$ cases lay closer to equation (6.2) represented by the blue with respect to the $s \approx 2\delta$ counterpart. This matches the expectation that for $s \to \infty$, $\Delta C_f / C_{f0}$ might converge to equation (6.2) since the secondary flows will occupy a diminishing proportion of the span.

From figure 6.10 (a), it can be observed that all $s/\delta \approx 2$ spaced configurations produce more friction drag compared to the respective $s/\delta \approx 4$ configurations. From literature, it is known that the strongest secondary currents are expected for δ spanwise spacing [110], recently confirmed e.g. by sPIV measurements of strip-type roughness [116]. Due to the fact that solely the wavelength s varies between cases and the surface parameters remain constant, the observed increase in friction (between 2δ and $4\,\delta$ spacing) is a strong indication of stronger secondary currents in case of $s \approx 2\delta$.

Comparing the $\frac{\Delta C_f}{C_{f0}}$ plots in panel (b) of figure 6.10, where the laminar reference height is used, to panel (a), the discussed general trends remain unchanged. Overall, smaller values of $\frac{\Delta C_f}{C_{f0}}$ are reported compared to $\frac{\Delta \widetilde{C_f}}{\widetilde{C}_{f0}}$, since $\delta / \delta_{\text{avg}} < 1$. Interestingly, the respective protruding and submerged configuration collapse better when using the laminar wall-normal origin definition with protruding_rgh_4δ and submerged_rgh_4δ collapsing perfectly in panel (b) of figure 6.10. Therefore, the global friction trends are largely independent of the specific choice of the wall-normal origin. At the same time, it is favourable to use a suitable choice of the wall-normal origin in order to achieve collapse between surface configurations of varying physical sizes. A possible choice is presented here utilising the introduced laminar reference. Admittedly, a better collapse between two sets of results cannot be seen as universal proof

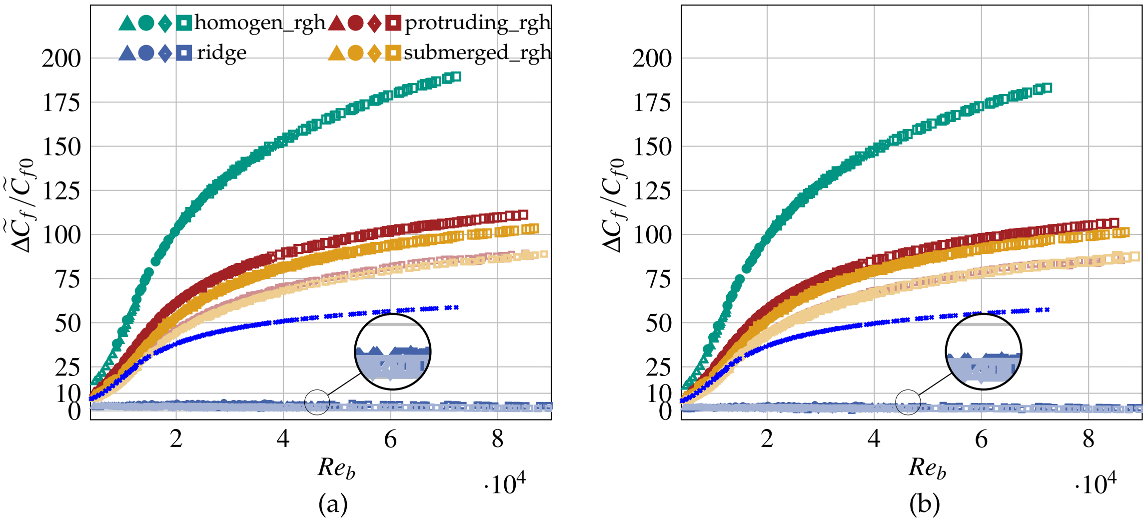

Figure 6.10: Relative drag increase $\Delta C_f/C_{f0}$ as a function of Re_b for investigated cases as listed in table 6.1. Equation (6.2) $\Delta C_{f\,\tau_w=\mathrm{const}}/C_{f0}$ represented as the blue markers. Dark colour: $s \approx 2\delta$, light colour: $s \approx 4\delta$. Panel (a): Wall-normal origin placed at the averaged structure (melt-down) height h_{avg}. $\widetilde{()}$ used to denote the change of the wall-normal origin to h_{avg}. Panel (b): Wall-normal origin placed at h_{lam}, still below the roughness crest.

of this statement but fits nicely with the findings on riblets and ridges. Thus, the laminar frame of reference is further used in the following.

6.6.2 Drag Regimes

As an alternative representation to $\frac{\Delta C_f}{C_{f0}}$ discussed before, the induced drag change of surface roughness is expressed in terms of the effective roughness function ΔU^+. Based on the ΔU^+ as a function of a viscous scaled roughness length scale k^+, different types of surface roughness are distinguished in literature [59]. Thus, the drag-change measurements expressed as ΔU^+ are discussed in the following, as presented in figure 6.11. ΔU^+ is retrieved from C_f and C_{f0} as outlined in §2.2.2. In figure 6.11, ΔU^+ as a function of the laminar height h^+_{lam} is shown. The solid black line corresponds to the fully-rough behaviour [85]

$$\Delta U^+ = \frac{1}{\kappa}\ln k^+ + C. \tag{6.3}$$

with k^+ as a roughness length scale. For choosing $k = h_{\mathrm{lam}}$ as in figure 6.11 and a von Kármán constant of $\kappa = 0.39$, an additive constant of $C = -3.5$ is obtained when matching equation (6.3) with the homogeneous rough reference case homogen_rgh. Quite surprisingly, this is a perfect match with equivalent sand grain roughness function $\Delta U^+ = \frac{1}{\kappa}\ln k_s^+ - 3.5$ [16] and it remains to be investigated if the match of $h_{\mathrm{lam}} = k_s$ is mere coincidence or can also be observed for other homogeneous rough surfaces. With respect to figure 6.11, in this scaling a fully-rough behaviour is evident beyond $h^+_{\mathrm{lam}} \approx 70$ which matches well with the reported threshold Reynolds number $Re_b = 3 \times 10^4$ as discussed in section 6.5.

Comparing the case protruding_rgh_2δ to homogen_rgh and the fully-rough reference in figure 6.11(a), protruding_rgh_2δ appears to be only slightly shifted horizontally from the fully-rough regime between $20 \lessapprox h^+_{\mathrm{lam}} \lessapprox 40$. Beyond $h^+_{\mathrm{lam}} \gtrapprox 50$, a significantly lower ΔU^+ compared to the fully-rough reference is found comparable to the departure from the fully-rough reference for 2D surface structures (see §5.4). The observed absence of a fully-rough behaviour beyond a certain threshold of k^+ might be caused

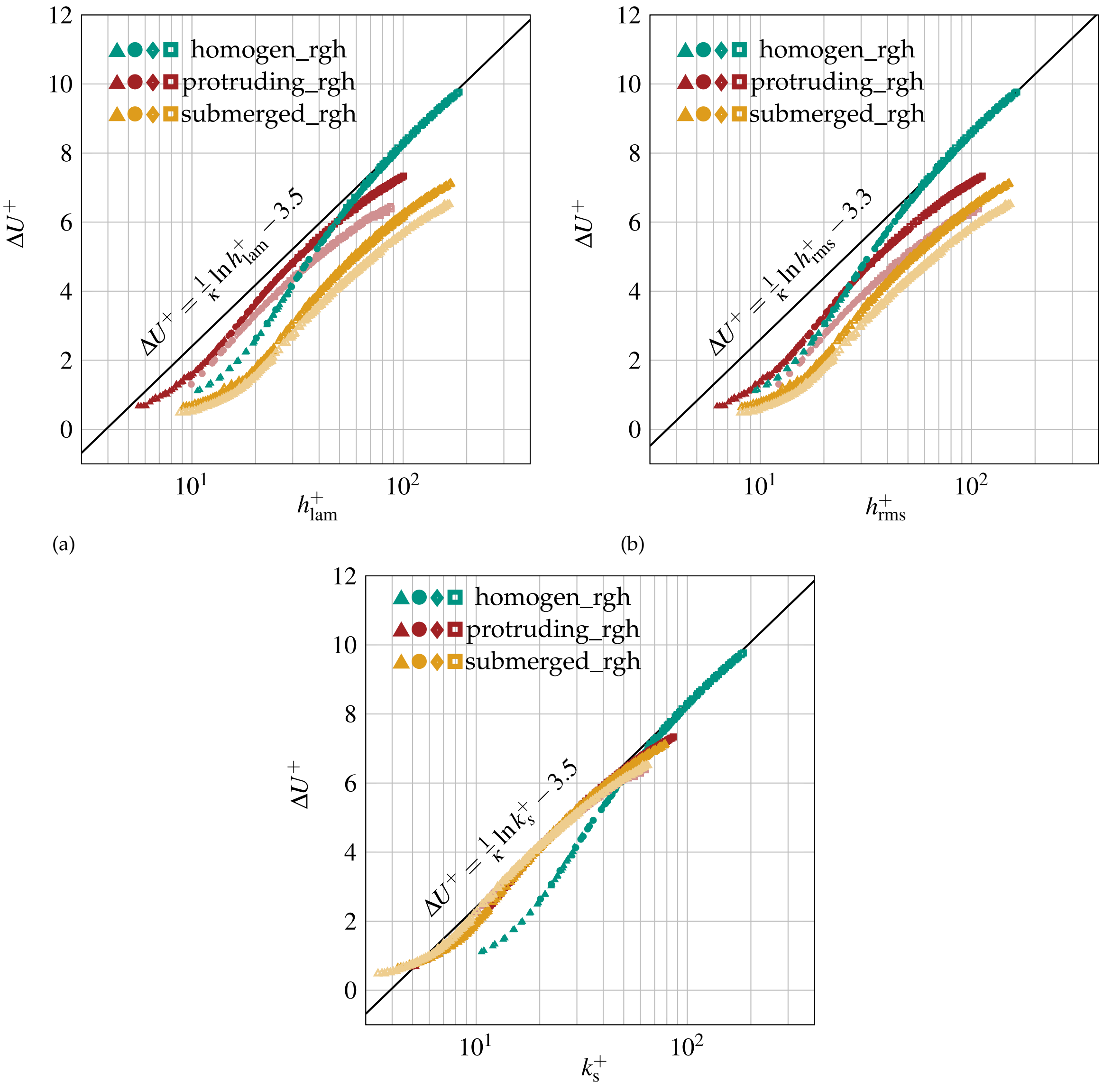

(a)

(b)

(c)

Figure 6.11: Effective roughness function ΔU^+. Panel (a): ΔU^+ vs. h^+_{lam}. Panel (b): ΔU^+ vs. h^+_{rms}. Panel (c): ΔU^+ vs. equivalent sand grain roughness k_s. The fully-rough reference is included in all panels as the black solid line, while κ is set to $\kappa = 0.39$. dark colour: $s \approx 2\delta$, light colour: $s \approx 4\delta$.

by the surface spanwise inhomogeneity and thus shows an interesting analogy with the 2D surface structures (see §5.4).

The wider-spaced configuration protruding_rgh_4δ reveals a qualitatively very similar $\Delta U^+(h^+_{\mathrm{lam}})$ behaviour compared to protruding_rgh_2δ in figure 6.11 (a), although protruding_rgh_4δ produces less friction drag resulting in smaller ΔU^+ for matched h^+_{lam}. Again, similar trends are found for the submerged roughness strip configurations but shifted horizontally due to the approximately two times larger h_{lam} compared to the protruding configurations.

As additional information, ΔU^+ is shown as a function of root mean square of the roughness distribution h_{rms} in figure 6.11 (b). h_{rms} is computed from the numerically investigated surfaces specified in table 6.4. Interestingly, the protruding and submerged cases move closer together in this representation compared to h^+_{lam} scaling presented in panel (a).

In order to enable a direct comparison between all sandpaper strip cases, the equivalent sand grain roughness concept is employed. For each data set, the roughness length scale k is adjusted to match the relation for the Nikuradse sand grain roughness $\Delta U^+(k_s^+) = \frac{1}{\kappa}\ln k_s^+ - 3.5$ [16]. The respective ratio of the laminar roughness height h_{lam} and equivalent sand grain roughness k_s are included in table 6.1. Note that the homogeneous reference case homogen_rgh yields $h_{\mathrm{lam}} = k_s$.

The ΔU^+ results rescaled to the equivalent sand grain size k_s^+ are shown in figure 6.11 (c). In this representation, all sandpaper strip cases collapse with the fully-rough reference as intended and show remarkable agreement with the fully-rough regime for $15 \lessapprox k_s^+ \lessapprox 40$. Interestingly, all lateral inhomogeneous cases experience a clear departure from the fully-rough regime supporting the hypothesis that the observed behaviour is an effect of lateral surface inhomogeneity. Moreover, the respective protruding and submerged configurations agree remarkably in the rescaled k_s representation, while the wider-spaced configurations with $s \approx 4\delta$ lead to an earlier departure from the fully-rough regime.

6.7 Secondary Motions Induced by Sandpaper Strips

In case of lateral inhomogeneous surfaces with a spanwise wavelength of $s/\delta \approx 1-5$, strong secondary motions are expected to significantly alter the time-averaged velocity components [69, 110, 116, 120]. In order to characterise the flow locally and link the present investigation to studies in literature, hot-wire measurements in the $y-z$ cross plane are carried out for the cases protruding_rgh_$x\delta$ and submerged_rgh_$x\delta$. The time-averaged mean velocity U normalised with the global bulk velocity U_b acquired with the orifice flow meter (see §3.1.1) is shown in figure 6.12. The expected domain-filling effect of the secondary motions strongly bulging the iso-lines of U is clearly visible.

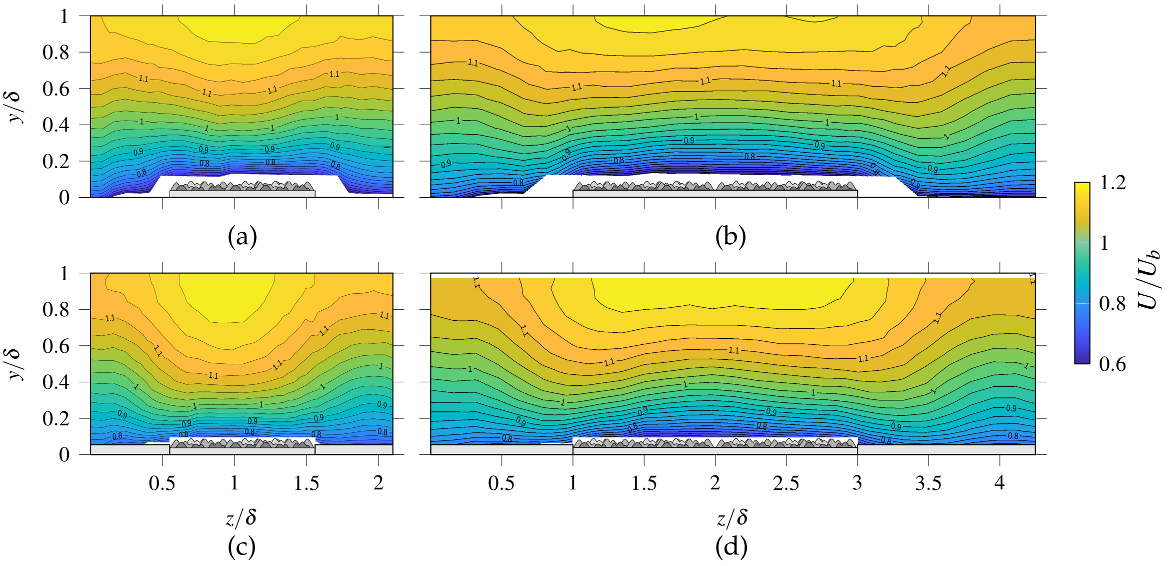

(a) (b) (c) (d)

Figure 6.12: U/U_b contours for all sandpaper cases. Top row: protruding_rgh_xδ, bottom row: submerged_rgh_xδ obtained at $Re_b = 1.8 \times 10^4$. U_b obtained from global flow rate measurements with the orifice flow meter (see section 3.1.1).

Stroh et al. [105] pointed out that turbulent fluctuations are deflected upwards at the edges of protruding rough strips, which reflects in the spanwise wall-normal Reynolds stresses vw. The upward motion at the edges of the protruding strip deflects slower fluid towards the channel centre and thus leads to a local decrease in the time-averaged streamwise velocity U. This effect is detected with the current single hot-wire measurements for the case protruding_rgh_$x\delta$ presented in figure 6.12 (a) and is visible at the roughness strip edges ($z/\delta_{\mathrm{avg}} = 0.6$ and $z/\delta_{\mathrm{avg}} = 1.6$) up to a wall-normal height $y/\delta_{\mathrm{avg}} \approx 0.4$. Moreover, the iso-lines of U are deflected downwards above the protruding strip's centre in the bulk flow region. This suggests a negative time-averaged wall-normal velocity component V in this region.

Other studies featuring comparable spanwise wavelengths are consistent with the suggested interpretation of figure 6.12: Wangsawijaya et al. [116] experimentally and Chung et al. [16] numerically also report a downward motion above the region of higher wall-shear stress for $s/\delta_{\mathrm{avg}} \approx 2$, although their studies are carried out in strip-type configuration. The experiments of Medjnoun et al. [69] confirm the sense of rotation also for smooth ridges with $s/w = 1$, i.e. ridge-type roughness, consistent with the direct numerical study reported by [von Deyn et al., 2021a].

When doubling the spanwise wavelength s as presented in panel (b) of figure 6.12 for the protruding sandpaper strips, the general trends remain similar to protruding_rgh_2δ shown in panel (a) except that the bulging of the iso-lines is less pronounced as the secondary motions are stretched in spanwise direction. Also, an upward deflection of fluid at the roughness strip edges and a slight downward bent of the iso-lines above the roughness strip are observed. Note that an unexpected slight asymmetry of the iso-lines occurs in panel (b) of figure 6.12. During the hot-wire calibration, no drift was detected that could be attributed to the asymmetry. Note that drift effects are compensated with the procedure discussed in §3.1.2. Also, ambient effects are accounted for during the measurement. That leaves a potential slight asymmetry of the investigated roughness strip itself or a slight misalignment of the strips with the streamwise direction as a potential explanation.

Interestingly, when comparing the protruding (top row) to the submerged cases (bottom row) of figure 6.12, the bulging of the U iso-lines is much more strongly pronounced for the submerged roughness cases. This is perhaps counter-intuitive since the strip edges deflect fluids upwards such that one might expect a stronger bulging compared to the submerged case. Instead, the deflections at the strip edges induce additional vortices that counteract the global sense of rotation, as discussed in the following section.

6.7.1 Protruding vs Submerged Sandpaper Strips

In order to gain insight into the secondary motions occurring for the protruding and submerged strip configurations and to detect similarities and differences, DNS simulations of the cases protruding_rgh_2δ and submerged_rgh_2δ at $Re_b = 1.8 \times 10^4$ are discussed in the following.

The obtained mean velocity contours are presented in figure 6.13. Comparing the U/U_b contours to the ones measured with hot-wires, good agreement between measurements and DNS is found. Comparison of the DNS case protruding_rgh_2δ to sPIV and X-wire measurements is shown in appendix A. The downward motion above the roughness strip and the upward motion in the valley between two strips is now clearly visible from the V/U_b contours shown in figure 6.13. This holds true for the protruding as well as the submerged configuration. However, while for the case submerged_rgh_2δ the downward motion occurs over the whole spanwise extent of the roughness strip, for protruding_rgh_2δ a clear upward motion at the roughness strip edges is evident.

This results in different flow topologies, as visualised in figure 6.14, where the secondary motion magnitude $\sqrt{V^2+W^2}/U_b$ overlaid with streamlines indicating the sense of rotation is shown. For the case submerged_rgh_2δ shown in panel (b) of figure 6.14, a simple topology of two domain filling counter-rotating vortices become apparent. Interestingly, it appears from the $\sqrt{V^2+W^2}/U_b$ visualisation that the two vortices are fed by wall-parallel jets in the time-averaged sense, which transport fluid from the roughness strip towards the adjacent valleys. In case of the protruding configuration protruding_rgh_2δ, the same domain filling counter-rotating vortex pair is detected, but the topology is somewhat distorted

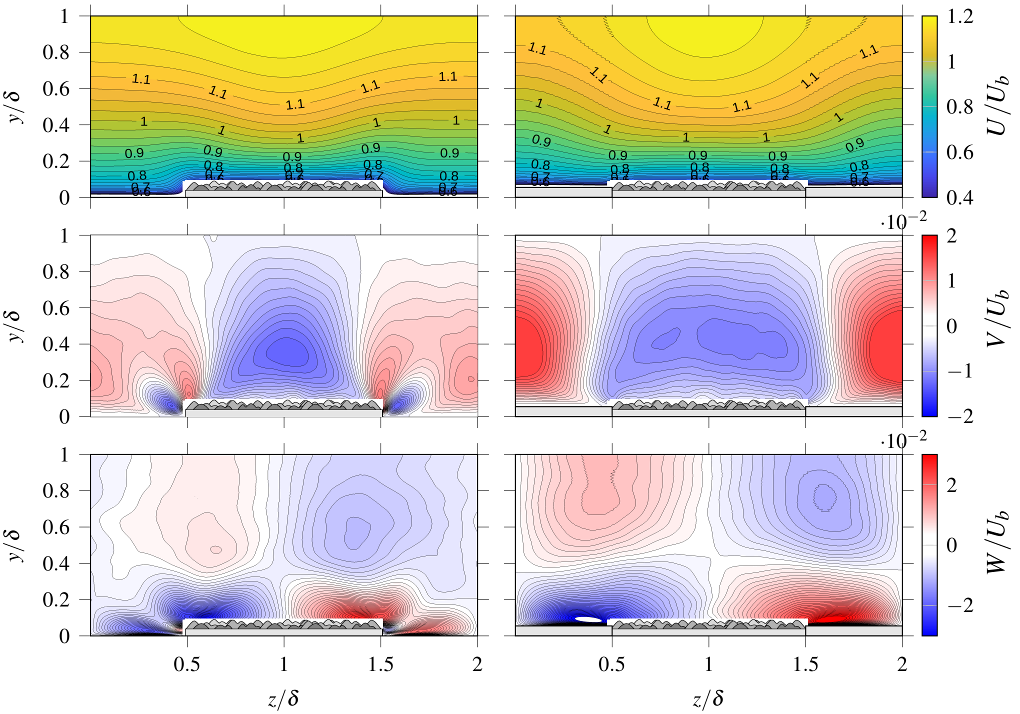

(a) (b)

Figure 6.13: DNS of protruding_rgh_2δ (a) vs. submerged_rgh_2δ (b) mean velocities U, V, W obtained at $Re_b = 1.8 \times 10^4$.

compared to the submerged case since fluid being ejected from the roughness strip towards the valley is moved upwards at the roughness strip edges rather than remaining wall-parallel. Thus, additional vortices are induced at the roughness strip sides, as can be seen when closely inspecting panel (a) of figure 6.14.

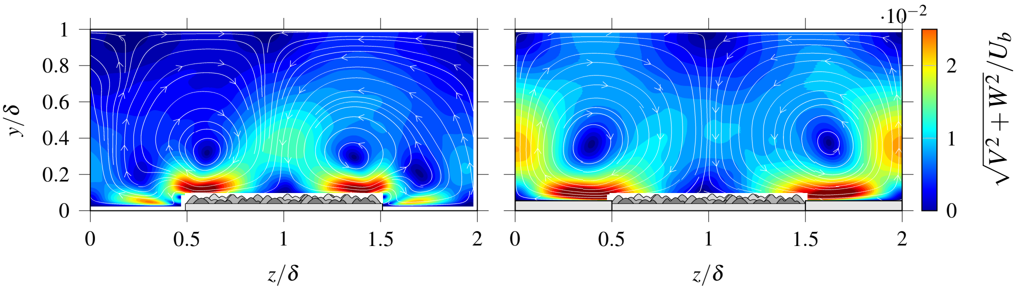

(a) (b)

Figure 6.14: DNS of protruding_rgh_2δ (a) vs. submerged_rgh_2δ (b) secondary motion magnitude $\sqrt{V^2+W^2}/U_b$ overlaid with streamlines obtained at $Re_b = 1.8 \times 10^4$.

As mentioned in the discussion of figure 6.12, the deflections occurring at the roughness strip edges can be observed in the *vw* Reynolds stress, which is visualized in figure 6.15 among all Reynolds stresses of cases protruding_rgh_2δ and submerged_rgh_2δ. Here, the stronger deflections for the protruding case at the edges compared to the submerged case become obvious. A similar trend for the *uw* Reynolds stress is found.

For the remaining Reynolds stress tensor components, the highest magnitude for the submerged configuration occurs at the roughness strip's spanwise centre and fades towards the strip edges. Interestingly, a strong effect of the roughness edges in the protruding configuration is found such that the *uu*, *vv*, *ww* and *uv* contours in the strip edge vicinity are bulged accordingly. Especially the *uv* Reynolds stress, which is directly related to the total friction, shows an increase at the roughness strip edges that fits qualitatively well with the measured higher global friction (§6.6.2) of the protruding vs the submerged configuration.

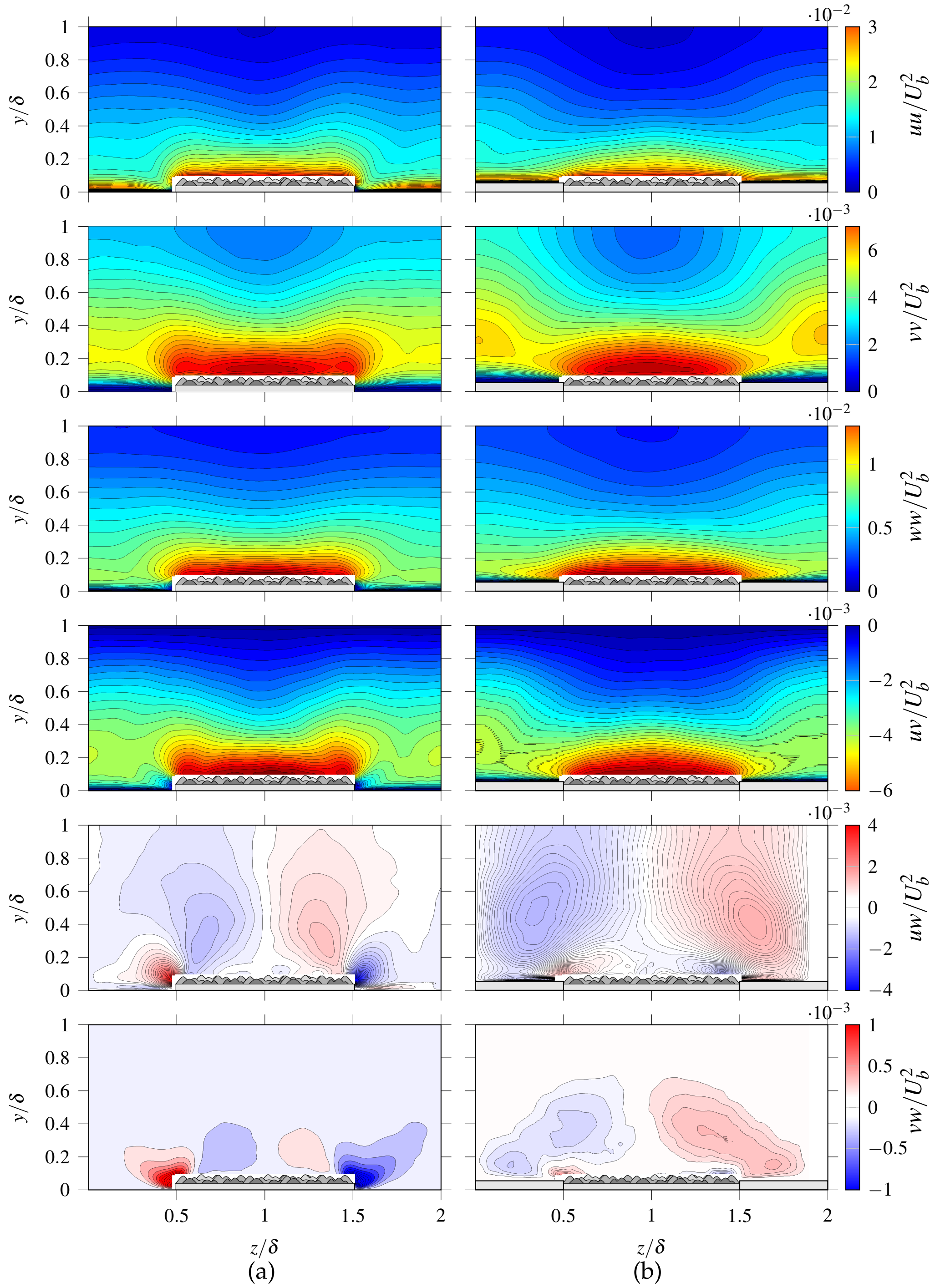

Figure 6.15: DNS of protruding_rgh_2δ (a) vs. submerged_rgh_2δ (b) Reynolds stresses u_iu_j obtained at $Re_b = 1.8 \times 10^4$.

6.7.2 Reynolds Number Effects

As a first step to address the unexpectedly occurring overlap and departure from the fully-rough regime discussed in §6.6.2, additional hot-wire measurements with $Re_b > 1.8 \times 10^4$ are analysed in order to study Reynolds number effects.

Local wall-normal profiles at the spanwise centre above the protruding sandpaper strip for protruding_rgh_2δ and in the valley between two adjacent strips are shown in figure 6.16 in diagnostic representation for four Reynolds numbers. The smooth and homogeneous rough reference profiles discussed in §6.5 with the distinction made between transitional rough (blue lines) and fully rough (red lines) for $Re_b > 3 \times 10^4$ are also included in figure 6.16.

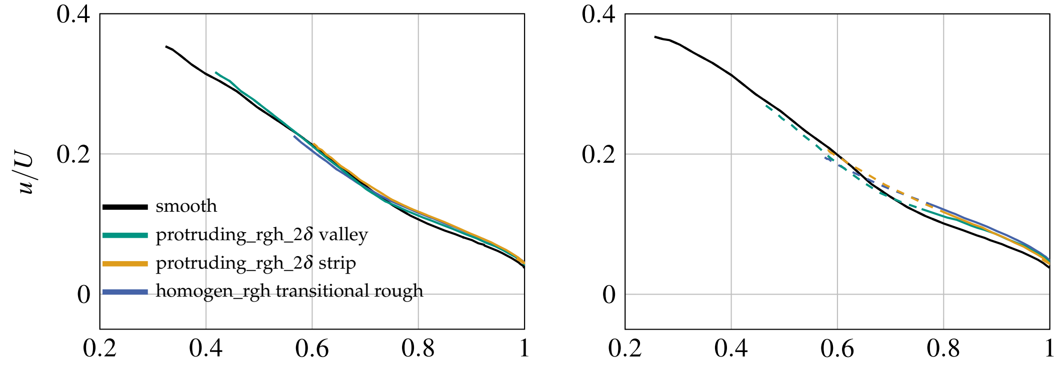

(a) $Re_b = 1.2 \times 10^4$

(b) $Re_b = 1.8 \times 10^4$

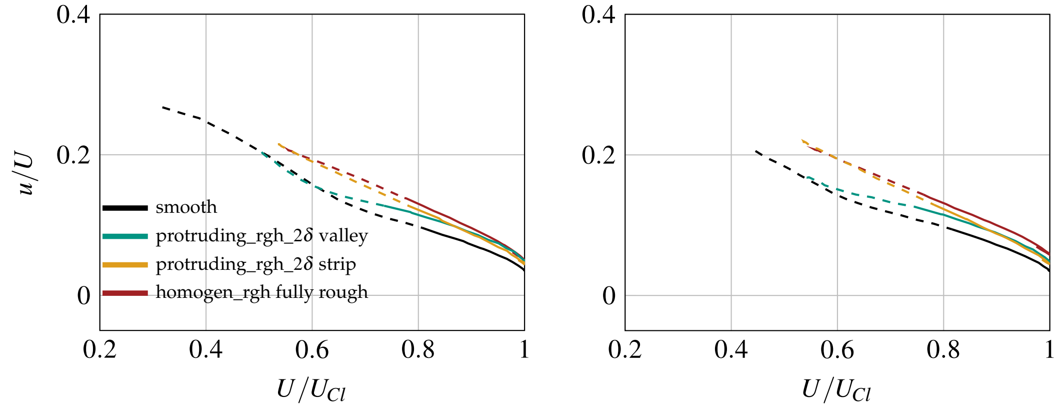

(c) $Re_b = 3.7 \times 10^4$

(d) $Re_b = 5.8 \times 10^4$

Figure 6.16: Reynolds number effects on the diagnostic plots of case protruding_rgh_1δ obtained at the spanwise centre of the protruding sandpaper strip and the middle of the valley with respect to the smooth and homogeneous rough reference (see figure 6.8). The distinction made between transitional rough (blue lines) and fully rough (red lines) for the homogeneous rough reference. Dashed lines represent potential attenuation. Criterion for smooth case: $y^+ < 3L^+$ if $L^+ > 20$, otherwise $y < y(U/U_{Cl} = 0.75)$ if $L^+ > 20$. Panels (a) to (d) show diagnostic plots with increasing Reynolds number spreading from $Re_b = 1.2 \times 10^4$ (panel (a)) to $Re_b = 5.8 \times 10^4$ (panel (d)).

In diagnostic representation, a clear Reynolds number effect of the local velocity profiles is evident for the case protruding_rgh_2δ. Interestingly, for the lowest Reynolds number $Re_b = 1.2 \times 10^4$, all diagnostic profiles collapse in figure 6.16. Note that locally, the velocities differ, e.g. the centerline velocity is strongly affected by the bulging of the U iso-lines. Thus, U_{Cl} above the spanwise centre of the protruding strip is smaller compared to the valley centre in physical units. However, the diagnostic plot features velocity-related quantities only and thus, spatial information such as the wall distance do not influence this representation. Consequently, this behaviour can be interpreted as *local flow similarity* due to the

ID	$Re_b = 1.8 \times 10^4$	$Re_b = 3.7 \times 10^4$	$Re_b = 5.8 \times 10^4$
protruding_rgh_2δ	1.0194±0.2 %	1.0242±0.3 %	1.0214±0.3 %
protruding_rgh_4δ	1.014±0.2 %	1.0169±0.2 %	1.012±0.2 %
sumberged_rgh_2δ	1.0305±0.1 %	1.035±0.1 %	1.0314±0.1 %
sumberged_rgh_4δ	1.0206±0.05 %	1.0227±0.05 %	1.0207±0.05 %

Table 6.6: Reynolds number evolution of the local flow rate of the roughness strip expressed as a bulk velocity U_{b_rgh} with respect to U_{b_glob}. The values stated in the table are the ratio $U_{b\_\mathrm{rgh}}/U_{b\_\mathrm{glob}}$.

collapse of the diagnostic profiles. A similar observation was made by Medjnoun et al. [68] investigating diagnostic plots above smooth ridges inducing secondary motions.

Towards higher Re_b, as the smooth and homogeneous rough references start to deviate and the homogeneous rough case converges for fully-rough behaviour, also the diagnostic profiles above the roughness strip and the valley start to diverge. The observed trend increases gradually throughout panels (a) - (d) of figure 6.16 (i.e. with increasing Reynolds number) and is most pronounced for $Re_b = 5.8 \times 10^4$ depicted in panel (d). Hereby, the diagnostic profile above the roughness strip agrees surprisingly well with the homogeneous rough reference, especially in the wall vicinity. In the valley close to the wall, the diagnostic profile coincides with the smooth reference and tends to the respective profile above the roughness strip in the bulk region. Thus, the roughness effect on the surrounding flow seems most pronounced in the roughness strip vicinity and the bulk region, while the valley seems less affected.

Note that for all Reynolds numbers, the same miniature hot-wire wire probe was used and attenuation effects might occur, as discussed in section 6.5. Thus, measurement points below $y^+ < 3L^+$ if $L^+ > 20$ are highlighted in figure 6.16. However, the comparison for a fixed Reynolds number as presented in figure 6.16 is less problematic, as the viscous scales are in a similar order of magnitude and attenuation thus occurs to a comparable extent.

For a more global analysis, in order to uncover whether changes in the flow distribution with respect to roughness strip and valley occur depending on the Reynolds number, the bulk flow distribution is analysed for the four roughness strip configurations. As such, the bulk velocity is computed for each recorded wall-normal profile based on the measured hot-wire profiles. In table 6.6, the ratio of the spanwise averaged U_b of profiles acquired above the roughness strip U_{b_rgh} with respect to the spanwise average over the entire domain U_{b_glob} is shown.

As expected from the U/U_b contours shown in figure 6.12, more fluid flows over the roughness strip than the valley, i.e. $U_{b\_\mathrm{rgh}}/U_{b\_\mathrm{glob}} > 1$. Quite interestingly, for all investigated roughness strip cases, $U_{b\_\mathrm{rgh}}/U_{b\_\mathrm{glob}}$ is largest for $Re_b = 3.7 \times 10^4$ and therefore in the fully-rough regime. For smaller ($Re_b = 1.8 \times 10^4$) and higher ($Re_b = 5.8 \times 10^4$) Reynolds number, the flow rate distribution across the span is more even, i.e. $U_{b\_\mathrm{rgh}}/U_{b\_\mathrm{glob}}$ is smaller. Comparing the protruding and submerged cases, the submerged configuration exhibits a $\approx 1\%$ (and thus exceeds the uncertainty of the computation of $U_{b\_\mathrm{rgh}}/U_{b\_\mathrm{glob}}$) higher local flow rate above the roughness strip compared to the respective protruding configuration. Note that the obtained U_b from integrating the velocity profile is biased to higher velocities as the near-wall region is not completely resolved. However, since the exact same measurement grid is used between different Reynolds numbers, i.e. spatial positions, comparison between Reynolds numbers is valid.

This preliminary study does not unveil the origins of the occurring fully-rough behaviour or the departure from said regime but clearly hints at a Reynolds number dependence of the spanwise flow rate distribution that deserves to be further investigated in future studies.

7 Conclusion and Outlook

Throughout the thesis, the resulting drag of different types of spanwise heterogeneous surface topographies is investigated experimentally. Emphasis is given to the analysis of pressure-drop measurements resulting in Nikuradse-type diagrams enabling insights into occurring drag regimes. Complementary hot-wire and sPIV measurements are carried out to further link with literature studies and enable the analysis of the local flow. Gradually increasing the complexity, first measurements on eight 2D trapezoidal groove surface structures are carried out, followed by the analysis of spanwise heterogeneous roughness in the form of alternating smooth and sandpaper strips.

As the first main outcome of the present study, the investigation of the 2D surface structures presented in chapter 5 highlights the importance of the choice of the effective channel half height δ. The eight investigated trapezoidal groove surfaces are designed such that the spanwise wavelength s and the structure height h vary over one order of magnitude, including geometrically similar topographies. In dimensionless scaling based on viscous units, the resulting drag-change curves of geometrical similar riblets (structures with $l_g/\delta < 0.17$ are termed riblets in the present work) are expected to collapse as long as the friction Reynolds numbers are in the same order of magnitude. It is shown that the desired collapse is only observed with an appropriate choice of the wall-normal origin, i.e. δ.

"In the present study, the wall-normal origin is placed $h_{\|}$ below the crest of the 2D structures. The streamwise protrusion height $h_{\|}$ is obtained by solving an inexpensive Poisson equation. The resulting effective channel height δ, utilised to translate the measured pressure gradient into an equivalent wall-shear stress of a virtual flat wall, is smaller than the average channel height. The present definition ensures that the relation $C_f = 12/Re_b$, valid for laminar flow over flat surfaces, also holds for laminar flow above the structured ones. In this way, all surface-induced changes of C_f measured in turbulent channel flow stem from turbulent effects only. With this choice of δ, the drag-change curves collapse remarkably well both in the drag reducing regime (all structures achieve maximum drag reduction at $l_g^+ \approx 11$ and cross $\Delta C_f = 0$ at $l_g^+ \approx 17$) and in the drag-increasing regime up to $l_g^+ \approx 40$.

The challenge of choosing a physically-sound value of δ is shared by many recent studies [14, 24, 54] involving surface structuring, not only of the 2D-kind addressed [in chapter 5]. Even numerical studies, where τ_w can be determined directly [...], face this ambiguity as the different problem of the virtual wall placement, typically required to represent spanwise-averaged turbulence statistics. For instance, [54] proposes a virtual wall placement relying upon turbulent statistics obtained a posteriori. Evaluation of the effective wall-shear stress for direct numerical simulations of rough wall flows [32] often also rely on a posteriori methods. Naturally, any a priori method has clear advantages for experimental studies in which the full flow field information is not available. More importantly, one has to be aware of the fact that different definitions of the effective channel height could lead to different interpretations of C_f variations, especially when the scale separation between structure size and boundary layer thickness is not very large." [von Deyn et al., 2022a]

A similar approach to define δ is taken for the heterogeneous roughness cases based on laminar flow solutions. Note that Stokes and laminar flow do not coincide for three-dimensional roughness, such that DNS has been used to obtain the laminar flow solutions. Only a marginal Reynolds number dependence of δ is found when applying the same methodology to define a laminar reference height h_{lam} in analogy

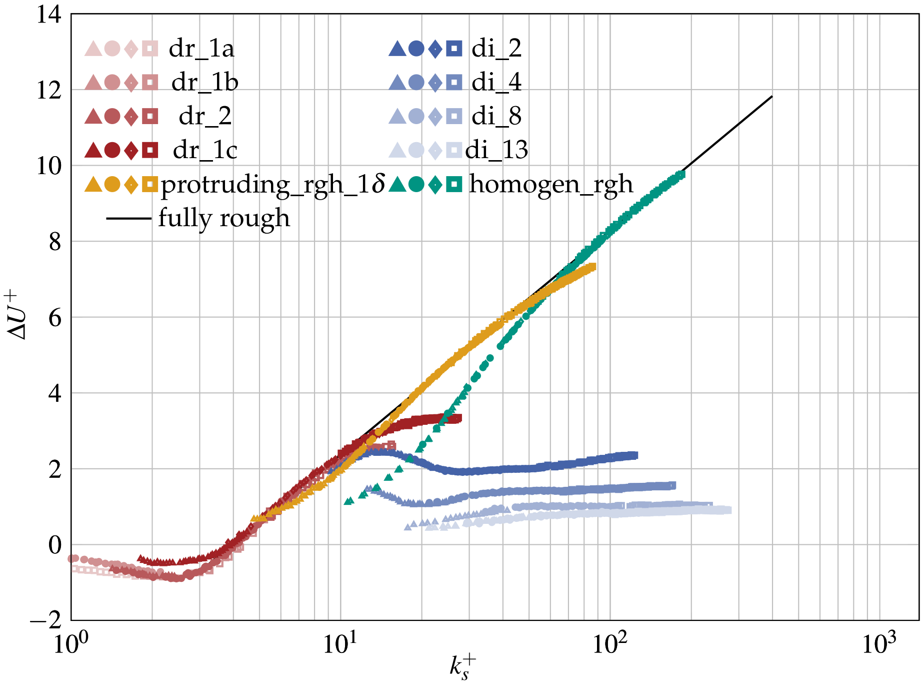

Figure 7.1: Roughness function ΔU^+ vs. equivalent sand grain roughness k_s^+ of selected spanwise heterogeneous topographies discussed in chapters 5 and 6. The friction measurements of homogeneous sandpaper roughness are included for reference as green markers. The black solid line represents fully-rough behaviour $\Delta U = 1/\kappa \ln k_s - 3.5$ with $\kappa = 0.39$

to the procedure used to derive $h_\parallel$. Note that in contrast to the 2D structures, δ defined with h_{lam} does not fulfill $C_f = 12/Re_b$ for the investigated roughness configurations. As such, the physical interpretation of h_{lam} is not as clear as $h_\parallel$ for 2D surface structures. However, utilising this definition of δ still leads to better collapse between the submerged and protruding heterogeneous roughness configurations for a given spanwise wavelength s compared to the h_{avg} based definition δ_{avg}.

The resulting drag-change measurements scaled with the laminar frame of reference are translated into the roughness function ΔU^+. If employing the concept of an equivalent sand grain roughness k_s as commonly done for homogeneous roughness also for the presently investigated spanwise heterogeneous surfaces, the global friction measurements discussed in §5.4.2 and §6.6.2 can be condensed into figure 7.1.

Considering the drag behaviour of the 2D structures shown in shades of blue and red in figure 7.1, "four main outcomes can be drawn from the analysis of the structure-induced drag changes [...]. First, the viscous prediction of riblet drag reduction based on the difference of the streamwise ($h_\parallel$) and spanwise ($h_\perp$) protrusion heights [66] agrees very well with the measured drag-change curve of the physically smallest riblet set `dr_1c` between $1 < l_g^+ < 7$. Also for larger structures such as `dr_1c`, the expected drag-reducing effect known from literature [7, 114] is obtained.

Second, past the drag-reducing regime ($l_g^+ \geq 17$) and up to $l_g^+ \approx 40$, the drag-change curves in terms of the roughness function ΔU^+ plotted against l_g^+ are found to collapse onto one single curve which agrees well with the fully-rough behaviour or rough wall surfaces characterised by a logarithmic increase of the roughness function ΔU^+. Interestingly, data for geometrically similar riblets and ridges are found to collapse in this regime, confirming that the distinction between riblets and ridges is just mere nomenclature. For the equivalent sand grain roughness k_s of the identified (apparent) fully-rough regime, the empirical relation $k_s = l_g/4.4$ is found [for riblets and ridges of different size and spacing], making the drag in this regime predictable. [Note that $k_s = l_g/4.4$ is also used for ridges exceeding the fully-rough regime to scale the data consistently for 2D structures in figure 7.1]. Since riblets and ridges cannot experience any pressure drag (the dominance of which is typically associated with fully-rough drag behaviour), it remains to be understood which flow phenomena induce this phenomenon.

Third, an unexpectedly rich drag behaviour is observed for the first time beyond the fully-rough regime ($l_g^+ \geq 40$). [...] The new data show that such deviation from the fully-rough regime is very complex, with ΔU^+ exhibiting local maxima and minima for two sets of ridges di_2 and di_4. Thus, we term this regime, found between $50 < l_g^+ < 200$ for the investigated geometries, the non-monotonic regime.

Finally, a drag regime beyond $l_g^+ = 200$ is identified in which a hydraulic channel height ratio (similar to a hydraulic diameter concept) is sufficient to describe the drag behaviour of ridges. Riblets might also eventually reach such a regime, but this is not the case for the presently investigated riblet shapes within the Reynolds number range of the experimental facility. The hydraulic channel height ratio η is a quantity obtained a posteriori, which compares the effective hydraulic channel height under turbulent flow conditions to its laminar counterpart, which is exactly the equivalent channel height δ employed for the present study. In the hydraulic channel height regime, η assumes a constant but surface-specific value η_c. Relating this hydraulic surface property to geometrical surface properties remains an open task for which data for different ridge geometries is required." [von Deyn et al., 2022a]

The added homogeneous rough and protruding_rgh_2δ case shown as the green and yellow markers, respectively, put the drag change measurements of the investigated riblets and ridges in perspective to more realistic roughness of three-dimensional character. As expected, the homogeneous roughness case agrees well with the fully-rough reference after surpassing the transitionally rough regime. Interestingly, the drag behaviour of the protruding sandpaper strips appears as a somewhat intermediate case between ridges and irregular roughness. The amount of drag increase is dominated by the presence of roughness, while the "shape" of the $C_f(Re_b)$ curve bears more similarity to the trends of smooth ridges. The presented measurements suggest that a fully rough regime is only intermediately present for roughness strips. At sufficiently large Reynolds numbers, ΔU^+ departs from the fully rough regime as otherwise observed for the two-dimensional surface structuring.

Overall, the presented global friction measurements add to the ongoing endeavour of characterising and predicting flow properties of heterogeneous surfaces. The investigated 2D structures and alternating smooth and rough strips reveal a "transitional" fully-rough behaviour, where k_s based prediction of ΔU^+ is applicable.

Future work should focus on uncovering the origins of the documented unexpectedly rich drag regimes of spanwise heterogeneous topographies. As a side benefit from further experimental investigation of additional 2D surface configurations, the introduced hydraulic height concept can serve as a framework to establish an actual prediction of the drag of 2D surface structures. Methodically, concerted numerical and experimental work seems a promising approach and the analysis of the local flow rate distribution, as briefly discussed in §6.7.2 can serve as a starting point to reveal mechanisms leading to the observed drag regimes.

Bibliography

[1] A. Abdel-Rahman, C. Tropea, P. Slawson, and A. Strong. On temperature compensation in hot-wire anemometry. *Journal of Physics E: Scientific Instruments*, 20(3):315–320, 1987. `doi:10.1088/0022-3735/20/3/017`.

[2] P. H. Alfredsson, R. Örlü, and A. Segalini. A new formulation for the streamwise turbulence intensity distribution in wall-bounded turbulent flows. *European Journal of Mechanics - B/Fluids*, 36:167–175, 2012. `doi:10.1016/J.EUROMECHFLU.2012.03.015`.

[3] W. Anderson, J. M. Barros, K. T. Christensen, and A. Awasthi. Numerical and experimental study of mechanisms responsible for turbulent secondary flows in boundary layer flows over spanwise heterogeneous roughness. *Journal of Fluid Mechanics*, 768:316–347, 2015. `doi:10.1017/jfm.2015.91`.

[4] J. M. Barros and K. T. Christensen. Observations of turbulent secondary flows in a rough-wall boundary layer. *Journal of Fluid Mechanics*, 748:R1–1–R1–13, 2014. `doi:10.1017/jfm.2014.218`.

[5] J. M. Barros, M. P. Schultz, and K. A. Flack. Measurements of skin-friction of systematically generated surface roughness. *International Journal of Heat and Fluid Flow*, 72:1–7, 2018. `doi:10.1016/J.IJHEATFLUIDFLOW.2018.04.015`.

[6] D. W. Bechert and M. Bartenwerfer. The viscous flow on surfaces with longitudinal ribs. *Journal of Fluid Mechanics*, 206:105–129, 1989. `doi:10.1017/S0022112089002247`.

[7] D. W. Bechert, M. Bruse, W. Hage, J. G. V. D. Hoeven, and G. Hoppe. Experiments on drag-reducing surfaces and their optimization with an adjustable geometry. *Journal of Fluid Mechanics*, 338:59–87, 1997. `doi:10.1017/S0022112096004673`.

[8] S. E. Belcher, I. N. Harman, and J. J. Finnigan. The wind in the willows: flows in forest canopies in complex terrain. *Annual Review of Fluid Mechanics*, 44(1):479–504, 2012. `doi:10.1146/annurev-fluid-120710-101036`.

[9] S. Bhattacharya, J. J. Charonko, and P. P. Vlachos. Stereo-particle image velocimetry uncertainty quantification. *Measurement Science and Technology*, 28(1):015301:1–17, 2016. `doi:/10.1088/1361-6501/28/1/015301`.

[10] J. P. Bons, R. P. Taylor, S. T. McClain, and R. B. Rivir. The many faces of turbine surface roughness. *Proceedings of the ASME Turbo Expo*, 3:1–11, 2001. `doi:10.1115/2001-GT-0163`.

[11] I. P. Castro, J. Kim, A. Stroh, and H. C. Lim. Channel flow with large longitudinal ribs. *Journal of Fluid Mechanics*, 915:A92–1–A92–28, 2021. `doi:10.1017/jfm.2021.110`.

[12] I. P. Castro, A. Segalini, and P. H. Alfredsson. Outer-layer turbulence intensities in smooth- and rough-wall boundary layers. *Journal of Fluid Mechanics*, 727:119–131, 2013. `doi:10.1017/JFM.2013.252`.

[13] L. Chan, M. Macdonald, D. Chung, N. Hutchins, and A. Ooi. A systematic investigation of roughness height and wavelength in turbulent pipe flow in the transitionally rough regime. *Journal of Fluid Mechanics*, 771:743–777, 2015. `doi:10.1017/JFM.2015.172`.

[14] C. Chan-Braun, M. García-Villalba, and M. Uhlmann. Force and torque acting on particles in a transitionally rough open-channel flow. *Journal of Fluid Mechanics*, 684:441–474, 2011. `doi:10.1017/JFM.2011.311`.

[15] M. Chevalier. Simson : a pseudo-spectral solver for incompressible boundary layer flows. Technical report, Royal Institute of Technology, Stockholm, Sweden, 2007. URL: `https://www.mech.kth.se/~mattias/simson-user-guide-v4.0.pdf`.

[16] D. Chung, N. Hutchins, M. P. Schultz, and K. A. Flack. Predicting the drag of rough surfaces. *Annual Review of Fluid Mechanics*, 53:439–471, 2021. `doi:10.1146/ANNUREV-FLUID-062520-115127`.

[17] D. Chung, J. Monty, and A. Ooi. An idealised assessment of townsend's outer-layer similarity hypothesis for wall turbulence. *Journal of Fluid Mechanics*, 742:R3–1–R3–12, 2014. `doi:10.1017/jfm.2014.17`.

[18] D. Chung, J. P. Monty, and N. Hutchins. Similarity and structure of wall turbulence with lateral wall shear stress variations. *Journal of Fluid Mechanics*, 847:591–613, 2018. `doi:10.1017/JFM.2018.336`.

[19] C. F. Colebrook, T. Blench, H. Chatley, E. H. Essex, J. R. Finnieome, G. Lacey, J. Williamson, and G. G. Macdonald. Turbulent flow in pipes, with particular reference to the transition region between the smooth and rough pipe laws. *Journal of the Institution of Civil Engineers*, 12:393–422, 1939. `doi:10.1680/IJOTI.1939.14509`.

[20] M. Colombini. Turbulence-driven secondary flows and formation of sand ridges. *Journal of Fluid Mechanics*, 254:701–719, 1993. `doi:10.1017/S0022112093002319`.

[21] M. Colombini and G. Parker. Longitudinal streaks. *Journal of Fluid Mechanics*, 304:161–183, 1995. `doi:10.1017/S0022112095004381`.

[22] G. Daschiel, T. Baier, J. Saal, and B. Frohnapfel. On the flow resistance of wide surface structures. *PAMM*, 12(1):569–570, 2012. `doi:10.1002/pamm.201210273`.

[23] R. B. Dean. Reynolds number dependence of skin friction and other bulk flow variables in two-dimensional rectangular duct flow. *Journal of Fluids Engineering*, 100:215–223, 1978. `doi:10.1115/1.3448633`.

[24] S. Endrikat, D. Modesti, R. García-Mayoral, N. Hutchins, and D. Chung. Influence of riblet shapes on the occurrence of kelvin-helmholtz rollers. *Journal of Fluid Mechanics*, 913:A37–1–A37–34, 2021. `doi:10.1017/JFM.2021.2`.

[25] K. A. Flack. Moving beyond moody. *Journal of Fluid Mechanics*, 842:1–4, 2018. `doi:10.1017/JFM.2018.154`.

[26] K. A. Flack and M. P. Schultz. Roughness effects on wall-bounded turbulent flows. *Physics of Fluids*, 26:101305–1–101305–17, 2014. `doi:10.1063/1.4896280`.

[27] K. A. Flack, M. P. Schultz, and J. M. Barros. Skin friction measurements of systematically-varied roughness: Probing the role of roughness amplitude and skewness. *Flow, Turbulence and Combustion*, 104:317–329, 2019. `doi:10.1007/S10494-019-00077-1`.

[28] K. A. Flack, M. P. Schultz, and J. M. Barros. Skin friction measurements of systematically-varied roughness: Probing the role of roughness amplitude and skewness. *Flow, Turbulence and Combustion*, 104:317–329, 2020. `doi:10.1007/S10494-019-00077-1`.

[29] K. A. Flack, M. P. Schultz, J. M. Barros, and Y. C. Kim. Skin-friction behavior in the transitionally-rough regime. *International Journal of Heat and Fluid Flow*, 61:21–30, 2016. `doi:10.1016/J.IJHEATFLUIDFLOW.2016.05.008`.

[30] K. A. Flack, M. P. Schultz, and J. S. Connelly. Examination of a critical roughness height for outer layer similarity. *Physics of Fluids*, 19(9):095104–1–095104–9, 2007. `doi:10.1063/1.2757708`.

[31] K. A. Flack, M. P. Schultz, and R. J. Volino. The effect of a systematic change in surface roughness skewness on turbulence and drag. *International Journal of Heat and Fluid Flow*, 85:108669, 2020. `doi:10.1016/J.IJHEATFLUIDFLOW.2020.108669`.

[32] P. Forooghi, A. Stroh, F. Magagnato, S. Jakirlić, and B. Frohnapfel. Toward a universal roughness correlation. *Journal of Fluids Engineering, Transactions of the ASME*, 139:121201–1–121201–12, 2017. `doi:10.1115/1.4037280/371945`.

[33] P. Forooghi, A. Stroh, P. Schlatter, and B. Frohnapfel. Direct numerical simulation of flow over dissimilar, randomly distributed roughness elements: a systematic study on the effect of surface morphology on turbulence. *Physical Review Fluids*, 3(4):044605–1–044605–27, 2018. `doi:10.1103/PhysRevFluids.3.044605`.

[34] G. Gamrat, M. Favre-Marinet, S. Le Person, R. Baviere, and F. Ayela. An experimental study and modelling of roughness effects on laminar flow in microchannels. *Journal of Fluid Mechanics*, 594:399–423, 2008. `doi:10.1017/S0022112007009111`.

[35] R. García-Mayoral, G. Gómez-De-Segura, and C. T. Fairhall. The control of near-wall turbulence through surface texturing. *Fluid Dynamics Research*, 51:011410:1–32, 2019. `doi:10.1088/1873-7005/AADFCC`.

[36] R. García-Mayoral and J. Jiménez. Drag reduction by riblets. *Philosophical Transactions of the Royal Society A: Mathematical, Physical and Engineering Sciences*, 369:1412–1427, 2011. `doi:10.1098/RSTA.2010.0359`.

[37] R. García-Mayoral and J. Jiménez. Hydrodynamic stability and breakdown of the viscous regime over riblets. *Journal of Fluid Mechanics*, 678:317–347, 2011. `doi:10.1017/JFM.2011.114`.

[38] D. Gatti, A. Güttler, B. Frohnapfel, and C. Tropea. Experimental assessment of spanwise-oscillating dielectric electroactive surfaces for turbulent drag reduction in an air channel flow. *Experiments in Fluids*, 56:110:1–15, 2015. `doi:10.1007/s00348-015-1983-x`.

[39] D. Gatti, A. Stroh, B. Frohnapfel, and R. Örlü. Spatial resolution issues in rough wall turbulence. *Experiments in Fluids*, 63:63:1–6, 2022. `doi:10.1007/S00348-022-03412-X`.

[40] D. Goldstein, R. Handler, and L. Sirovich. Modeling a no-slip flow boundary with an external force field. *Journal of Computational Physics*, 105:354–366, 1993. `doi:10.1006/JCPH.1993.1081`.

[41] D. B. Goldstein and T. C. Tuan. Secondary flow induced by riblets. *Journal of Fluid Mechanics*, 363:115–151, 1998. `doi:10.1017/S0022112098008921`.

[42] R. Grüneberger and W. Hage. Drag characteristics of longitudinal and transverse riblets at low dimensionless spacings. *Experiments in Fluids*, 50:363–373, 2011. `doi:10.1007/S00348-010-0936-7`.

[43] A. Güttler. High accuracy determination of skin friction differences in an air channel flow based on pressure drop measurements. *Doctoral Thesis, Karlsruher Institut für Technologie (KIT)*, 2015. `doi:10.5445/IR/1000048039`.

[44] B. Hallert. *Photogrammetry, Basic Principles and General Survey*. McGraw-Hill, New York, United States, 1960.

[45] F. R. Hama. Boundary layer characteristics for smooth and rough surfaces. *Transactions of the Society of Naval Architects and Marine Engineers*, 62:333–358, 1954.

[46] F. Hecht. New development in freefem++. *Journal of Numerical Mathematics*, 20(3-4):251–265, 2012. `doi:10.1515/jnum-2012-0013`.

[47] M. T. Hehner. Dielectric-barrier discharge plasma actuators for turbulent friction-drag manipulation via spanwise oscillations. *Doctoral Thesis, Karlsruher Institut für Technologie (KIT)*, 2022, not yet published online.

[48] J. O. Hinze. Secondary currents in wall turbulence. *The Physics of Fluids*, 10:S122–S125, 1967. `doi:10.1063/1.1762429`.

[49] J. O. Hinze. Experimental investigation on secondary currents in the turbulent flow through a straight conduit. *Applied Scientific Research 1973 28:1*, 28:453–465, 1973. `doi:10.1007/BF00413083`.

[50] L. C. Hoagland. *Fully developed turbulent flow in straight rectangular ducts: secondary flow, its cause and effect on the primary flow*. PhD thesis, Massachusetts Institute of Technology, 1962. URL: `http://hdl.handle.net/1721.1/44470`.

[51] S. Hoyas and J. Jiménez. Reynolds number effects on the reynolds-stress budgets in turbulent channels. *Physics of Fluids*, 20:101511–1–101511–8, 2008. `doi:10.1063/1.3005862`.

[52] N. Hutchins, T. B. Nickels, I. Marusic, and M. S. Chong. Hot-wire spatial resolution issues in wall-bounded turbulence. *Journal of Fluid Mechanics*, 635:103–136, 2009. `doi:10.1017/S0022112009007721`.

[53] H. G. Hwang and J. H. Lee. Secondary flows in turbulent boundary layers over longitudinal surface roughness. *Physical Review Fluids*, 3:014608–1–014608–25, 2018. `doi:10.1103/PHYSREVFLUIDS.3.014608`.

[54] J. I. Ibrahim, G. Gómez-de Segura, D. Chung, and R. García-Mayoral. The smooth-wall-like behaviour of turbulence over drag-altering surfaces: a unifying virtual-origin framework. *Journal of Fluid Mechanics*, 915:A56–1–A56–39, 2021. `doi:10.1017/jfm.2021.13`.

[55] International Organization for Standardization. ISO 5167-1:2003 Measurement of fluid flow by means of pressure differential devices inserted in circular cross-section conduits running full - Part 1: General principles and requirements. 2003. URL: `https://www.iso.org/standard/28064.html`.

[56] International Organization for Standardization. ISO 5167-2:2003 Measurement of fluid flow by means of pressure differential devices inserted in circular cross-section conduits running full - Part 2: Orifice plates. 2003. URL: `https://www.iso.org/standard/30190.html`.

[57] U. Ismail, T. A. Zaki, and P. A. Durbin. The effect of cube-roughened walls on the response of rough-to-smooth (rts) turbulent channel flows. *International Journal of Heat and Fluid Flow*, 72:174–185, 2018. `doi:10.1016/j.ijheatfluidflow.2018.05.008`.

[58] T. O. Jelly and A. Busse. Reynolds number dependence of reynolds and dispersive stresses in turbulent channel flow past irregular near-gaussian roughness. *International Journal of Heat and Fluid Flow*, 80:108485:1–17, 2019. `doi:10.1016/J.IJHEATFLUIDFLOW.2019.108485`.

[59] J. Jiménez. Turbulent flows over rough walls. *Annual Review of Fluid Mechanics*, 36:173–196, 2004. `doi:10.1146/ANNUREV.FLUID.36.050802.122103`.

[60] M. A. Jouybari, J. Yuan, G. J. Brereton, and M. S. Murillo. Data-driven prediction of the equivalent sand-grain height in rough-wall turbulent flows. *Journal of Fluid Mechanics*, 912:A8–1–A8–23, 2021. `doi:10.1017/JFM.2020.1085`.

[61] J. H. Lee, H. J. Sung, and P. A. ge Krogstad. Direct numerical simulation of the turbulent boundary layer over a cube-roughened wall. *Journal of Fluid Mechanics*, 669:397–431, 2011. `doi:10.1017/S0022112010005082`.

[62] M. Li, C. M. de Silva, A. Rouhi, R. Baidya, D. Chung, I. Marusic, and N. Hutchins. Recovery of wall-shear stress to equilibrium flow conditions after a rough-to-smooth step change in turbulent boundary layers. *Journal of Fluid Mechanics*, 872:472–491, 2019. `doi:10.1017/jfm.2019.351`.

[63] P. M. Ligrani and R. J. Moffat. Structure of transitionally rough and fully rough turbulent boundary layers. *Journal of Fluid Mechanics*, 162:69–98, 1986. `doi:10.1017/S0022112086001933`.

[64] Y. Liu, J. Li, and A. J. Smits. Roughness effects in laminar channel flow. *Journal of Fluid Mechanics*, 876:1129–1145, 2019. `doi:10.1017/jfm.2019.603`.

[65] P. Luchini. Structure and interpolation of the turbulent velocity profile in parallel flow. *European Journal of Mechanics - B/Fluids*, 71:15–34, 2018. `doi:10.1016/j.euromechflu.2018.03.006`.

[66] P. Luchini, F. Manzo, and A. Pozzi. Resistance of a grooved surface to parallel flow and cross-flow. *Journal of Fluid Mechanics*, 228:87–109, 1991. `doi:10.1017/S0022112091002641`.

[67] M. Macdonald, L. Chan, D. Chung, N. Hutchins, and A. Ooi. Turbulent flow over transitionally rough surfaces with varying roughness densities. *Journal of Fluid Mechanics*, 804:130–161, 2016. `doi:10.1017/JFM.2016.459`.

[68] T. Medjnoun, C. Vanderwel, and B. Ganapathisubramani. Characteristics of turbulent boundary layers over smooth surfaces with spanwise heterogeneities. *Journal of Fluid Mechanics*, 838:516–543, 2018. `doi:10.1017/JFM.2017.849`.

[69] T. Medjnoun, C. Vanderwel, and B. Ganapathisubramani. Effects of heterogeneous surface geometry on secondary flows in turbulent boundary layers. *Journal of Fluid Mechanics*, 886:A31–1–A31–36, 2020. `doi:10.1017/JFM.2019.1014`.

[70] R. Mehta and P. Bradshaw. Design rules for small low speed wind tunnels. *The Aeronautical Journal*, 83:443–453, 1979. `doi:10.1017/S0001924000031985`.

[71] R. Mejia-Alvarez and K. T. Christensen. Wall-parallel stereo particle-image velocimetry measurements in the roughness sublayer of turbulent flow overlying highly irregular roughness. *Physics of Fluids*, 25(11):115109–1–115109–24, 2013. `doi:10.1063/1.4832377`.

[72] D. Modesti, S. Endrikat, N. Hutchins, and D. Chung. Dispersive stresses in turbulent flow over riblets. *Journal of Fluid Mechanics*, 917:A55–1–A5–36, 2021. `doi:10.1017/JFM.2021.310`.

[73] D. Modesti, S. Pirozzoli, P. Orlandi, and F. Grasso. On the role of secondary motions in turbulent square duct flow. *Journal of Fluid Mechanics*, 847:R1–1–R1–11, 2018. `doi:10.1017/jfm.2018.391`.

[74] A. Mohammadi and J. Floryan. Groove optimization for drag reduction. *Physics of Fluids*, 25(11):113601–1–113601–25, 2013. `doi:10.1063/1.4826983`.

[75] A. Mohammadi and J. Floryan. Numerical analysis of laminar-drag-reducing grooves. *Journal of Fluids Engineering*, 137(4):041201–1–041201–12, 2015. `doi:10.1115/1.4028842`.

[76] A. Mohammadi and J. M. Floryan. Pressure losses in grooved channels. *Journal of Fluid Mechanics*, 725:23–54, 2013. `doi:10.1017/jfm.2013.184`.

[77] J. P. Monty, E. Dogan, R. Hanson, A. J. Scardino, B. Ganapathisubramani, and N. Hutchins. An assessment of the ship drag penalty arising from light calcareous tubeworm fouling. *Biofouling*, 32:451–464, 2016. `doi:10.1080/08927014.2016.1148140`.

[78] L. F. Moody. Friction Factor for Pipe Flow. *Transactions of the ASME*, 66:671–684, 1944.

[79] J. Nikuradse. Untersuchungen über turbulente Strömungen in nicht kreisförmigen Rohren. *Ingenieur-Archiv*, 1(3):306–332, 1930. `doi:10.1007/BF02079937`.

[80] J. Nikuradse. Strömungswiderstand in rauhen rohren. *ZAMM - Journal of Applied Mathematics and Mechanics / Zeitschrift für Angewandte Mathematik und Mechanik*, 11:409–411, 1931. `doi:10.1002/ZAMM.19310110603`.

[81] R. Örlü, J. H. Fransson, and P. H. Alfredsson. On near wall measurements of wall bounded flows-the necessity of an accurate determination of the wall position. *Progress in Aerospace Sciences*, 46(8):353–387, 2010. `doi:10.1016/j.paerosci.2010.04.002`.

[82] R. Örlü and R. Vinuesa. *Thermal anemometry*, pages 257–304. CRC Press, Boca Raton, United States, 2017. `doi:10.1201/9781315371733`.

[83] I. Papautsky, J. Brazzle, T. Ameel, and A. B. Frazier. Laminar fluid behavior in microchannels using micropolar fluid theory. *Sensors and Actuators A: Physical*, 73(1-2):101–108, 1999. `doi:10.1016/S0924-4247(98)00261-1`.

[84] F. Pérez-Ràfols and A. Almqvist. Generating randomly rough surfaces with given height probability distribution and power spectrum. *Tribology International*, 131:591–604, 2019. `doi:10.1016/j.triboint.2018.11.020`.

[85] A. E. Perry, W. H. Schofield, and P. N. Joubert. Rough wall turbulent boundary layers. *Journal of Fluid Mechanics*, 37:383–413, 1969. `doi:10.1017/S0022112069000619`.

[86] A. Pinelli, M. Uhlmann, A. Sekimoto, and G. Kawahara. Reynolds number dependence of mean flow structure in square duct turbulence. *Journal of Fluid Mechanics*, 644:107–122, 2010. `doi:10.1017/S0022112009992242`.

[87] S. Pirozzoli. On turbulent friction in straight ducts with complex cross-section: the wall law and the hydraulic diameter. *Journal of Fluid Mechanics*, 846:R1–1–R1–11, 2018. `doi:10.1017/JFM.2018.303`.

[88] M. Placidi and B. Ganapathisubramani. Effects of frontal and plan solidities on aerodynamic parameters and the roughness sublayer in turbulent boundary layers. *Journal of Fluid Mechanics*, 782:541–566, 2015. `doi:10.1017/JFM.2015.552`.

[89] S. B. Pope. *Turbulent Flows*. Cambridge University Press, Cambridge,United Kingdom, 2000. `doi:10.1017/CBO9780511840531`.

[90] L. Prandtl. *Einführung in die Grundbegriffe der Strömungslehre*. Akademische Verlagsgesellschaft, Leipzig, Germany, 1931.

[91] M. Raffel, C. E. Willert, J. Kompenhans, et al. *Particle Image Velocimetry: a Practical Guide*, volume 2. Springer, Berlin, Germany, 1998.

[92] M. R. Raupach, R. A. Antonia, and S. Rajagopalan. Rough-wall turbulent boundary layers. *Applied Mechanics Reviews*, 44:1–25, 1991. `doi:10.1115/1.3119492`.

[93] M. Reader-Harris and J. Sattary. The orifice plate discharge coefficient equation. *Flow Measurement and Instrumentation*, 1(2):67–76, 1990. `doi:10.1016/0955-5986(90)90031-2`.

[94] A. Rouhi, D. Chung, and N. Hutchins. Direct numerical simulation of open-channel flow over smooth-to-rough and rough-to-smooth step changes. *Journal of Fluid Mechanics*, 866:450–486, 2019. `doi:10.1017/jfm.2019.84`.

[95] A. G. Roy, T. Buffin-Bélanger, H. Lamarre, and A. D. Kirkbride. Size, shape and dynamics of large-scale turbulent flow structures in a gravel-bed river. *Journal of Fluid Mechanics*, 500:1–27, 2004. `doi:10.1017/S0022112003006396`.

[96] K. Schäfer, A. Stroh, P. Forooghi, and B. Frohnapfel. Modelling spanwise heterogeneous roughness through a parametric forcing approach. *Journal of Fluid Mechanics*, 930:A7–1–A7–22, 2022. `doi:10.1017/JFM.2021.850`.

[97] L. Schiller. Über den strömungswiderstand von rohren verschiedenen querschnitts und rauhigkeitsgrades. *ZAMM - Journal of Applied Mathematics and Mechanics / Zeitschrift für Angewandte Mathematik und Mechanik*, 3:2–13, 1923. `doi:10.1002/ZAMM.19230030102`.

[98] H. Schlichting. *Boundary-Layer Theory, 7th edition*. McGraw-Hill, New York, United States, 1979.

[99] C. Schönecker and S. Hardt. Assessment of drag reduction at slippery, topographically structured surfaces. *Microfluidics and Nanofluidics*, 19(1):199–207, 2015. `doi:10.1007/s10404-015-1565-5`.

[100] M. Schultz and K. Flack. Outer layer similarity in fully rough turbulent boundary layers. *Experiments in fluids*, 38(3):328–340, 2005. `doi:10.1007/s00348-004-0903-2`.

[101] P. R. Spalart and J. D. Mclean. Drag reduction: enticing turbulence, and then an industry. *Philosophical Transactions of the Royal Society A: Mathematical, Physical and Engineering Sciences*, 369:1556–1569, 2011. `doi:10.1098/RSTA.2010.0369`.

[102] J. H. Spurk. *Fluid Mechanics*. Springer International Publishing, Cham, Switzerland, 3rd edition, 2020. `doi:10.1007/978-3-030-30259-7`.

[103] D. T. Squire, C. Morrill-Winter, N. Hutchins, M. P. Schultz, J. C. Klewicki, and I. Marusic. Comparison of turbulent boundary layers over smooth and rough surfaces up to high reynolds numbers. *Journal of Fluid Mechanics*, 795:210–240, 2016. `doi:10.1017/JFM.2016.196`.

[104] A. Stroh, K. Schäfer, P. Forooghi, and B. Frohnapfel. Secondary flow and heat transfer in turbulent flow over streamwise ridges. *International Journal of Heat and Fluid Flow*, 81:108518:1–13, 2020. `doi:10.1016/J.IJHEATFLUIDFLOW.2019.108518`.

[105] A. Stroh, K. Schäfer, B. Frohnapfel, and P. Forooghi. Rearrangement of secondary flow over spanwise heterogeneous roughness. *Journal of Fluid Mechanics*, 885:R5–1–R5–12, 2020. `doi:10.1017/JFM.2019.1030`.

[106] A. A. R. Townsend. *The Structure of Turbulent Shear Flow*. Cambridge University Press, Cambridge, United Kingdom, 1956.

[107] R. L. Townsin. The ship hull fouling penalty. *Biofouling*, 19(S1):9–15, 2003. `doi:10.1080/0892701031000088535`.

[108] M. Uhlmann, A. Pinelli, G. Kawahara, and A. Sekimoto. Marginally turbulent flow in a square duct. *Journal of Fluid Mechanics*, 588:153–162, 2007. `doi:10.1017/S0022112007007604`.

[109] University of Southampton. Roughness database. `http://roughnessdatabase.org/`, 2020. Accessed: 2022-08-24.

[110] C. Vanderwel and B. Ganapathisubramani. Effects of spanwise spacing on large-scale secondary flows in rough-wall turbulent boundary layers. *Journal of Fluid Mechanics*, 774:R2–1–R2–12, 2015. `doi:10.1017/JFM.2015.292`.

[111] C. Vanderwel, A. Stroh, J. Kriegseis, B. Frohnapfel, and B. Ganapathisubramani. The instantaneous structure of secondary flows in turbulent boundary layers. *Journal of Fluid Mechanics*, 862:845–870, 2019. `doi:10.1017/JFM.2018.955`.

[112] R. Vinuesa, A. Noorani, A. Lozano-Durán, G. K. E. Khoury, P. Schlatter, P. F. Fischer, and H. M. Nagib. Aspect ratio effects in turbulent duct flows studied through direct numerical simulation. *Journal of Turbulence*, 15(10):677–706, 2014. `doi:10.1080/14685248.2014.925623`.

[113] T. von Kármán. Turbulence and skin friction. *Journal of the Aeronautical Sciences*, 1:1–20, 1934. `doi:10.2514/8.5`.

[114] M. J. Walsh. Effect of detailed surface geometry on riblet drag reduction performance. *Journal of Aircraft*, 27(6):572–573, 1990. `doi:10.2514/3.25323`.

[115] M. J. Walsh and A. Lindemann. Optimization and application of riblets for turbulent drag reduction. In *22nd Aerospace Sciences Meeting*, pages 347:1–10, 1984. `doi:10.2514/6.1984-347`.

[116] D. D. Wangsawijaya, R. Baidya, D. Chung, I. Marusic, and N. Hutchins. The effect of spanwise wavelength of surface heterogeneity on turbulent secondary flows. *Journal of Fluid Mechanics*, 894:A7–1–A7–36, 2020. `doi:10.1017/jfm.2020.262`.

[117] Y. Wu and K. Christensen. Outer-layer similarity in the presence of a practical rough-wall topography. *Physics of Fluids*, 19(8):085108–1–085108–15, 2007. `doi:10.1063/1.2741256`.

[118] J. Yang, A. Stroh, D. Chung, and P. Forooghi. Direct numerical simulation-based characterization of pseudo-random roughness in minimal channels. *Journal of Fluid Mechanics*, 941:A47–1–A47–34, 2022. `doi:10.1017/jfm.2022.331`.

[119] J. Yuan and U. Piomelli. Roughness effects on the reynolds stress budgets in near-wall turbulence. *Journal of Fluid Mechanics*, 760:R1–1–R1–12, 2014. `doi:10.1017/JFM.2014.608`.

[120] A. Zampiron, S. Cameron, and V. Nikora. Secondary currents and very-large-scale motions in open-channel flow over streamwise ridges. *Journal of Fluid Mechanics*, 887:A17–1–A17–25, 2020. `doi:10.1017/JFM.2020.8`.

[121] I. F. Zidane, K. M. Saqr, G. Swadener, X. Ma, and M. F. Shehadeh. On the role of surface roughness in the aerodynamic performance and energy conversion of horizontal wind turbine blades: a review. *International Journal of Energy Research*, 40:2054–2077, 2016. `doi:10.1002/ER.3580`.

Journal Publications

[Gatti et al., 2020] Gatti, D., von Deyn, L. H., Forooghi, P., and Frohnapfel, B. (2020). Do riblets exhibit fully rough behaviour? *Experiments in Fluids*, 61(3):1–6. doi: 10.1007/s00348-020-2921-0.

[von Deyn et al., 2020] von Deyn, L., Forooghi, P., Frohnapfel, B., Schlatter, P., Hanifi, A., and Henningson, D. (2020). Direct numerical simulations of bypass transition over distributed roughness. *AIAA journal*, 58(2):702–711. doi: 10.2514/1.J057765.

[von Deyn et al., 2022a] von Deyn, L. H., Gatti, D., and Frohnapfel, B. (2022a). From drag reducing riblets to drag increasing ridges. *Journal of Fluid Mechanics*, 951:A6–1–A6–24. doi: 10.1017/jfm.2022.796.

[von Deyn et al., 2022b] von Deyn, L. H., Schmidt, M., Örlü, R., Stroh, A., Kriegseis, J., Böhm, B., and Frohnapfel, B. (2022b). Ridge-type roughness: from turbulent channel flow to internal combustion engine. *Experiments in Fluids*, 63:1–16. doi: 10.1007/S00348-021-03353-x.

Conference Contributions

[Hehner et al., 2021] Hehner, M. T., Deyn, L. H., Serpieri, J., Gatti, D., and Frohnapfel, B. (2021). Stereo piv of a plasma actuator applied in a fully-developed turbulent channel flow. *14th International Symposium on Particle Image Velocimetry - ISPIV 2021*. doi: 10.18409/ispiv.v1i1.117 .

[von Deyn et al., 2019a] von Deyn, L. H., Coppini, L., Hehner, M. T., Kriegseis, J., Gatti, D., Forooghi, P., and Frohnapfel, B. (2019a). Riblets in fully developed turbulent channel flow: an experimental campagin. *European Drag Reduction and Flow Control Meeting - EDRFCM 2019*. doi: 10.5445/IR/1000090546 .

[von Deyn et al., 2021a] von Deyn, L. H., Gatti, D., Frohnapfel, B., and Stroh, A. (2021a). Parametric study on ridges inducing secondary motions in turbulent channel flow. *PAMM*, 20:e202000139:1–3. doi: 10.1002/PAMM.202000139 .

[von Deyn et al., 2021b] von Deyn, L. H., Hehner, M. T., Serpieri, J., Kriegseis, J., Gatti, D., and Frohnapfel, B. (2021b). Riblets in the rough regime. *13th international ERCOFTAC Symposium on Engineering Turbulence Modeling and Measurements, ETMM 2021*. doi: 10.5445/IR/1000145506.

[von Deyn et al., 2019b] von Deyn, L. H., Örlü, R., Gatti, D., Kriegseis, J., Frohnapfel, B., and Stroh, A. (2019b). Turbulent channel flows with secondary motions: A concerted dns and experimental study. *11th International Symposium on Turbulence and Shear Flow Phenomena, TSFP 2019*. doi: 10.5445/IR/1000097958.

[von Deyn et al., 2022] von Deyn, L. H., Stroh, A., Gatti, D., and Frohnapfel, B. (2022). Global friction of uniform vs. heterogeneous sandpaper roughness. *12th International Symposium on Turbulence and Shear Flow Phenomena, TSFP 2022*. doi: 10.5445/IR/1000150166.

Nomenclature

All indices used (i,j,k...) run from $1-3$. The superscript $^+$ marks quantities scaled in viscous units.

Latin letters – Upper case

SYMBOL	SI UNIT	DESCRIPTION
A	m^2	duct cross section
AR		aspect ratio
B		additive constant of the law of the wall
C		additive constant of the roughness function
C_f		skin-friction coefficient
E	V	hot-wire voltage
D	m	pipe diameter
D_{hyd}	m	hydraulic diameter
P	m	perimeter
Ra	m	average roughness
Re_b		bulk Reynolds number
Re_{Cl}		centreline Reynolds number
Re_D		pipe Reynolds number
Re_τ		friction Reynolds number
L	m	(hot-wire) length
L_x	m	streamwise simulation domain size
L_y	m	wall-normal simulation domain size
L_z	m	spanwise simulation domain size
N		number of grid points
T	K	Temperature
U	m/s	time averaged streamwise velocity
U_b	m/s	bulk velocity
U_{Cl}	m/s	centreline velocity
$\dot{V}_0$	m^3/s	volumetric flow rate
V	m/s	time averaged wall-normal velocity

W	m/s	time averaged spanwise velocity
W_{duct}	m	width of the test section

Latin letters – Lower case

SYMBOL	SI UNIT	DESCRIPTION
a		offset of linear fit
a_q	%	humidity
b		slope of linear fit
d	m	inner orifice diameter
f	Hz	frequency
h	m	structure height
h_{avg}	m	spanwise averaged height
h_{lam}	m	laminar reference height
$h_{\|\|}$	m	streamwise protrusion height
$h_{\perp}$	m	spanwise protrusion height
k	m	roughness length scale
k_s	m	equivalent sand grain roughness
l_g	m	square root of the groove area
$\dot{m}$	kg/s	mass flow rate
p	Pa	pressure
p_{amb}	Pa	ambient pressure
r	m	radius
s_r	m	ridge width
s	m	spanwise wavelength
t	s	time
$u_i u_j$	$\mathrm{m}^2/\mathrm{s}^2$	Reynolds stresses
w_{strip}	m	roughness strip width
x	m	streamwise coordinate
y	m	wall-normal coordinate
z	m	spanwise coordinate

Greek letters – Upper case

SYMBOL	SI UNIT	DESCRIPTION
Δp	Pa	pressure difference
Δp_0	Pa	orifice pressure difference
Δt	s	sPIV time delay
ΔU^+		roughness function
Π	Pa/m	streamwise pressure gradient

Greek letters – Lower case

SYMBOL	SI UNIT	DESCRIPTION
α		angle
β		orifice diameter ratio
δ	m	(effective) channel half height
δ_{avg}	m	average channel half height defined with h_{avg}
δ_{hyd}	m	hydraulic channel half height
η		hydraulic channel height ratio
κ		von Kármán constant
λ		friction factor
ε		expansion coefficient
ν	m^2/s	kinematic viscosity
ρ	kg/m^3	fluid density
σ	%	relative uncertainty
τ_w	Pa	(effective) wall shear stress

Subscripts

SYMBOL	DESCRIPTION
0	smooth reference value at matched Re_b
avg	spanwise average
in	quantity defined at the wind tunnel inlet
max	maximum occuring value
out	quantity defined at the test section outlet

Abbreviations

SYMBOL	DESCRIPTION
1D	one-dimensional
2D	two-dimensional
DNS	direct numerical simulation
HWA	hot-wire anemometry
FDM	fused deposition modeling
PDF	probability density function
PS	power spectral
SLA	stereolithography
sPIV	stereoscopic particle image velocimetry

List of Figures

List of Tables

A Comparison of DNS, sPIV and X-Wire Measurements

For the local characterization of the two-dimensional flow above lateral inhomogeneous surface structuring, stereoscopic particle image velocimetry (sPIV) is adopted in the present work (see §5.5). The respective setup is described in §3.2. In order to assess the suitability and possible limitations of the chosen measurement technique, sPIV measurements are compared to direct numerical simulations (DNS) and hot-wire measurements in X-wire configuration for trapezoidal groove ridges (data set di_13) and protruding sandpaper strips (data set protruding_rgh_2δ).

The DNS method is described in §5.5.2 for 2D ridges di_13 and §6.3 for the protruding sandpaper strips, respectively. For both DNS, the same code is used, which is featured in a series of recent publications [32, 105, 118].

The X-wire measurements are based on the hot-wire anemometry set-up as described in section 3.1.2. After the first measurements campaign measuring the wall-normal velocity component, the X-wire probe is rotated by precisely 90° and a second measurement is carried out to measure the wall-parallel velocity.

The obtained mean velocity fields and Reynolds stresses are shown in figure A.1 and A.2 for data set di_13 and A.3 and A.4 for data set protruding_rgh_2δ, respectively. Very good agreement is found between DNS and sPIV, demonstrating the suitability of the current sPIV set-up to resolve mean flow properties and Reynolds stresses adequately. Since the sPIV domain is limited to the field of view of the experiment, only half of the spanwise wavelength is captured. For the X-wire measurements, the full domain, including the valley between two adjacent ridges, is measured. However, limitations of the spatial resolution are clearly visible as the X-wire probe has a sensing length of ≈ 1 mm of each individual wire. Crucially, the averaging occurs also in wall-normal direction since two wires are adopted at 90° angle, covering an area of $\approx 1\,\mathrm{mm}^2$ in the $y-z$ cross plane. With respect to the relatively small half-channel height of $\delta \approx 12.6\,\mathrm{mm}$, mean velocities and Reynolds stresses are surprisingly accurately resolved with the X-wire measurements. An additional limitation is apparent, e.g. comparing the wall-normal and spanwise mean velocity measured with the X-wire probe: only two velocity components can be distinguished at a time. Due to the three-dimensional character of the occurring secondary motions, the non-streamwise components are superposed when measuring with an X-wire probe and hence cannot be properly distinguished. Nevertheless, qualitatively consistent trends with DNS and sPIV are found. The limitations of the sPIV method become clearly visible when analyzing the uw and vw Reynolds stress for the protruding sandpaper strips protruding_rgh_2δ displayed in figure A.4. Since the secondary motions are less pronounced for this case compared to the ridge case di_13, also the turbulent fluctuations are weaker in the averaged sense and are close to the background noise level. Even so, the correct topology and approximate magnitude are still resolved when compared to the DNS results.

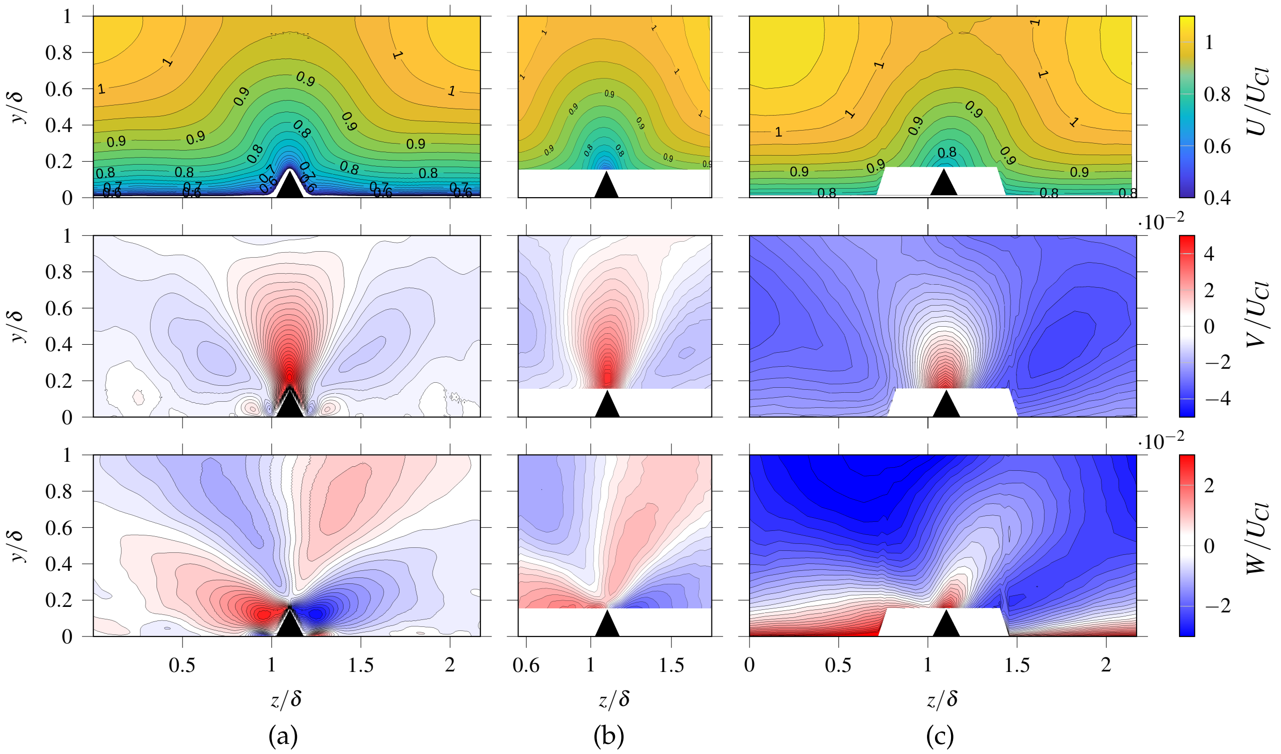

Figure A.1: DNS (a) vs. sPIV (b) vs. X-wire (c) mean velocities U, V, W normalized with U_{Cl} obtained at $Re_b = 1.8 \times 10^4$ for the smooth ridge case di_13.

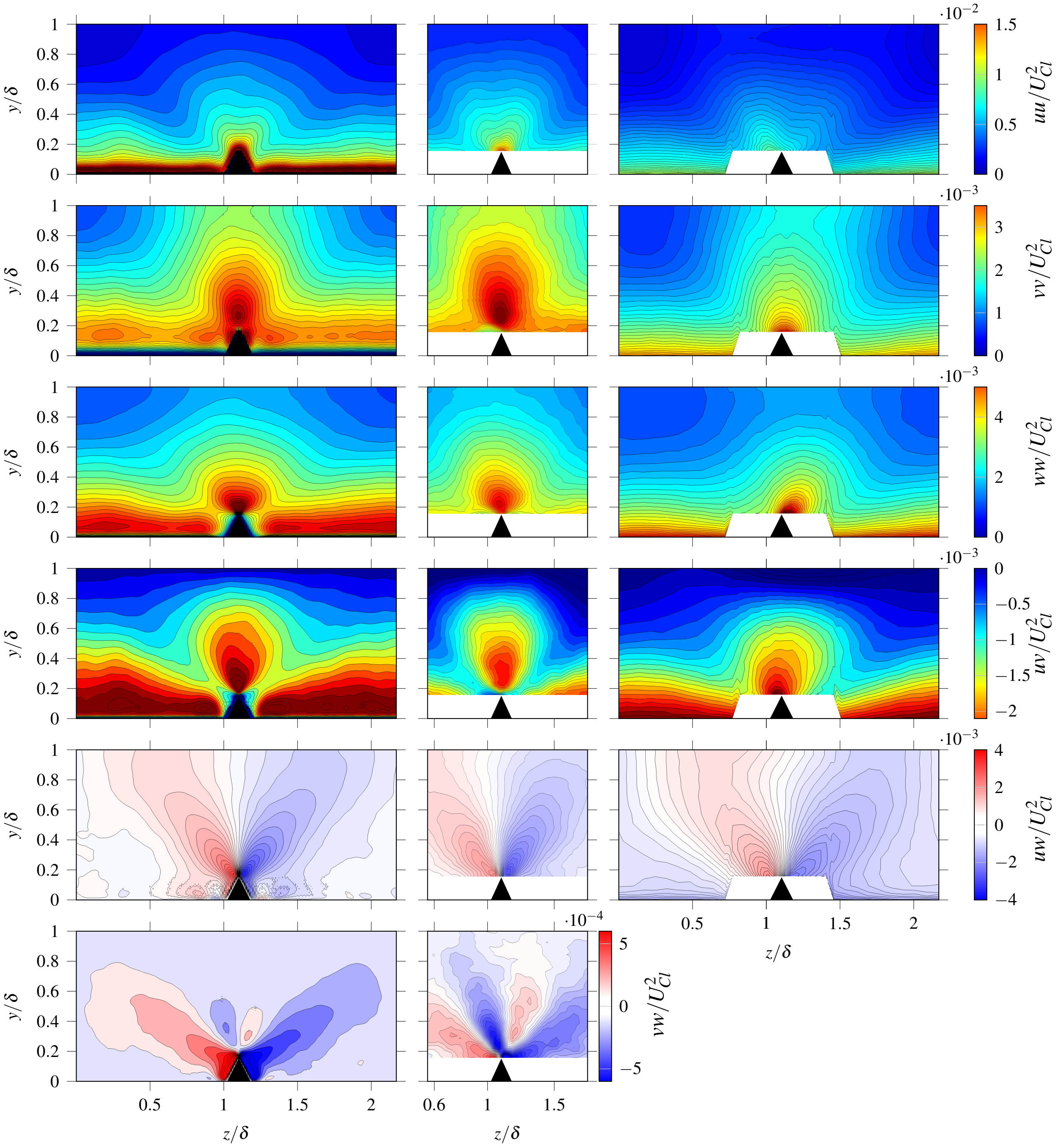

Figure A.2: DNS (a) vs. sPIV (b) vs. X-wire (c) Reynolds Stresses $u_i u_j / U_{Cl}^2$ obtained at $Re_b = 1.8 \times 10^4$ for the smooth ridge case di_13.

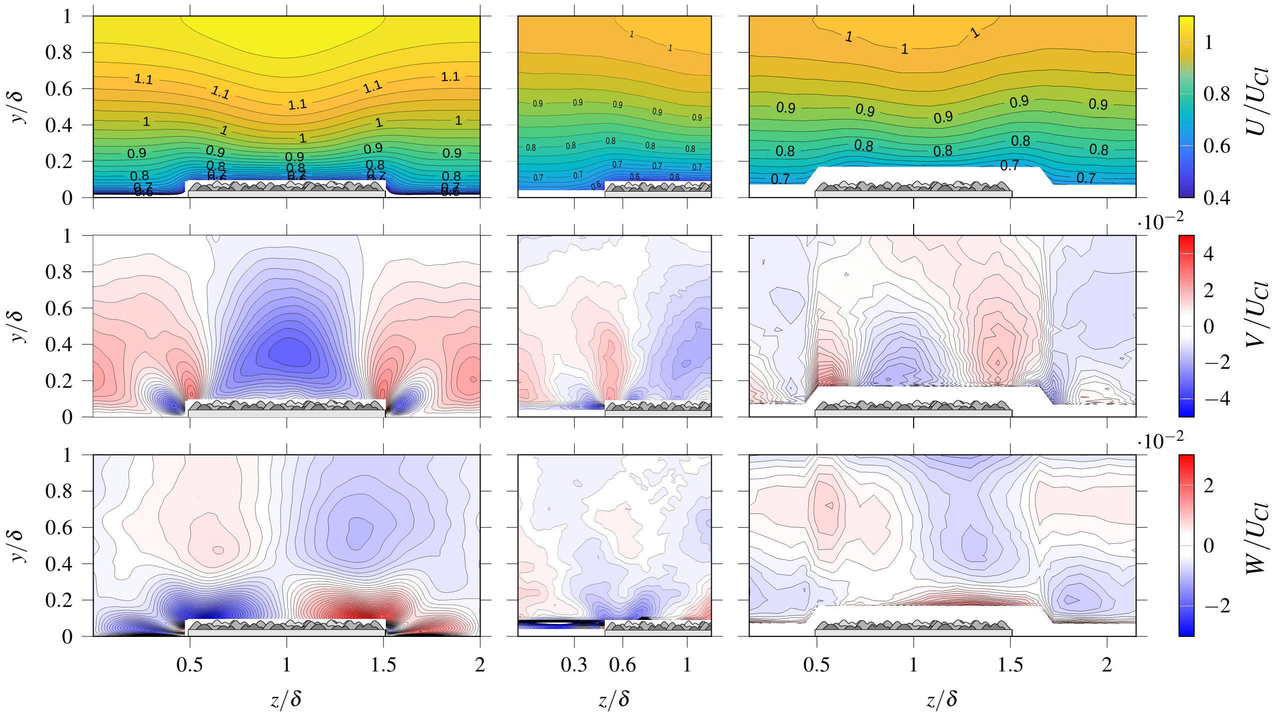

(a) (b) (c)

Figure A.3: DNS (a) vs. sPIV (b) vs. X-wire (c) mean velocities U, V, W normalized with U_{Cl} obtained at $Re_b = 1.8 \times 10^4$ measured above the protruding sandpaper strip case protruding_rgh_2δ.

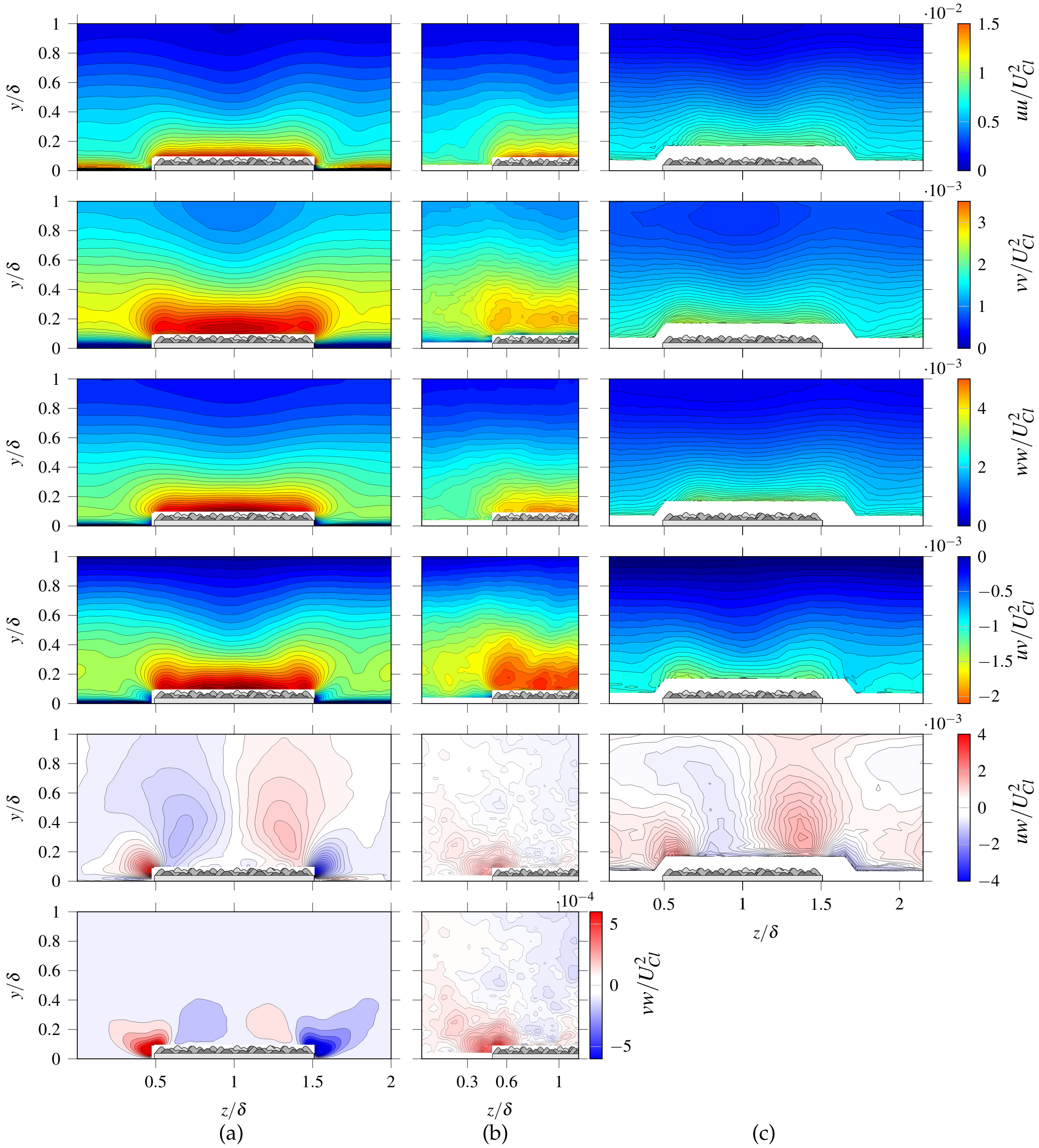

(a) (b) (c)

Figure A.4: DNS (a) vs. sPIV (b) vs. X-wire (c) Reynolds Stresses $u_i u_j / U_{Cl}^2$ obtained at $Re_b = 1.8 \times 10^4$ measured above the protruding sandpaper strip case protruding_rgh_2δ.

B Additive Manufacturing of Surface Structures

B.1 Additive Manufacturing Set-Up

Low force stereolithography (SLA) 3D printing is adopted to manufacture parabolic-shaped riblets. This geometry shape is chosen since it is particularly challenging to manufacture. Thus, challenges in the manufacturing process can be uncovered. Moreover, reliable friction measurements are available in literature [7] and can serve as a reference case for the present investigation.

The utilized Formlabs Form 3L printer is shown in figure B.1. SLA printing has the advantage of reaching higher spatial resolutions and a smoother surface finish compared to standard fused Deposition Modeling (FDM) printers at the expense of longer printing time and additional post-processing steps. The utilized Form 3L printer has a spatial resolution of $25\mu m \times 25\mu m$ in the built plane (see figure B.6 panel (a)) and a layer height of $50\mu m$ is chosen.

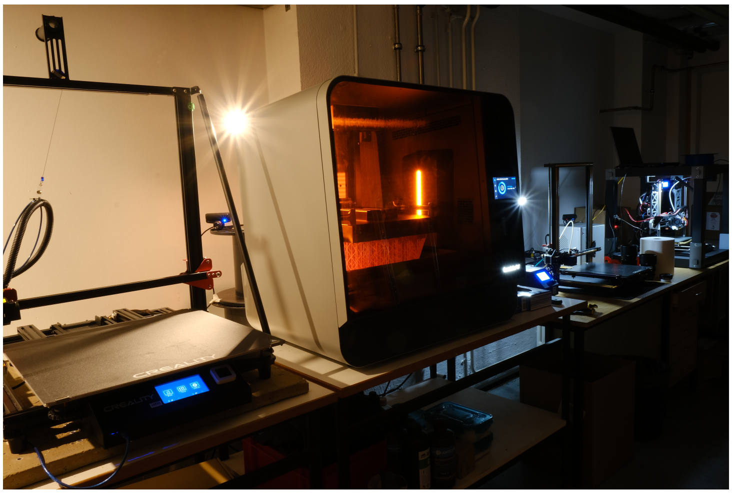

Figure B.1: Overview of the 3D printing facility @ ISTM, including the utilized Formlabs Form3L printer for the present study.

After a print is completed, the resin needs to be washed with isopropanol and cured under UV light. An FDM 3D printed frame is used to simplify the plate handling (see B.2 panel(a)) and avoid damaging the sensitive part. Special attention needs to be paid to the UV curing of the printed parts to avoid warping. Simply putting a weighted glass plate on both sides of the printed riblet plate prevents the warping effect but could damage the very sensitive riblet tips. To this end, vacuum channels are printed on the back side of the riblet plate and a groove close to the edges is printed, where a vacuum proof sealing is placed. The UV curing is executed while employing a vacuum to the back side of the riblet plate. An extensive parametric study is conducted on the sealing groove dimensions to ensure the evenness of the riblet plate: during vacuum conditions, seal tightness needs to be guaranteed. At the same time, a too-small grove would permanently bend the riblet plate. Thus, groove dimensions and the vacuum sealing need to be optimized in a joint effort. The UV curing set-up is depicted in panel (b) of figure B.2.

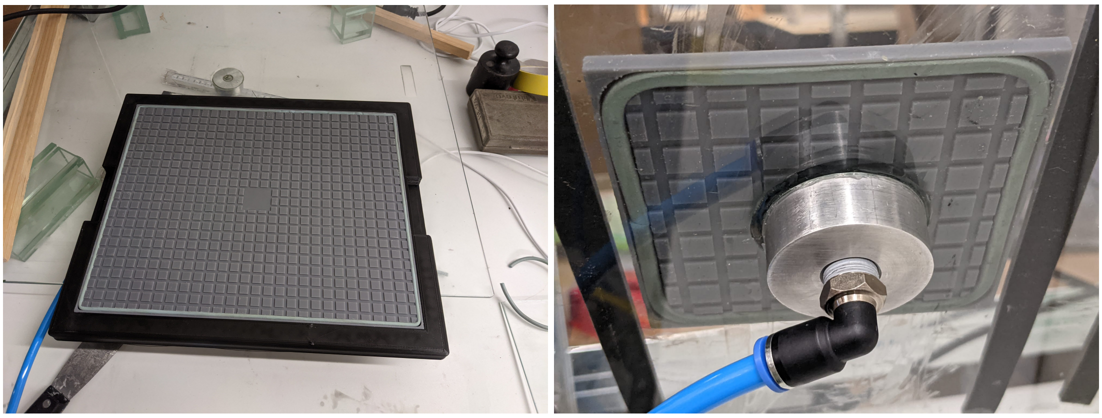

Figure B.2: UV vacuum supported curing: (a): Riblet plate with FDM printed black frame for handling, vacuum channels and vacuum proof sealing. (b): Vacuum curing setup shown while the vacuum pump is running for a smaller 100 mm × 100 mm test plate.

B.2 Manufacturing of Parabolic Riblets

The design parameters of the investigated parabolic riblets are listed in table B.1 with its dimensions introduced in figure B.3. The shape can be thought of as sawtooth-like riblets carved out until they meet the desired parabolic shape. The height $h = s = 0.7\,\mathrm{mm}$ is chosen that the expected optimum drag reduction is reached at $Re_b \approx 8000$, well above the lower limit for a fully developed turbulent channel flow $Re_b = 4500$ in the utilized blower tunnel [43]. Thus, the riblets are discretized with 14 layers, keeping in mind the wall-normal resolution of 50 µm. Theoretically, the layer height can be reduced to 25 µm once the printer software allows doing so. Of course, this is at the expense of additional print time, which is already substantial with approximately seven days for two riblet plates that can be printed simultaneously with the 50 µm layer height. Keep in mind that six such print jobs are needed to equip the whole 1500 mm downstream section of the wind tunnel with riblets.

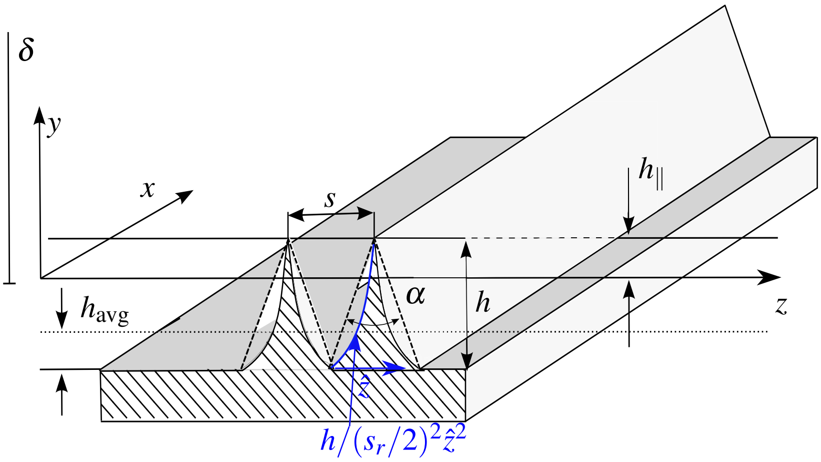

Figure B.3: Sketch of the parabolic surface structures including the origin definition. $h_{||}$ represents the parallel protrusion height [66], h_{avg} the averaged (melt-down) height. The half-channel height δ is defined as the distance between the channel centreline and $h_{||}$ below the structures crest.

In order to assess the obtained surface quality of the 3D printed riblets, optical scans obtained with a Sensofar S neox white light interferometer were conducted. Figure B.4 shows the raw data of such a surface scan.

ID	s/δ	h/δ	s/s_r	α [°] /shape	l_g/δ	P/s	$h_\parallel/s$ $\times 10^{-1}$	$h_\perp/s$ $\times 10^{-2}$
parabolic	0.0584	0.0584	1	$h/(s_r/2)^2$	0.0533	2.32	1.791	8.083

Table B.1: Dimensions of the investigated parabolic riblets. P denotes the perimeter, l_g is the square root of the groove area [36]. $h_\parallel$, $h_\perp$ are the parallel and perpendicular protrusion heights measured from the tip [66].

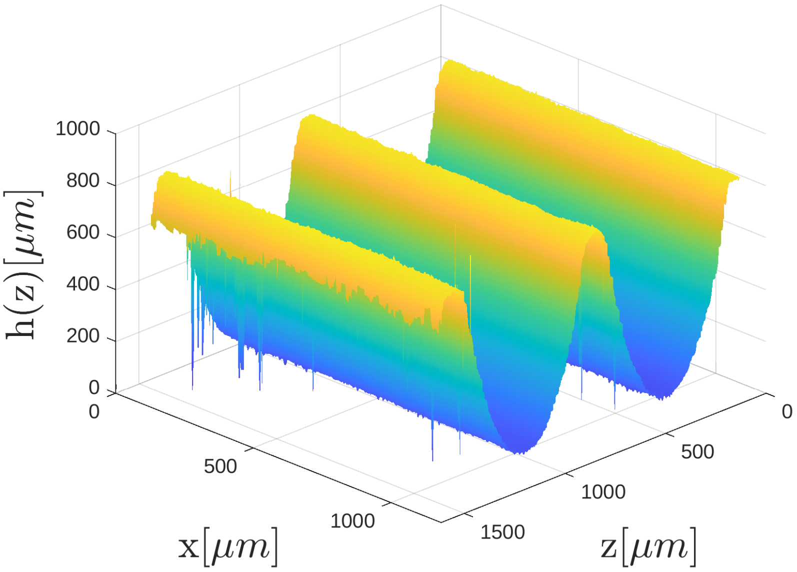

Figure B.4: Exemplary Surface scan obtained with a Sensofar S neox white light interferometer.

While analyzing the scan, a systematic height deviation is detected. The streamwise averaged surface profile $h(z)$ is shown in figure B.5 with respect to the parabolic design geometry. When comparing the green line representing the measured profile with the design geometry, ≈ 0.17 mm lower rib height compared to the desired 0.7 mm is detected. To account for this systematic deviation, a parametric study on the height is conducted. The height in the prescribed CAD model is varied between 0.7 mm and 1.2 mm, as denoted in the caption of figure B.5. The resulting averaged $h(z)$ profiles are shown in figure B.5. Prescribing a height of 0.9 mm results in a reasonable match with the prescribed height of 0.7 mm. Moreover, it can be observed that for all prescribed heights, a considerable tip rounding occurs related to the limited spatial resolution of the 3D printer. For the chosen setting represented by the red line, a tip radius of $r = 40\,\mu\text{m}$ is detected. Nevertheless, a discretization effect of the 3D printing process is expected and can be less crucial in the context of roughness studies. Figure B.6 depicts the resulting 3D printed parabolic riblet plates and their orientation within the print volume. A parametric study leads to the conclusion that the best print quality, while still fitting two riblet plates in the print volume, is achieved when orienting the riblet plates at 18 deg to the vertical axis. Panel (b) of figure B.6 shows a printed riblet plate still sitting on the built platform, including the utilized support structures. Since the built volume can only fit riblet plates with 260 mm streamwise extent, six plates need to be stitched together in order to cover the complete 1500 mm. As can be seen from figure B.6, the support structures leave small dimpled marks on the interface surface. In order to achieve a smooth transition without any disturbance between the individual riblet plates, the upstream and downstream edges are cut with a high precision CNC milling machine to a streamwise length of 250 mm.

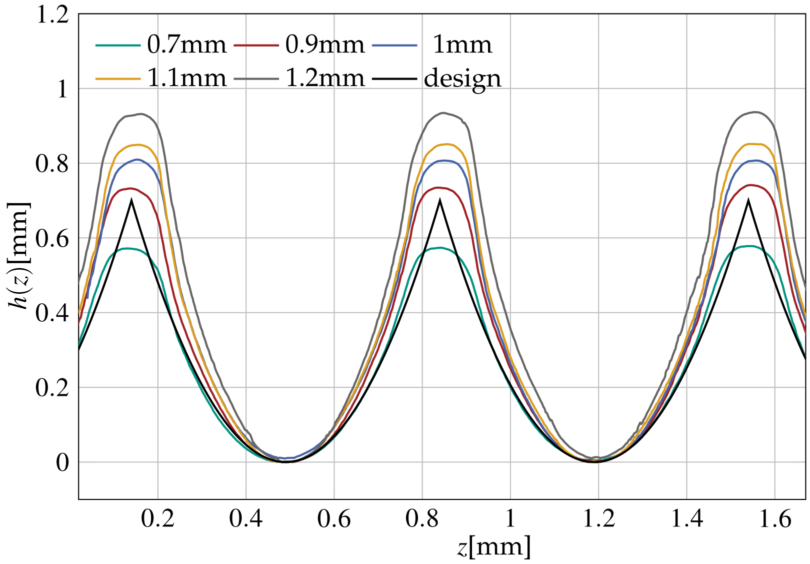

Figure B.5: Resulting height distribution obtained from optical scans for nominal design heights ranging between 0.7 mm and 1.2 mm.

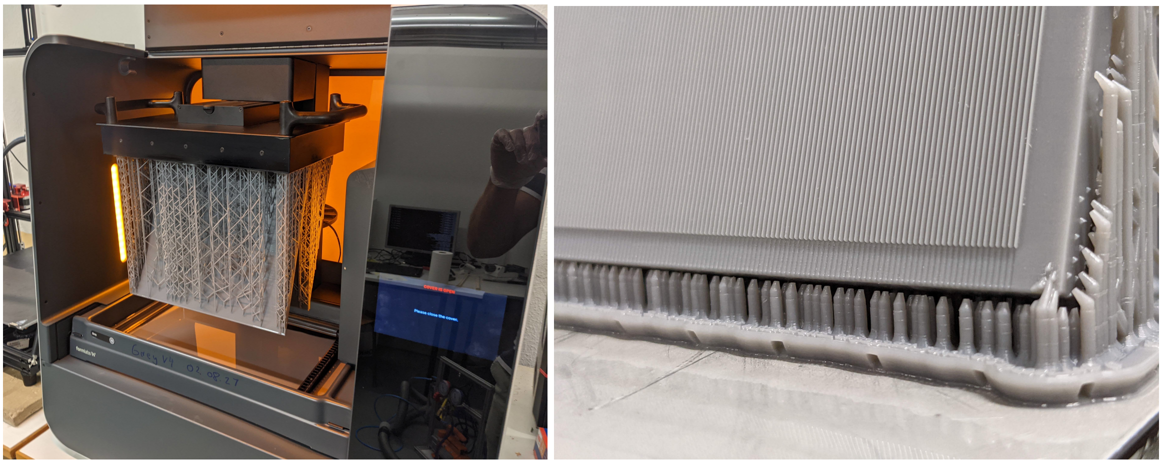

Figure B.6: 3D printed parabolic riblets. (a): completed print of two riblet plates. (b): Detailed view of the 3D printed riblets, including the support structure employed in the printing process.

After cutting the 3D printed riblet plates to the desired streamwise length of 250 mm, the finished riblet plates are glued on a metal carrier plate using epoxy resin. Due to the considerable print time, only a total of eight riblet plates are printed. Thus, 1000 mm of the most downstream wind tunnel section are equipped with riblets. Special attention is given to carefully aligning the individual plates and ensuring evenness in the glueing process. Photographs of the resulting riblet plate built in the test section are shown in figure B.7. The drag-reducing effect of the riblet plates is quantified via measurements of the streamwise pressure gradient in the wind tunnel test section [43].

B.3 Drag-Change Measurements

The obtained skin-friction measurement results are presented in figure B.8 in the form of the relative drag change $\Delta C_f / C_{f0}$. Note that the definition of δ is based upon the parallel protrusion height $h_{\parallel}$ in agreement with the definitions used in chapter 5. δ is 1.4% smaller than $\widetilde{\delta}_{\text{avg}}$, defined as the distance from the average riblet height h_{avg} (see figure B.3) up to the channel centerline. The highest achieved

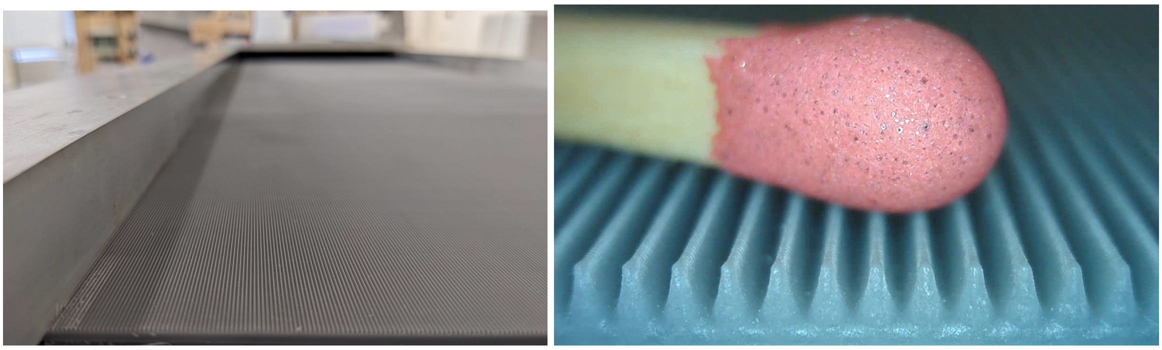

Figure B.7: 3D printed trapezoidal groove riblets. (a): Riblet plates built in the lower wind tunnel wall before sealing the test section with the upper riblet plate. (b): Detailed view of the riblets.

$\Delta C_f/C_{f0}$ is $\approx 5\%$. The pressure-drop-based measurement results agree surprisingly well with the drag-balance measurement of [7], given the rather large tip radius of $r = 40\,\mu\text{m}$ of the 3D printed riblet set. Translating the radius to the tip width t to wavelength ratio t/s utilized by Bechert et al. [7], t/s is six times larger than $t/s = 0.018$ for the respective [7] data set. It is well-known that rib-tip sharpness is crucial for riblet drag reduction [36, 114].

Note that the choice of the half-channel height strongly affects $\Delta C_f/C_{f0}$, as $C_f = \mathcal{O}(\delta^3)$. In chapter 5 it is demonstrated that using $h_{\parallel}$ to define δ leads to good collapse in dimensionless scaling for 2D structures of varying physical size. Thus, the data of Bechert et al. [7] is rescaled to match the protrusion height-based definition of δ.

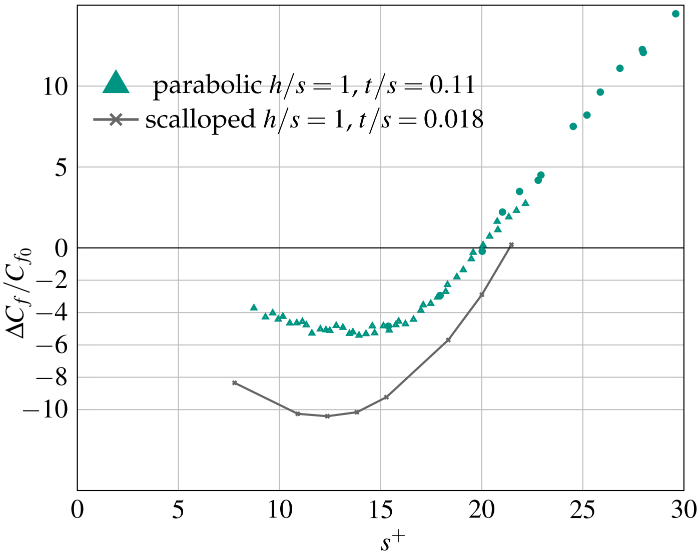

Figure B.8: Relative drag change $\Delta C_f/C_{f0}$ vs. the viscous-scaled riblet spacing s^+. 3D printed parabolic riblet vs experimental data from Bechert et al. [7]. Note that $h_{\parallel}$ based scaling of δ is used and the reference [7] data is rescaled to match this definition.

Albeit difficulties remain in manufacturing and the assembling process, the general suitability of 3D printing as an additional manufacturing technique is demonstrated with the present study. Special attention is needed to ensure evenness and the alignment of the individual 3D-printed plates. Sharp edges cannot be accurately 3D printed and are discretized with a radius of $r = 40\,\mu\text{m}$ limiting the achievable drag reduction in riblet studies. Increasing the wall-normal resolution of the 3D print to $25\,\mu\text{m}$ could help to obtain better print results.

Note that the relatively soft 3D-printed plastic, especially when further weakened by the introduced vacuum channels as shown in figure B.2, can be deformed when mounting the wind tunnel plates into the test section of the wind tunnel. Unfortunately, a slightly uneven channel height across the span of the channel is detected and the overall averaged value is used. Therefore, note that the results shown in figure B.8 demonstrate the general suitability of the 3D printing approach as the expected drag-reducing behaviour can be deduced. However, the presented data might be subject to systematic error sources and do not meet the usually achieved 0.4% uncertainty in $\Delta C_f / C_{f0}$ for the utilized facility [43].

In order to establish the 3D printing approach and ease the involved curing, cutting and alignment of individual plates, the vacuum curing set-up needs further optimization. Ideally, the same vacuum channels can be used during CNC milling, which is not the case in the present study. Currently, the plates were clamped on the sides, which proved to be a delicate task to ensure a tight fit during machining without damaging the sensitive plates. Moreover, establishing a vacuum bagging approach when glueing 3D printed plates onto the carrier metal plate should make the procedure more precise and less error-prone.